UNIVERSITY OF CALIFORNIA
SANTA CRUZ

LUNAR MAGNETISM, SPACE WEATHERING, AND ICY SATELLITE INTERIORS

A dissertation submitted in partial satisfaction
of the requirements for the degree of

DOCTOR OF PHILOSOPHY

in

EARTH SCIENCES
with an emphasis in PLANETARY SCIENCE

by

Douglas Hemingway

September 2015

The Dissertation of Douglas Hemingway
is approved:

_____
Professor Francis Nimmo, chair

_____
Professor Ian Garrick-Bethell

_____
Professor Gary Glatzmaier

_____
Professor Jasper Halekas

_____
Tyrus Miller
Vice Provost and Dean of Graduate Studies

Table of Contents

List of Figures

Abstract

Lunar Magnetism, Space Weathering, and Icy Satellite Interiors

by

Douglas Hemingway

An enduring mystery since Apollo is that, in spite of the Moon's lack of a global magnetic field, the surface is nevertheless dotted with regional magnetic fields strong enough to be detected from orbit. Did the Moon once have an intrinsic global field that magnetized parts of the crust but has since decayed away? This is a question of fundamental importance to understanding the formation and evolution of solid planetary bodies, and yet it remains unanswered due in part to limitations in our knowledge of these crustal magnetic anomalies. Adding to the puzzle, many of these magnetic anomalies are accompanied by enigmatic optical features, known as swirls, which may hold the key to understanding "space weathering"—a process by which airless bodies change color over time due to exposure to solar wind and micrometeoroids. Here we show both that swirl morphology provides information about the structure of the underlying magnetic sources, and that the color of the lunar surface varies systematically with latitude in a way that allows us to distinguish between the effects of solar wind ion and micrometeoroid bombardment, addressing a decades-old problem in remote sensing, and aiding in the interpretation of the spectra of airless bodies throughout the solar system.

The remarkable diversity of the outer solar system's satellites provides important clues about the formation and evolution of the solar system. Many of

the satellites have surprisingly young surfaces, owing in some cases to on-going geologic activity. Moreover, the existence of subsurface oceans within some of the satellites raises the intriguing possibility of extant habitable environments in the outer solar system. Determining the properties of their ice shells and the structures of their deep interiors places fundamental constraints on how the icy satellites formed and evolved, and on what governs their behavior today. Using gravity and topography data from *Cassini*, we develop analytical models showing that Titan's ice shell may be very rigid and therefore unlikely to be geologically active. In contrast, we also model the internal structure of the tiny, but highly geologically active moon Enceladus, and find that a subsurface liquid ocean is likely.

Acknowledgements

The text of this dissertation includes modified reprints of previously published material. Chapter 2 is a slightly modified reprint of *Hemingway and Garrick-Bethell* (2012); the co-author (Garrick-Bethell) supervised the research. Chapter 3 is a slightly modified version of *Hemingway et al.* (2015); the first co-author (Garrick-Bethell) supervised the research; the second co-author (Kreslavsky) supported the research and carried out the determination of phase angles associated with the Clementine mosaics; the text of this paper is used with the permission of all co-authors. Chapter 4 is adapted from *Hemingway et al.* (2013); the first co-author (Nimmo) supervised the research; the second (Zebker) and third (Iess) co-authors, respectively, supplied the topography and gravity models used in the analysis; the text is used with the permission of all co-authors. Chapter 5 describes research I carried out in support of the multi-author publication *Iess et al.* (2014); only my own contributions, under the supervision of Professor Nimmo, are included in this dissertation. Material contributed by other authors of *Iess et al.* (2014) is not included here.

I am extremely grateful for the unhesitating support of my academic advisors, Ian Garrick-Bethell and Francis Nimmo, for their advice and guidance, and for the time they shared so generously with me over the past few years. I

am also grateful to Erik Asphaug, who has always been very supportive and helpful with general advice, especially during my first two years of grad school. For their time and helpful advice, I am also thankful to Gary Glatzmaier and Jasper Halekas, who have kindly served on my reading committee for the last three years. Discussions and technical support from Lon Hood, Bob Lin, and Jasper Halekas were very important during my first major research work, detailed in Chapter 2. The work detailed in Chapter 3 benefitted enormously from numerous discussions with Carle Pieters and Misha Kreslavsky. An informative conversation with Bob Pappalardo helped me first find my way into the field of icy satellites, and ultimately the work described in Chapters 4 and 5. Technical discussions with Howard Zebker, Bill McKinnon and Dave Stevenson were also valuable, and led to some of the ideas discussed in Chapters 4 and 5.

I am grateful to have had an amazing support network of friends and colleagues in the Department of Earth & Planetary Sciences. Of course Jennifer Fish deserves special mention, but really the excellent environment is made by all of the staff, faculty, and grad students, who genuinely take an interest in each other's success. I appreciate everyone's time, and the interest people have taken in my work, especially my lab mates Naor Movshovitz (with whom I have shared countless hours of valuable technical discussion time, both at the white board and at the picnic table), Viranga Perera, Erinna Chen, Tina Dwyer, Delia Santiago, and Carver Thomason. Finally, I am thankful to my family for their support, and especially to Lynne Harden, who has also been a critical sounding board so very often over the past four and a half years.

Chapter 1

Introduction

Gravity and magnetic fields are among the most fundamental and powerful tools for probing the interiors of planetary bodies (*Connerney*, 2007; *Wieczorek*, 2007). An internally generated geomagnetic field is a clear indication of sustained movement of an electrically conducting fluid within the interior. Even if no such field is present, remanent magnetization in crustal rocks can put constraints on the material properties of the crust and may indicate that a geomagnetic field once existed, but has since decayed away, as may be the case for the Moon (*Garrick-Bethell et al.*, 2009). In addition to constraining the properties of the crust and providing clues about the deeper interior, crustal magnetic fields may also affect the evolution of the surface itself by influencing space weathering—the gradual optical evolution of exposed surfaces—through magnetic deflection of solar wind (*Hood and Schubert*, 1980). Gravity is fundamentally about mass distribution and is therefore a crucial tool for interior structure modeling. With a combination of gravity and topography data, we can measure the thickness and elastic properties of a body's lithosphere and place constraints on the deeper interior.

This work divides broadly into two parts. In the first part (Chapters 2 and 3), we use optical and magnetic field data to study "lunar swirls", a class of albedo anomalies associated with strongly magnetized parts of the crust. Swirls offer insights into both the geometry of lunar crustal magnetic sources and the role played by solar wind in space weathering. In the second part (Chapters 4 and 5), we develop analytical models and use them in combination with topography and gravity field data to construct interior structure models for two of Saturn's icy moons, Titan and Enceladus, helping to constrain the likely level of geologic activity on the former and confirming the presence of a subsurface liquid ocean on the latter.

Although the Moon does not possess a global magnetic field today (*Ness et al.*, 1967), parts of its crust are nevertheless magnetized strongly enough to be detected from orbit (*Dyal et al.*, 1970; *Hood et al.*, 2001). The origin of this remanent magnetization is unknown, but it could be the result of crustal rocks having cooled in the presence of a dynamo field that is now extinct (*Garrick-Bethell et al.*, 2009) or transient episodes of intense magnetization associated with basin-forming impact events (*Hood and Artemieva*, 2008; *Mitchell et al.*, 2008). Curiously, many of the crustal magnetic anomalies are co-located with enigmatic collections of morphologically complex bright markings known as "swirls" (*Hood and Schubert*, 1980). The mechanism for the formation of swirls is not known, but their close association with magnetic anomalies suggests that they may be useful for studying the characteristics and origins of lunar crustal magnetism. In Chapter 2, we use Lunar Prospector magnetometer data and Clementine reflectance mosaics to test the hypothesis that swirls are formed where crustal magnetic anomalies, acting as mini magnetospheres, shield portions of the surface from the darkening effects of solar wind ion bombardment,

thereby leaving patches that appear bright compared with their surroundings (*Hood and Schubert*, 1980). We find evidence from two swirls with dissimilar magnetization orientations, Airy and Reiner Gamma, that the bright parts of swirls correspond to dominantly horizontal magnetic fields and that the intra-swirl dark lanes correspond to vertical fields at the surface—just what we would predict if the swirls are in fact formed due to magnetic deflection of solar wind. We further show that source models constrained by the morphology of the swirls produce fields that are consistent with the Lunar Prospector magnetometer observations. We conclude that solar wind deflection is the likely mechanism for the formation of swirls and suggest that swirl morphology provides a previously unrecognized clue to the geometry of the underlying magnetic source bodies (*Hemingway and Garrick-Bethell*, 2012).

Aside from its connection to lunar magnetic anomalies, space weathering is an important phenomenon of its own as it complicates the interpretation of spectroscopic observations of airless bodies everywhere (*Hapke*, 2001). Solar wind and micrometeoroids are thought to be the dominant agents of space weathering, but their relative contributions are not yet well understood. In Chapter 3, building from the findings of *Garrick-Bethell et al.* (2011), we characterize the unique spectral signature of lunar swirls and compare it against the spectra of the lunar surface globally. Using Clementine mosaics, we find a previously unrecognized systematic latitudinal variation in the near-infrared spectral properties of the lunar surface, and show that the characteristics of this latitudinal trend match those observed at swirls. We propose that reduced solar wind flux, which should occur both at swirls and toward higher latitudes, is the common mechanism behind these color variations. This model helps us quantify the distinct effects of solar wind and micrometeoroid weathering and

could aid in interpreting the spectra of airless bodies throughout the solar system (*Hemingway et al.*, 2015).

Beginning with Chapter 4, we turn to the problem of modeling the interior structures of icy satellites, specifically using gravity and topography data from the *Cassini* mission. *Cassini* has made numerous flybys of several of Saturn's moons, most notably, the giant Titan and the small but geologically hyperactive Enceladus—the subjects of Chapters 4 and 5, respectively. A handful of the flybys have been dedicated to determination of the moons' low order gravity fields via radio tracking during close approaches (*Iess et al.*, 2010, 2012, 2014), resulting in good constraints up to spherical harmonic degree 3 in the case of Titan. For Enceladus, only the degree-2 terms and the degree-3 zonal term have been determined. The shape of Enceladus has been determined through compilation of dozens of limb profiles obtained from the Imaging Science Subsystem (*Nimmo et al.*, 2011). This technique has not been applicable to Titan, however, due to the thick and opaque atmosphere. Instead, Titan's topography has been determined by compiling elevation data obtained from *Cassini*'s RADAR system (*Stiles et al.*, 2009; *Zebker et al.*, 2009, 2012). In both of these chapters, we employ an admittance analysis which characterizes the degree to which the topography is compensated, and at what depth, providing an estimate of the thickness of the icy crusts and their elastic properties.

In the case of Titan (Chapter 4), the gravity and topography show a strong and unexpected inverse correlation at spherical harmonic degree 3 (long wavelengths that are not affected by tidal and rotational distortion), suggesting that the high standing topography is associated with negative mass anomalies at depth. We develop analytical models that allow for such a condition, but only if the ice shell is substantially rigid (and therefore unlikely to be geologi-

cally active), if it has been loaded primarily from below, and if the surface has experienced several hundred meters of erosion and deposition, with sediment being redistributed globally (*Hemingway et al.*, 2013).

For Enceladus (Chapter 5), the gravity data are so limited that we are forced to take on the task of analyzing the degree-2 signal, which is complicated by the effects of tidal and rotational distortion. Making the assumption that the compensation mechanism behaves isotropically, we are able to self-consistently separate the degree-2 gravity and topography signals into their hydrostatic (i.e., tidal/rotational) and non-hydrostatic components in a way that allows us to estimate the degree of compensation, the depth at which it occurs, and the moment of inertia. We conclude that Enceladus is substantially differentiated, and that the topography is highly compensated, suggesting that it is supported isostatically, consistent with the presence of a global subsurface liquid layer (*Iess et al.*, 2014).

Three appendices are included at the end of this document, and are as much for my own reference as anything else. In support of Chapters 2, 4, and 5, Appendix A describes the conventions and notation I use when working with spherical harmonics, along with some discussion of the various normalization schemes that are in use. Appendix B details supporting equations for Chapter 2, including conversion from magnetic scalar potential to magnetic flux density and modeling of magnetic fields generated by individual dipoles and linear sources. Finally, in support of Chapters 4 and 5, Appendix C provides a summary of many of the most relevant relations concerning gravitational potential and equilibrium figures arising from tidal and rotational distortion, including some derivations that I find useful to have written out in my own preferred notation.

Chapter 2

Magnetic Field Direction and Lunar Swirl Morphology

This chapter is a modified reprint of Hemingway, D and I. Garrick-Bethell (2012), Magnetic field direction and lunar swirl morphology: Insights from Airy and Reiner Gamma, *J. Geophys. Res. 117*, E10012.

Abstract

Many of the Moon's crustal magnetic anomalies are accompanied by high albedo features known as swirls. A leading hypothesis suggests that swirls are formed where crustal magnetic anomalies, acting as mini magnetospheres, shield portions of the surface from the darkening effects of solar wind ion bombardment, thereby leaving patches that appear bright compared with their surroundings. If this hypothesis is correct, then magnetic field direction should influence swirl morphology. Using Lunar Prospector magnetometer data and Clementine reflectance mosaics, we find evidence that bright regions corre-

spond with dominantly horizontal magnetic fields at Reiner Gamma and that vertical magnetic fields are associated with the intra-swirl dark lane at Airy. We use a genetic search algorithm to model the distributions of magnetic source material at both anomalies and we show that source models constrained by the observed albedo pattern (i.e., strongly horizontal surface fields in bright areas, vertical surface fields in dark lanes) produce fields that are consistent with the Lunar Prospector magnetometer measurements. These findings support the solar wind deflection hypothesis and may help to explain not only the general form of swirls, but also the finer aspects of their morphology. Our source models may also be used to make quantitative predictions of the near surface magnetic field, which must ultimately be tested with very low altitude spacecraft measurements. If our predictions are correct, our models could have implications for the structure of the underlying magnetic material and the nature of the magnetizing field.

2.1 Introduction

2.1.1 Background

Although the Moon does not now possess a global magnetic field (*Ness et al.*, 1967), remanent crustal magnetization has been identified on the surface and several stable regional magnetic fields have been detected from orbit (*Dyal et al.*, 1970; *Coleman et al.*, 1972; *Lin*, 1979; *Lin et al.*, 1998; *Hood et al.*, 2001). Curiously, many, but not all of these crustal magnetic anomalies are accompanied by sinuous patterns of anomalously high surface reflectance known as swirls (*Hood et al.*, 1979; *Hood and Williams*, 1989; *Richmond et al.*, 2005;

Blewett et al., 2011).

Compared with their surroundings, swirls are optically immature, exhibit spectrally distinct space weathering trends (*Garrick-Bethell et al.*, 2011), and are depleted in hydroxyl molecules (*Kramer et al.*, 2011). Swirls appear to overprint local topography, having no detectable topographic or textural expression of their own (*Neish et al.*, 2011). So far not identified anywhere else in the solar system, swirls are unique natural laboratories where space weathering and crustal magnetism intersect. As such, their study could help address important questions in lunar science including the Moon's dynamo history (*Garrick-Bethell et al.*, 2009; *Dwyer et al.*, 2011; *Le Bars et al.*, 2011), the relative influences of solar wind and micrometeoroid bombardment on space weathering (*Hapke*, 2001; *Vernazza et al.*, 2009), and the production and distribution of water over the lunar surface (*Pieters et al.*, 2009; *Kramer et al.*, 2011).

Electrostatic migration of dust has been proposed as a possible mechanism for swirl formation (*Garrick-Bethell et al.*, 2011), as have meteoroid or comet impacts (*Schultz and Srnka*, 1980; *Pinet et al.*, 2000; *Starukhina and Shkuratov*, 2004). Another model suggests that crustal magnetic fields act as mini magnetospheres, deflecting the solar wind and protecting portions of the surface from the optical maturation and darkening effects of proton bombardment (*Hood and Schubert*, 1980; *Hood and Williams*, 1989). This chapter aims to make and test predictions based on this solar wind deflection model for swirl formation.

2.1.2 Predicted Influence of Magnetic Field Direction

The solar wind deflection model suggests that solar wind ions are magnetically deflected due to the Lorentz force. Neglecting the induced electric field, the cross product of particle velocity and magnetic field in the Lorentz Law means the magnetic deflection force is maximized when particle velocity is perpendicular to the magnetic field and zero when it is parallel. Hence, if the high albedo of swirls is the result of inhibited space weathering due to magnetic deflection of solar wind ions, magnetic field direction should influence swirl morphology. While the solar wind incidence angle varies, the ion flux at the surface and thus any darkening effects will be greatest when the ion trajectories are vertical. We therefore predict that portions of the crust that are shielded by dominantly horizontal magnetic fields should receive maximum protection from the solar wind while portions of the crust associated with vertically oriented magnetic fields should experience protection only at high solar wind incidence angles, when darkening effects would be minimal anyway. This suggests that the magnetic fields directly over the bright swirls should be dominantly horizontal and that away from swirls and in the intra-swirl dark lanes, the fields may be either closer to vertical or too weak to offer the surface any protection from solar wind darkening.

Because magnetic field strength decreases rapidly with distance from the source, swirl morphology should depend mainly on the very low altitude structure of the magnetic field. The structure of the field at higher altitudes, where field strength is weaker, has less influence on solar wind deflection. Unfortunately, spacecraft observations are typically limited to higher altitudes and therefore do not directly capture the structure of the near-surface magnetic

field. It is therefore important to understand the way in which the field patterns change with observation altitude, including the role that is played by the direction of magnetization. Figure 2.1 illustrates the magnetic field due to a single dipole that is either vertically oriented (panels a and c) or horizontally oriented (panels b and d). The upper panels (a and b) illustrate magnetic field lines as seen in vertical cross section while the lower panels (c and d) show profiles of the horizontal component of the magnetic field as observed along the dashed lines shown in the upper panels (in both cases, the model dipole is placed at the origin and arbitrarily assigned a magnetic moment of $10^{12}\,\mathrm{Am}^2$). Directly over the vertically oriented dipole, field lines are vertical at any altitude (Figure 2.1a). Peaks in the horizontal field strength appear to either side and are separated by a distance equal to the observation altitude (Figure 2.1c). Directly over the horizontally oriented dipole, field lines are horizontal at any altitude (Figure 2.1b). As the observer moves along an axis parallel to the dipole direction, horizontal field strength decreases, reaching zero (i.e., vertical field lines) at a horizontal distance of $1/\sqrt{2}$ times the observation altitude, before temporarily increasing again slightly (Figure 2.1d). Appendix B gives a quantitative treatment of the way in which magnetic fields vary with position relative to the source.

Our study uses Lunar Prospector magnetometer data collected at altitudes of $\sim 18\,\mathrm{km}$ and higher. While we cannot measure the magnetic field structure below these altitudes, we can distinguish between vertically and horizontally oriented magnetizations (we assume that strong crustal magnetic anomalies are approximately dipolar). This means we can select anomalies exhibiting orientations that allow us to test our predictions. Specifically, we can look for intra-swirl dark lanes at an anomaly with approximately vertical magneti-

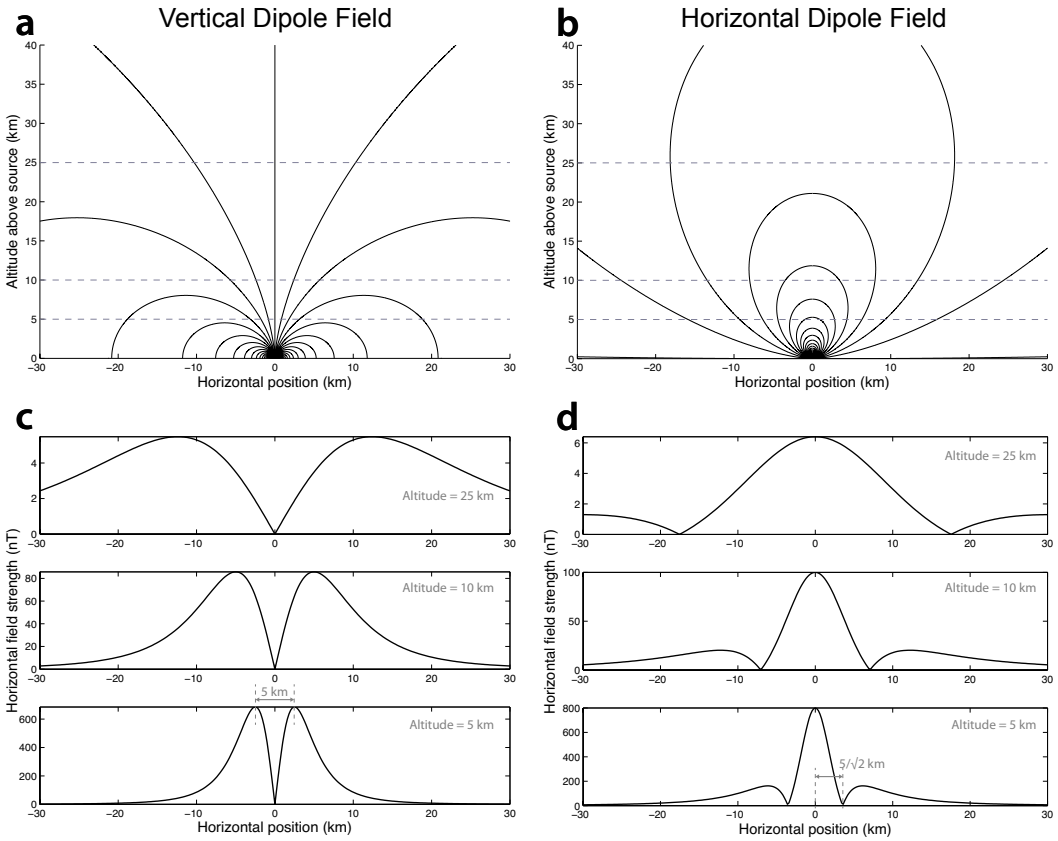

Figure 2.1: Upper panels: magnetic field lines due to a single dipole located at the origin and oriented either vertically (a), or horizontally (b), in the plane of the page; Lower panels: profiles of the horizontal component of the magnetic field shown at the various altitudes represented by dashed lines in the upper panels. In both cases, the dipolar source has a magnetic moment of 10^{12} Am^2.

zation because, in that case, field lines should appear vertical at any altitude over the dark lane (Figure 2.1, panels a and c). Likewise, we can look for a correlation between high albedo and strongly horizontal fields at anomalies with approximately horizontal magnetization because field lines at such anomalies should appear horizontal over the brightest areas regardless of observation altitude (Figure 2.1, panels b and d). We find that the Airy anomaly is similar to the case illustrated in the left panels of Figure 2.1 while the Reiner Gamma anomaly is similar to the case illustrated in the right panels of Figure 2.1.

2.2 Data Processing

2.2.1 Lunar Prospector Magnetometer Data

Our study uses Lunar Prospector 3-axis magnetometer measurements (level 1B data) obtained from NASA's Planetary Data System (ppi.pds.nasa.gov). Two distinct approaches are available for producing maps of crustal magnetic fields from orbital measurements. One involves direct mapping using data selected from a sequence of orbits that cross the region of interest (*Hood et al.*, 1981, 2001), resulting in maps of the field at the spacecraft altitude, while the other involves developing a global spherical harmonic model of the scalar potential field (see Appendix B) and using it to produce maps at arbitrary altitudes (*Purucker and Nicholas*, 2010). The spherical harmonic models are well suited to global mapping and have the advantages of automatically accounting for varying spacecraft altitudes and guaranteeing that the mapped field is a potential field. To date, the best available spherical harmonic models extend to degree 170, corresponding to a horizontal wavelength of ~ 64 km (*Purucker*

and Nicholas, 2010). However, because we are interested in small-scale swirl morphology, we instead employ a direct mapping technique similar to that of *Hood et al.* (2001), allowing us to map features at wavelengths comparable with the spacecraft altitude (as low as ~ 18 km). As discussed by *Hood* (2011), the direct mapping approach is suitable for regional mapping and has several advantages including that it allows us to perform model fitting directly to the minimally processed magnetometer measurements rather than to a derived field model. While we focus here on direct mapping, we did compare our maps against maps we derived from the *Purucker and Nicholas* (2010) model coefficients. We found that in the latter, crustal anomaly fields appear morphologically similar to the same features in our maps, but are typically broader in horizontal extent and exhibit lower field strength.

Each of our maps incorporates data from a sequence of consecutive orbits that cross the anomaly of interest. The polar orbiting spacecraft obtained global coverage twice each lunation, with consecutive orbits spaced ~ 1 degree in longitude (~ 30 km at the equator) and with along-track measurements recorded at 5-second intervals, corresponding to ~ 8 km spacing in latitude. In order to capture the undisturbed signal of the crustal magnetic anomalies, avoiding times when the field is distorted by the impinging solar wind (*Kurata et al.*, 2005; *Purucker*, 2008), we use only those magnetometer measurements collected when the Moon was protected from solar wind while passing through the Earth's magnetotail (excluding times when the field was disturbed by the plasma sheet) or when the Moon was in the solar wind but the spacecraft was in the lunar wake (on the dark side of the Moon and away from the terminator by at least 20°). We examined data from the lowest (< 50 km) altitude phase of the mission, between February and July 1999 (the final six months of the

Lunar Prospector Data for Airy

Day(s) of 1999	Solar wind condition	Minimum solar zenith angle (°)	Mean altitude (km)	Number of Measure-ments	Orbit segments
35,36,37	wind	56	27.5	734	15
49,50	wake	131	18.7	772	15
63,64	wind	29	28.3	759	14
76,77,78	wake	150	18.5	615	12
90,91	tail	9	28.3	610	11
104,105	wake	151	18	678	13
117,118	tail	26	28.3	776	14
131,132	wake	134	34.4	782	14
145,146	wind	52	38.5	838	15
158,159	wake	111	34.3	627	12
172,173	wind	77	38.6	824	15
186,187	wind	88	35.9	660	12
199,200	wind	102	37	785	14
131,132	wake	136	34.4	48	4
91,118	tail	15	28.4	82	7
49,50,77,104	wake	134	18.5	130	12

Table 2.1: Lunar Prospector data used for Airy. The upper part of the table lists the 13 orbit sequences (each consisting of segments of between 11 and 15 consecutive orbits) we examined in a 15° × 15° window centered on the anomaly. The solar wind condition column indicates whether the spacecraft was exposed directly to the solar wind (wind), or protected from it by being either in the lunar wake (wake) or the Earth's magnetotail (tail). The last three rows of the table show the 260 measurements retained after discarding data collected outside of wake and tail times, after combining like-altitude orbit sequences, and after cropping to a 3.25° × 4° study area.

mission). The upper portions of Tables 2.1 and 2.2 list the 13 orbit sequences we examined for each of the Airy and Reiner Gamma anomalies, respectively. In each case, of the 13 orbit sequences we examined, 5 took place in the lunar wake and 2 in the Earth's magnetotail.

We examined orbit segments spanning 15° of latitude approximately centered on each anomaly. Having eliminated measurements taken outside of wake and tail times, we assume that any remaining external fields are steady

Lunar Prospector Data for Reiner Gamma

Day(s) of 1999	Solar wind condition	Minimum solar zenith angle (°)	Mean altitude (km)	Number of Measure-ments	Orbit segments
40,41	wind	51	27.7	820	15
54,55	wake	139	19	769	14
67,68	wind	24	28.5	832	15
81,82	wake	162	18.6	795	15
95,96	wind	3	28.6	834	16
108,109	wake	158	18.3	634	12
122,123	wind	29	28.5	833	15
136,137	wake	135	34.8	703	13
149,150	tail	56	39.3	817	15
163,164	wind + wake	109	34.5	798	15
177,178	wind + tail	82	39.4	842	15
190,191	wind	83	36.3	838	15
204,205	wind	107	37.7	769	14
150	tail	57	39.7	48	4
136,163,164	wake	110	34.3	79	7
54,81,82,109	wake	141	18.3	118	10

Table 2.2: Lunar Prospector data used for Reiner Gamma. The upper part of the table lists the 13 orbit sequences (each consisting of segments of between 12 and 16 consecutive orbits) we examined in a 15° × 15° window centered on the anomaly. The solar wind condition column indicates whether the spacecraft was exposed directly to the solar wind (wind), or protected from it by being either in the lunar wake (wake) or the Earth's magnetotail (tail). The last three rows of the table show the 245 measurements retained after discarding data collected outside of wake and tail times, after combining like-altitude orbit sequences, and after cropping to a 3.25° × 4° study area.

over these 15° of latitude and that fields from isolated crustal sources span no more than a few degrees. After subtracting the mean background field, we assume the remaining fields are due to crustal sources. We then convert the spacecraft position into selenographic spherical coordinates, taking the Lunar Orbiter Laser Altimeter reference radius of 1737.4 km (*Smith et al.*, 2010) as zero altitude, and transform the magnetometer measurements into local east, north, and radial components. We next combine data from consecutive orbits to produce magnetic field maps by fitting regular square meshes to the data using Delaunay triangulation. In order to capture the structure of the signal, the grid cells must be no larger than half the spacecraft altitude, which can be as low as ~ 18 km. We therefore use $0.25^\circ \times 0.25^\circ$ (about 7.6 km $\times$ 7.6 km at the equator) as the grid spacing when fitting to the Lunar Prospector magnetometer (LP MAG) data. This grid resolution is also finer than the spacing between the observations (~ 8 km in latitude, up to ~ 30 km in longitude) meaning that no observed signal variations are lost in the gridding process. Using still finer resolution has no effect on the resulting linearly interpolated surface and is undesired as it increases computation time unnecessarily. Conversely, using a larger (more coarse) grid spacing leads to undesired smoothing in latitude, and as cell size approaches 1°, undesired smoothing occurs in longitude as well. Despite our efforts to remove external fields and avoid times with significant field distortion, portions of some of the orbit sequences still appear to be contaminated by transient signals and are therefore discarded. In order to obtain maps with improved spatial coverage, we combine measurements from different orbit sequences if the observation altitudes are sufficiently similar (differing by less than ~ 1 km). Since the spacecraft altitude varies only slightly (< 1 km) over the scale of our maps (> 120 km), we do not perform

upward or downward continuation of the signal to some fixed altitude. Instead, our maps represent the magnetic field at the slowly varying spacecraft altitude. Finally, we define study areas within the boundaries of the processed data: the Airy study area is illustrated in the left panels of Figure 2.2 while the Reiner Gamma study area is illustrated in the right panels of Figure 2.2. As summarized in the lower portions of Table 2.1 and Table 2.2, this results in Airy study area maps at altitudes of ~ 18 km, ~ 28 km, and ~ 34 km, using a total of 260 LP MAG measurements, and Reiner Gamma study area maps at altitudes of ~ 18 km, ~ 34 km, and ~ 40 km, using a total of 245 LP MAG measurements (only the lowest altitude maps are presented here).

2.2.2 Clementine Reflectance Mosaics

Our study uses Version 2 Clementine 750 nm reflectance mosaics produced by the USGS (United States Geological Survey) map-a-planet service (mapaplanet.org). Compared with the Version 1 (V1) maps, the Version 2 (V2) maps use a newer geodetic control network (*Archinal et al.*, 2006), refining the horizontal registration by as much as 10 km in some locations. We have manually adjusted the V2 reflectance values to match those of the V1 maps, which have been more carefully controlled to represent true reflectance.

2.3 Observations

We focus our discussion here on two specific examples: Airy and Reiner Gamma. The Airy anomaly exhibits a magnetic field resembling the case illustrated in Figure 2.1a while the Reiner Gamma anomaly field resembles the case illustrated in Figure 2.1b. The distinct orientations of these two

anomalies reveal different aspects of the relationship between magnetic field direction and swirl morphology.

2.3.1 Airy

First described by *Blewett et al.* (2007), the Airy swirl is found near Airy crater in the lunar nearside highlands. At the Lunar Prospector spacecraft altitude, the magnetic field lines tend to point inward toward the middle of the anomaly, becoming increasingly vertical and downward pointing at the center (Figure 2.2a), consistent with a source magnetization that is pointed mainly downward. This inferred magnetization direction is based on examination of the vector components and is supported by the models described in section 2.4. Here, contour maps of the total magnetic field strength illustrate only that the albedo anomaly is approximately centered on the magnetic anomaly (Figure 2.2b). However, maps of the horizontal field alone (Figure 2.2c) reveal structure that is more closely related to albedo morphology. For example, the dark lane through the center of the albedo anomaly forms an approximate plane of symmetry in the observed horizontal magnetic field map. Even more striking is the alignment between the dark lane in the center of the anomaly and the line representing zero east-west magnetic field strength (dashed white line in Figure 2.3). The brightest parts of the swirl are organized into two roughly parallel lobes on either side of the dark lane. The center-to-center horizontal distance between the lobes is approximately 8-10 km. Peaks in the horizontal field strength are also organized into two lobes on either side of the dark lane but with a peak-to-peak separation of roughly 30 km (Figure 2.2c). As illustrated in Figure 2.1c, a closer spacing of horizontal field strength peaks

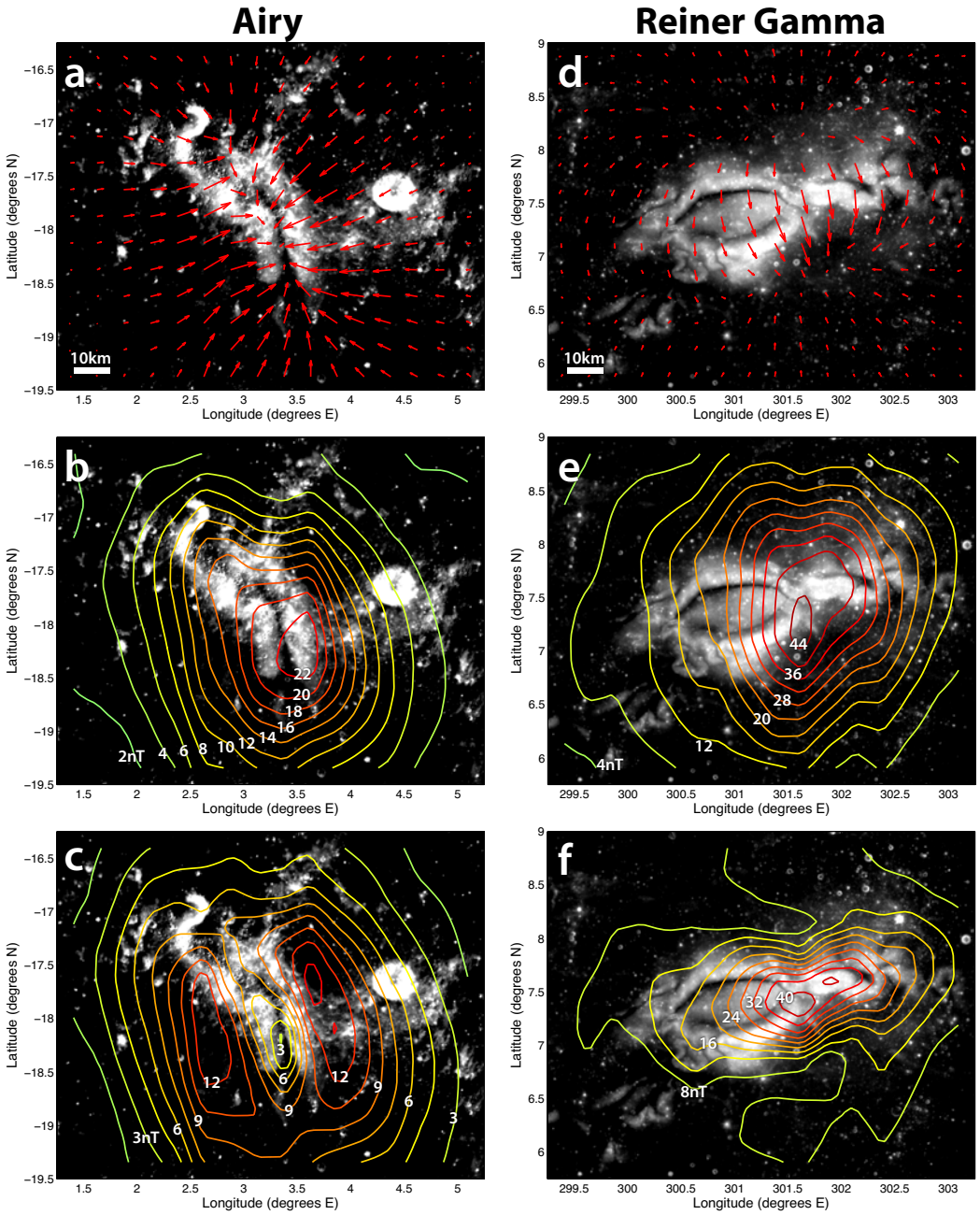

Figure 2.2: Magnetic field maps derived from Lunar Prospector magnetometer data over Clementine 750 nm reflectance maps at the Airy (left panels) and Reiner Gamma (right panels) anomalies. Panels (a) and (d) show the direction of field lines at the spacecraft altitude ($\sim$ 18 km in both cases), with arrow lengths showing relative horizontal field strength. Panels (b) and (e) show contours of the total magnetic field strength and panels (c) and (f) show contours of the horizontal component alone. The Airy maps shown here are derived from LP MAG data collected on days 49-50, 77, and 104 of 1999 while the Reiner Gamma maps are derived from data collected on days 54, 81-82, and 109 of 1999.

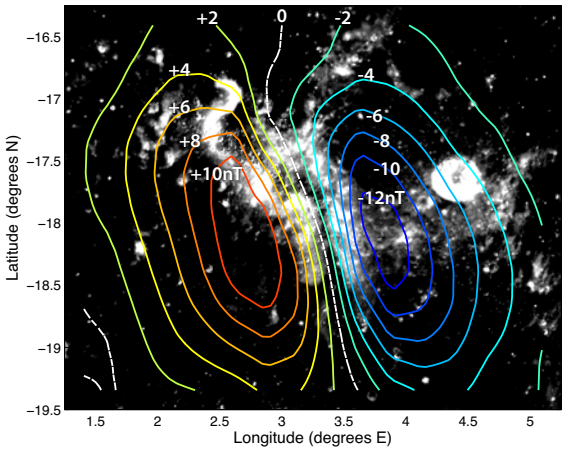

Figure 2.3: East-west component of magnetic field as measured by Lunar Prospector over Clementine 750 nm reflectance at Airy. Contour line colors and labels indicate magnitude of eastward field strength, with warm colors indicating east-pointing fields and cool colors indicating west-pointing fields. The dashed white line indicates zero field strength in the east-west direction. The map is derived from LP MAG data collected on days 49-50, 77, and 104 of 1999.

is expected at lower altitudes, potentially allowing for better alignment with the swirl's bright lobes.

2.3.2 Reiner Gamma

Reiner Gamma, the type example for lunar swirls, is found in Oceanus Procellarum near the western limb of the lunar nearside. At the Lunar Prospector spacecraft altitude, the magnetic field lines are south pointing (Figure 2.2d), consistent with a source magnetization that is mainly horizontal and north pointing. This inferred magnetization direction is based on examination of the vector components, is supported by the models described in section 2.4, and is in agreement with *Kurata et al.* (2005). Contour maps of total magnetic field strength, seen here (Figure 2.2e) and elsewhere (e.g. *Hood et al.* (2001)), illustrate only that the albedo anomaly is approximately co-located with the magnetic anomaly; there is no clear relationship between total field strength

and the morphology of the albedo anomaly. However, contour maps of the horizontal component alone (Figure 2.2f) show that regions of high horizontal field strength correspond well with the bright swirl. Based on SELENE magnetometer data, *Shibuya et al.* (2010) have reported similar findings for Reiner Gamma and other anomalies. Patches of high albedo tend not to occur where fields are weak, or where fields are strong but lack a large horizontal component. This observation is consistent with the hypothesis that darkening due to solar wind ion bombardment will be minimized where magnetic fields are strongly horizontal.

We tested the degree to which magnetic field direction is related to reflectance by measuring the correlation between reflectance and the angle the field makes with the vertical. Figure 2.4 plots reflectance versus magnetic field direction using data points gathered from all six retained sets of LP MAG measurements. Since the field strength varies with altitude, values were normalized to the maximum total field strength for each map before being combined into the set of 245 data points used to generate the scatter plot. Figure 2.5 illustrates the locations of the data points and corresponding reflectance values used to make the scatter plot. The reflectance map in Figure 2.5 has been smoothed by a $0.25^\circ \times 0.25^\circ$ window moving average filter in order to reduce its effective resolution to be comparable to the LP MAG data resolution. This removes the high frequency component of the albedo signal that could not possibly be captured in the lower frequency magnetic field data. The data points in Figure 2.4 are color-coded according to normalized total field strength. Cool colors represent weak fields and warm colors represent strong fields. A blue regression line is fit to the weakest third of the data points and illustrates that, as expected for weak fields, reflectance values are low regardless of magnetic

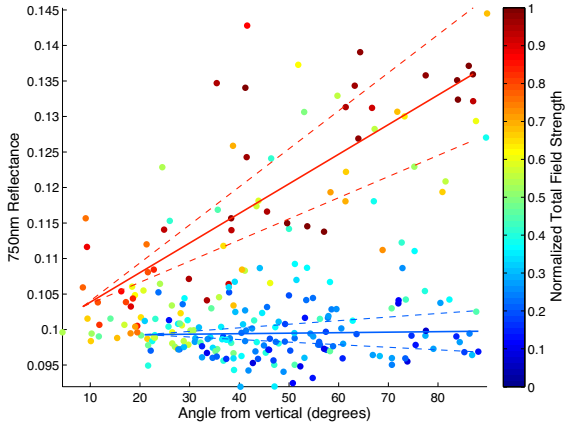

Figure 2.4: Correlation between magnetic field direction and reflectance at Reiner Gamma. 'Angle from vertical' is 90° where field lines are horizontal. Data points are color-coded by total field strength with cool colors representing weak fields and warm colors representing strong fields. Blue and red regression lines are fit to the weakest and strongest thirds of the data points, respectively, demonstrating that magnetic field direction becomes increasingly important with increasing field strength.

field direction. A red regression line is fit to the strongest third of the data points and illustrates that, for stronger fields, reflectance values are low where field lines are vertical and high where field lines are horizontal. Dashed lines are used to show 95% confidence intervals on the estimated slopes, indicating that the observed differences in slope are statistically significant. These trends are precisely what we would expect if the albedo anomalies owe their brightness to magnetic deflection of solar wind.

2.3.3 Discussion

The examples of Airy and Reiner Gamma illustrate distinct aspects of the solar wind deflection phenomenon: the Airy case shows that dark lanes may be associated with vertical magnetic fields (Figures 2.2a–c and Figure 2.3), while the Reiner Gamma example demonstrates that bright areas may be associated with strongly horizontal fields (Figures 2.2d–f and Figure 2.4). In

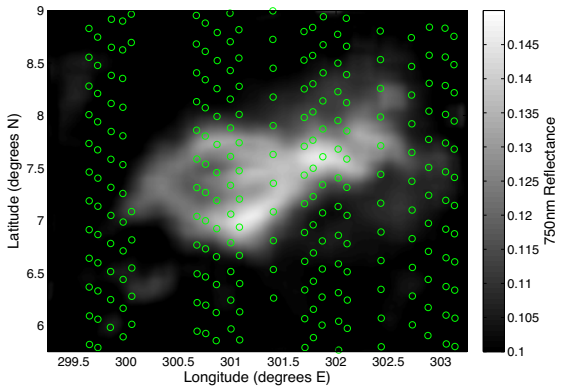

Figure 2.5: Locations of the 245 LP MAG data points (green circles) used to generate Figure 2.4. Background is a Clementine 750 nm reflectance mosaic with resolution reduced to be comparable with the LP MAG data resolution.

principle, however, both of these effects should be present at both locations. That is, we should expect to see alignment between the bright lobes of Airy and peaks in horizontal magnetic field strength and we should expect to see vertical field lines over the dark lanes of Reiner Gamma. But as discussed in section 2.1.2, we expect the near-surface field patterns to dominate solar wind deflection and we do not yet have observations at sufficiently low altitudes to map the near-surface field directly. However, we can use source models to determine whether the near surface field pattern we predict (horizontal over bright areas and vertical over dark lanes) is consistent with the observational constraints we do have.

2.4 Source Modeling

Using a combination of techniques, including a genetic search algorithm, we developed subsurface magnetization source models to gain insight into the possible distribution of source material at the Airy and Reiner Gamma anomalies. We use these models to support our interpretation of the observations discussed

above and to allow us to further test the plausibility of our hypothesis—that areas of high albedo should coincide with dominantly horizontal near-surface magnetic fields.

2.4.1 Lunar Prospector Data Fitting

As a first step, we use the Lunar Prospector magnetometer (LP MAG) measurements to determine the most probable characteristics of the magnetic source (the approximate distribution of magnetic material as well as the magnetic moment magnitude and orientation). The results are spatially coarse as the data are insensitive to variations on scales smaller than the observation altitudes. The results are also inherently non-unique as trades can be made between depth and magnetic moment magnitude, for example. Previous studies have modeled the source of the central part of the Reiner Gamma anomaly as a single dipole (*Kurata et al.*, 2005) or as a grid of dipoles (*Nicholas et al.*, 2007) using inversion techniques (*Von Frese et al.*, 1981; *Purucker et al.*, 1996; *Dyment and Arkani-Hamed*, 1998; *Parker*, 2003) to obtain models that best fit the LP MAG data in a least-squares sense. Here, we employ an alternative approach involving iterative forward modeling to identify the characteristics of the best-fitting solutions. Our approach demonstrates that a range of different solutions can deliver similarly good results. Throughout our modeling, we make the simplifying assumption that the source material is coherently magnetized in a single direction; much larger remanent magnetizations would be required to produce the observed fields if the source materials were not unidirectionally magnetized, and the inferred values are already large (as discussed in section 2.5.1).

2.4.1.1 Airy Single Dipole Model

We begin with a single dipole model to find the magnetic moment direction that best fits, in a least squares sense, the 260 LP MAG measurements of the Airy study area. We define the 'effective error' at each data point as the maximum of the three vector component residuals. The least squares solution thus minimizes residuals in all three vector components simultaneously. We vary the burial depth from 0 to 20 km in 1-km increments and the magnetic moment magnitude from 0 to 8×10^{12} Am^2 in increments of 5×10^{11} Am^2. We vary the inclination (angle positive downward from the horizontal) from -90° to +90° and the declination (angle positive clockwise from north) through 360°, each with 1° resolution. We find the measurements are well accommodated by a dipole buried between 10 and 20 km below the surface, with magnetic moment magnitude between 4×10^{12} Am^2 and 7×10^{12} Am^2, inclination between 79° and 81° and declination between -14° and +29° (i.e., pointed steeply downward and slightly to the north). Since this method delivers equally good solutions over a wide range of depths and magnetic moment magnitudes, we do not attempt to constrain depth and magnitude at this stage. In any case, because we are assuming a single dipole, the model fit overestimates the true source depth.

2.4.1.2 Reiner Gamma Single Dipole Model

For Reiner Gamma, we again begin with a single dipole oriented so that it best fits, in a least squares sense, the 245 LP MAG measurements at the Reiner Gamma study area. Using the 'effective' error metric described for the Airy model above, we search for the least squares best fit by varying the burial depth from 0 to 20 km in 1-km increments, the magnetic moment magnitude

from 0 to 2×10^{13} Am^2 in increments of 10^{12} Am^2, the inclination from -90° to +90° and the declination through 360°, with 1° resolution for both inclination and declination. We find that the measurements are well accommodated by a dipole that is buried between 8 and 15 km below the surface with magnetic moment between 9×10^{12} Am^2 and 16×10^{12} Am^2, inclination between -6° and +5° and declination between -18° and -3° (i.e., lying approximately in the plane of the lunar surface and pointing slightly west of north). For comparison, *Kurata et al.* (2005) modeled this part of the anomaly as a single dipole buried 11.1 km below the surface with magnetic moment 11.3×10^{12} Am^2, inclination +1.3° and declination -11°. Once again, depth and magnitude are not well constrained by the data and are overestimated by this single dipole model.

2.4.1.3 Genetic Search Algorithm

Next, for each of the two anomalies, we expand the parameter space by replacing the single dipole with a grid of dipoles, separated by 0.25° in both latitude and longitude (a distance comparable with half the minimum spacecraft altitude), resulting in a total of 208 dipoles. We allow each of the 208 dipoles' magnitudes to vary independently. We allow the burial depth of the grid to vary as a whole but burial depth does not vary between dipoles and we do not allow the dipoles to be above the lunar surface. Likewise, we allow the magnetization direction to vary as a whole but direction does not vary between dipoles. This opens a parameter space that is too large to explore completely, even with coarse resolution. Instead, we employ a heuristic search technique known as a "genetic algorithm" that iteratively adjusts each of the 211 independent parameters (208 independent dipole moment magnitudes plus depth of the grid, inclination and declination), gradually progressing toward

improving least-squares solutions.

Genetic algorithms have a diverse range of applications (*Holland*, 1992; *Goldberg*, 1989) including large-scale optimization problems such as ours: to find a source model (defined by 211 parameters) that produces minimal error between predicted and observed magnetic fields. Genetic algorithms employ concepts borrowed from gene-centered biological evolution (*Dawkins*, 1976) in order to iteratively (i.e., over many generations) progress towards solutions with increasing degrees of 'fitness'. In our case, this 'fitness' is a measure of how well the magnetic field produced by the source model matches the Lunar Prospector magnetometer (LP MAG) observations.

Our algorithm begins by generating a population of individual source models with randomly distributed characteristics. The characteristics of each individual source model are defined by its 'genes', with each individual having all 211 distinct genes (208 dipole moment magnitudes plus depth of the grid, inclination and declination). At each iteration, or generation, the individual members of the population are evaluated according to how well they predict the magnetic field at each of the LP MAG observation points. We compute the error between the prediction and the observation using the 'effective error' metric described above (maximum of the three vector component residuals). We then rank the individuals from lowest to highest sum of squared effective errors. The individuals with the lowest errors are then selected as the 'parents' of the next generation. The next iteration begins by generating a new population to replace the previous generation. Each individual in the new generation is formed by setting each of its 211 genes equal to the corresponding gene from one of its parents in a process known as crossover (analogous to chromosomal crossover). For example, an individual's gene for inclination

will match the inclination gene of one of its parents (chosen at random from among the parents). Because only the best-performing individuals contribute their genes to the next generation, individuals of each new generation tend to inherit the best characteristics of the previous generation. We then apply random mutations (i.e., randomly adjust several isolated genes). This step ensures variation in the population and allows for the possibility of introducing advantageous genes not possessed by the parents. Finally, members of the new generation are evaluated and their best performers are selected as the parents of the next generation. With each generation, genes that result in large model errors tend to be discarded while genes that result in smaller model errors tend to be retained. Inheritance and selection lead the gene pool to be increasingly rich in genes that form good source models while crossover and mutations ensure variation, allowing for innovations that can lead offspring to outperform their parents. The result is that the population progresses gradually towards optimality in terms of minimum model error.

While this explanation captures the essence of the algorithm, our implementation includes additional details such as gene mutation rate (the probability that any given gene will mutate) and how "random" mutations are distributed (i.e., it is not useful to have sudden changes in burial depth on the order of 1000 km, for example, so mutations must be limited to reasonable adjustments according to some distribution). We experimented with various population sizes and numbers of parents selected at each generation (there must be at least two parents but more than two is also allowed). For computational efficiency, a small population size is preferred. The algorithm was found to operate effectively with a population of just 10 individuals in which the top-performing 3 contribute their genes to the next generation. We allow

mutations to occur with a probability of 0.1 and when they do occur, the gene is adjusted from its current value according to a normal distribution with some pre-defined standard deviation (which depends on whether the gene has units of kilometers, degrees or Am^2). We also apply smaller mutations with a higher probability in order to ensure a measurable degree of variation in the population. The initial population is generated based on a seed model; each individual in the initial population is formed by applying normally distributed adjustments to each of the genes in the seed model. While the choice of seed model and parameter settings influences the efficiency of the algorithm (i.e., how quickly it reaches a good solution), the end results tend to be very similar across a wide range of parameters and initial conditions. The algorithm was allowed to iterate through 600 generations (Figure 2.6). Based on the trends in error evolution (Figure 2.7), we would not expect additional iterations to yield substantial improvements.

2.4.1.4 Airy Dipole Grid Model

For the Airy dipole grid model, we initiate the genetic search algorithm with a downward pointing magnetization in accord with the best fitting single dipole (80° inclination, 8° declination) and an arbitrary burial depth of 10 km. Again, the genetic search algorithm attempts to find a solution that minimizes the sum of squares over the 'effective' error at each of the 260 LP MAG data points. The dipoles in the final model grid have inclination 79°, declination 20° and a total magnetic moment of $4.7 \times 10^{12}\,Am^2$ distributed as shown in Figure 2.8. The final grid has a burial depth of ~ 650 meters, but again, depth is not well constrained by the LP MAG data as it can be traded against magnetic moment magnitude and the lateral extent of the source; an equally good

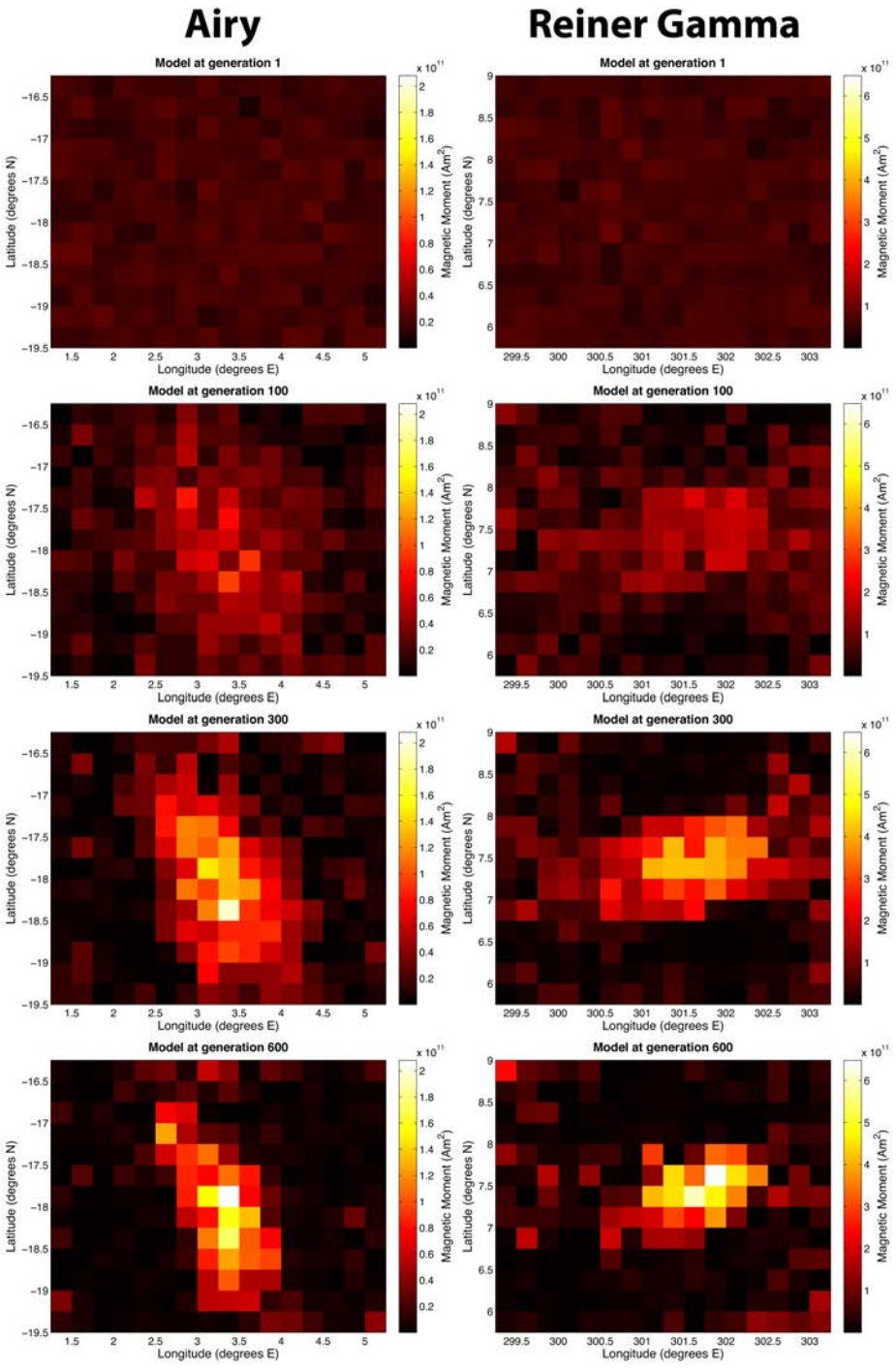

Figure 2.6: Snapshots at generations 1, 100, 300, and 600 during the evolution of the dipole grid source models for Airy (left panels) and Reiner Gamma (right panels). Each panel shows the distribution of magnetic moments from the best-performing model of the specified generation.

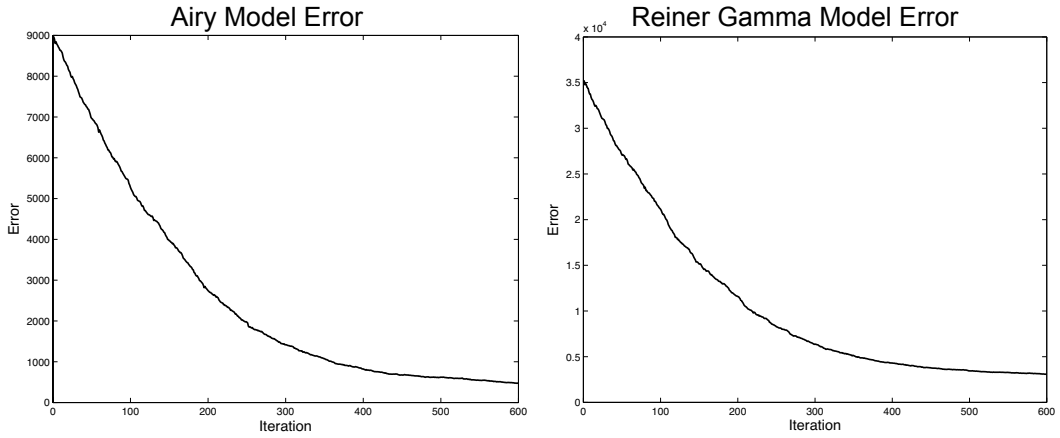

Figure 2.7: Evolution of dipole grid source model error over 600 generations for Airy (left panel) and Reiner Gamma (right panel). The error shown is the sum of squared 'effective' errors (as described in section 2.4.1.1) over all LP MAG data points for the best-performing model in each generation.

fit could be obtained with a source that is deeper, stronger and more horizontally concentrated. Although the model is spatially coarse, the distribution of magnetic moments appears to be consistent with a source structure that is centered on the anomaly and elongated in a north-south direction. Figure 2.9 shows that the resulting model field compares very well with the observed field. The magnetization direction is close to that of the hypothetical field illustrated in Figure 2.1a, indicating that the intra-swirl dark lane may well coincide with vertical field lines at the surface.

2.4.1.5 Reiner Gamma Dipole Grid Model

As with the Airy model, we replace the single dipole model with a grid of 208 dipoles and use the genetic algorithm to find a solution that best fits the 245 LP MAG data points. The final model dipole grid is magnetized with inclination +4° and declination -12° at a depth of 1.6 km (but again, depth is not well constrained by the LP MAG data), and has total magnetic moment

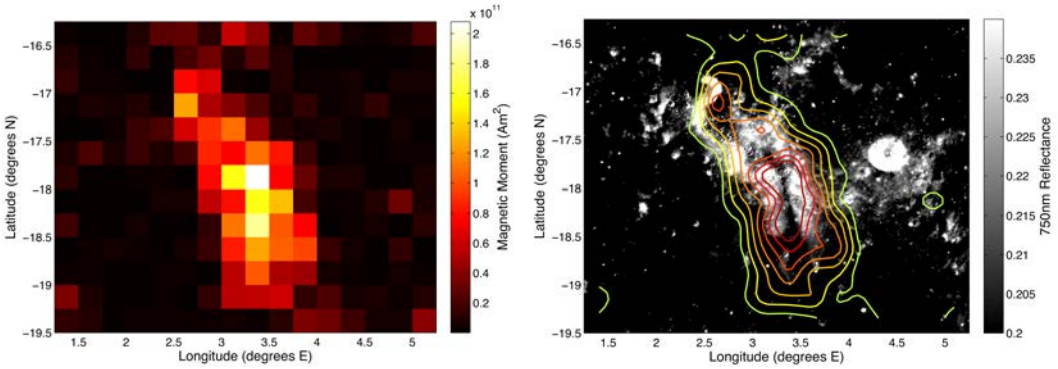

Figure 2.8: The Airy source model obtained via the genetic search algorithm described in section 2.4.1.3. In the left panel, each square represents a single dipole covering $0.25^\circ \times 0.25^\circ$ (roughly $5.5 \times 10^7\,\mathrm{m}^2$) with the color indicating each dipole's total magnetic moment (typical values in the center are $\sim 1.25 \times 10^{11}\,\mathrm{Am}^2$ per dipole). The right panel shows the same information as contours over Clementine albedo, suggesting approximate agreement between the source structure's longitudinal axis and that of the swirl's dark lane.

$\sim 1.4 \times 10^{13}\,\mathrm{Am}^2$ distributed as shown in Figure 2.10. The source model is spatially coarse but is consistent with a source structure that is elongated in the east-west direction and is most intense in the brightest part of the albedo anomaly. Figure 2.11 shows that the resulting model field compares well with the observed field. For comparison, *Nicholas et al.* (2007) modeled the Reiner Gamma source as a grid of dipoles separated by 0.1° and placed at the surface, coincident with the albedo anomaly. Those authors assumed a northward magnetization and solved for the magnitude and sign at each of the dipoles, obtaining the distribution of magnetization illustrated in Figure 2.12. In spite of the very different methods employed, the two results resemble one another, predicting strong magnetization in the brightest parts of the anomaly.

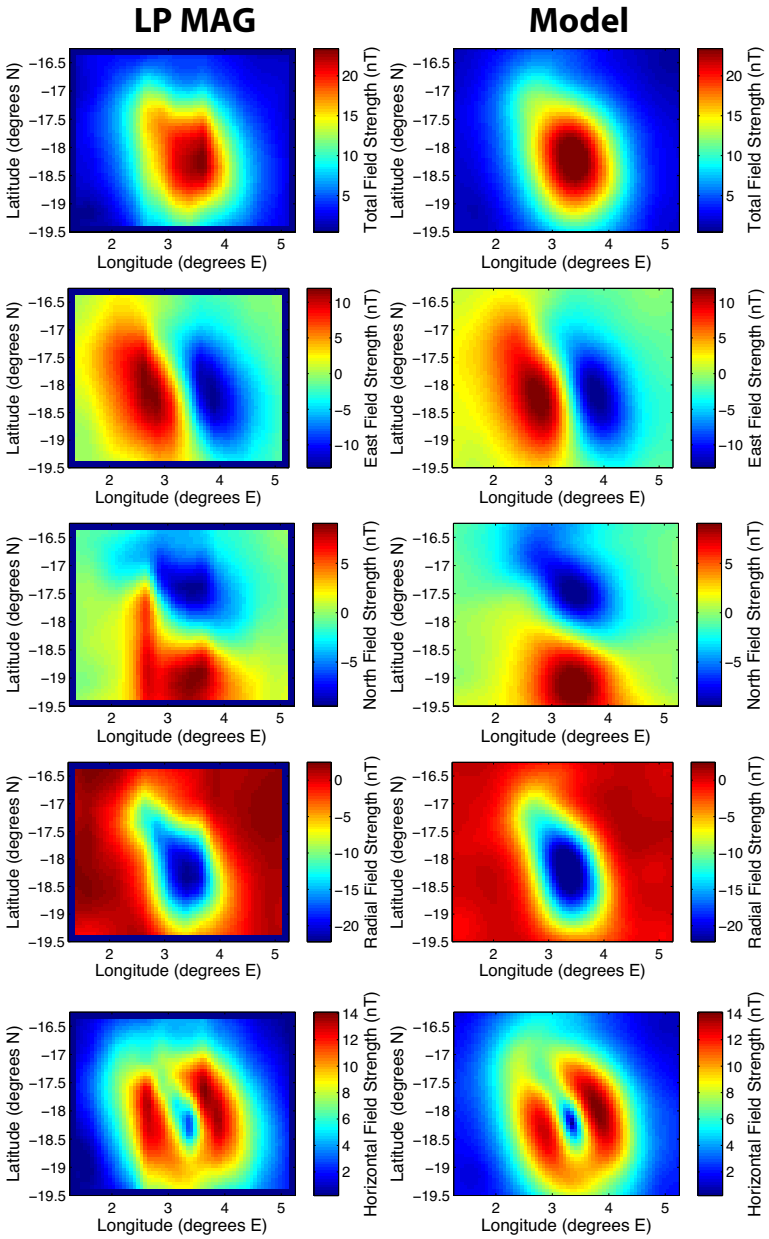

Figure 2.9: Comparison of the observed field at $\sim$ 18 km over Airy (left panels; derived from LP MAG data collected on days 49-50, 77, and 104 of 1999) and the model field (right panels; obtained by fitting a grid of dipoles to the LP MAG data using the genetic search algorithm).

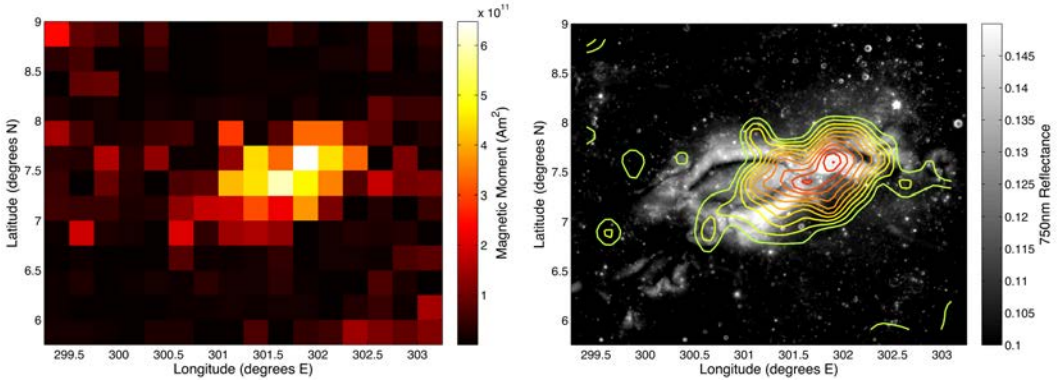

Figure 2.10: The Reiner Gamma source model obtained via the genetic search algorithm described in section 2.4.1.3. In the left panel, each square represents a single dipole covering $0.25^\circ \times 0.25^\circ$ (roughly $5.7 \times 10^7\,\mathrm{m}^2$) with the color indicating each dipole's total magnetic moment (typical values in the center are $\sim 3.4 \times 10^{11}\,\mathrm{Am}^2$ per dipole). The right panel shows the same information as contours over Clementine albedo.

2.4.2 Albedo Pattern Matching

The results of the genetic search algorithm suggest that the distribution of the underlying source material coincides roughly with the shape of the albedo anomaly: a north-south distribution for Airy and an east-west distribution for Reiner Gamma. Here, we refine our source models by applying the constraint that the near-surface field be structured according to our hypothesis: strongly horizontal over the brightest parts of swirls and vertical in the intra-swirl dark lanes. This allows for greatly improved spatial resolution since Clementine reflectance mosaics are available at 256 pixels/degree whereas LP MAG data are limited to $\sim 1-4$ pixels/degree. If our hypothesis is correct, source models constrained by the albedo pattern should produce fields that are consistent with the LP MAG observations made at higher altitudes. Below, we show that even simple source models are sufficient to accomplish this, suggesting that our models are highly plausible.

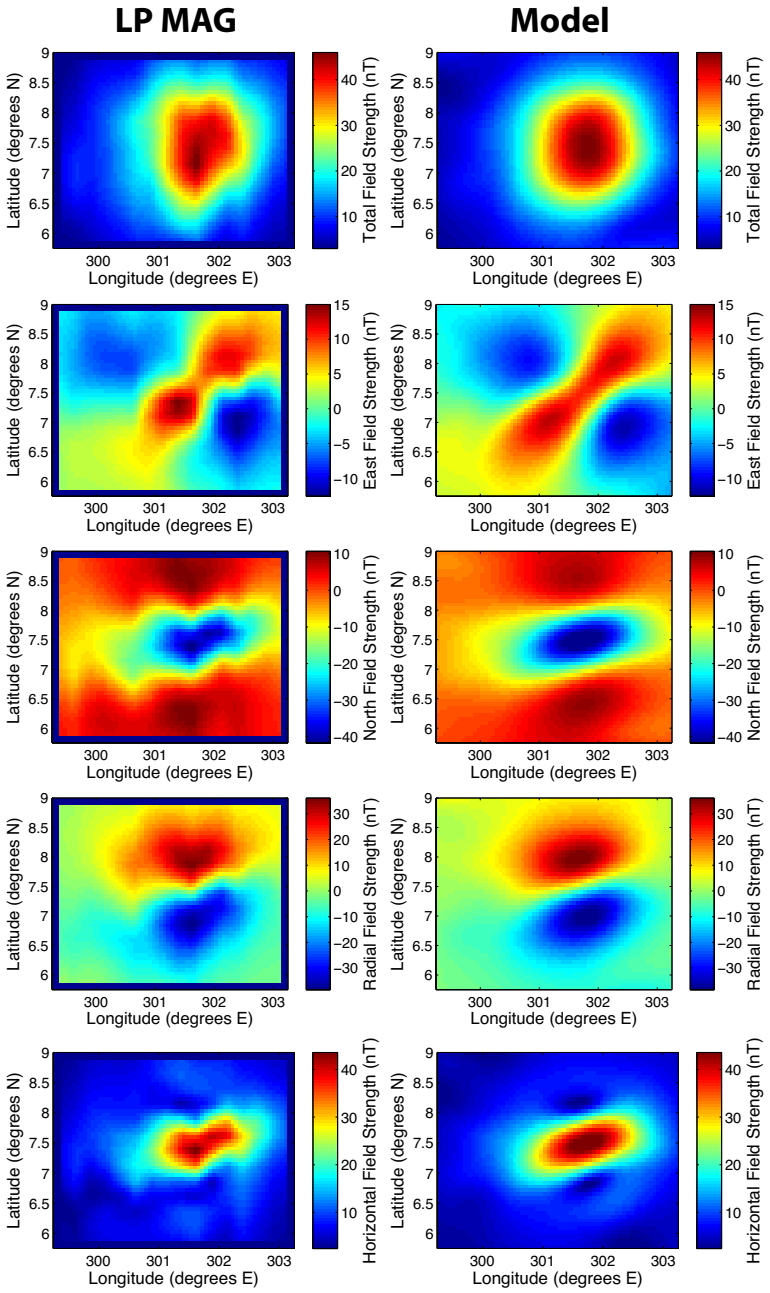

Figure 2.11: Comparison of the observed field at ~ 18 km over Reiner Gamma (left panels; derived from LP MAG data collected on days 54, 81-82, and 109 of 1999) and the model field (right panels; obtained by fitting a grid of dipoles to the LP MAG data using the genetic search algorithm).

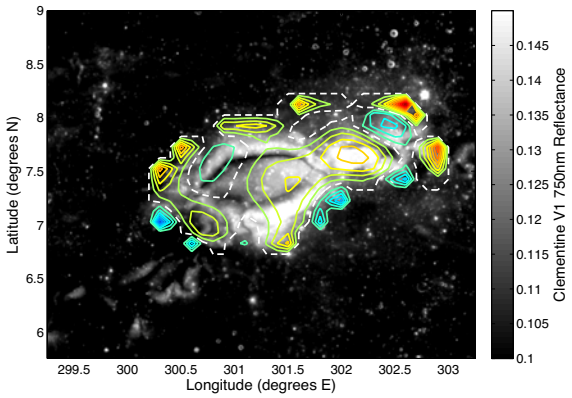

Figure 2.12: Distribution of source magnetization at Reiner Gamma as estimated by *Nicholas et al.* (2007) assuming the source layer is 40 km thick. The contour interval is 0.1 A/m with warm colors positive, cool colors negative and the dashed white contour representing zero magnetization. The contours are superimposed over Clementine V1 750 nm reflectance. Note: our study instead uses Clementine V2 mosaics, which differ in horizontal registration by ~ 7 km in the vicinity of Reiner Gamma.

2.4.2.1 Airy Model

Given the downward-pointing magnetization at Airy (section 2.4.1.4) and the associated field pattern (Figure 2.1c), the morphology of the Airy swirl suggests a roughly linear source structure following the dark lane. In order to be consistent with our hypothesis, the vertically magnetized source material cannot substantially underlie the bright lobes since this would mean vertical field lines in bright areas. We therefore replace the grid of dipoles described in section 2.4.1.4 with an array of 32 dipoles arranged as a two-segmented linear feature following the dark lane (Figure 2.13, left panel). In cross-section, the field pattern from such a line source resembles the pattern from a single dipole (illustrated in panels a and c of Figure 2.1). However, for a linear source, the peaks in the horizontal field profile are shifted outward slightly such that the peak-to-peak separation is $2/\sqrt{3}$ times the altitude above the source rather than being equal to the altitude above the source (details are given in Ap-

pendix B). If we assume the two bright lobes at Airy (separated by $\sim 9\,\mathrm{km}$) are aligned with peaks in the surface horizontal magnetic field profile, then the depth of this line source must be $\sim 7.8\,\mathrm{km}$. Because we assume an infinitely narrow source, this represents the maximum possible source depth consistent with the hypothesis that the bright lobes align with peaks in the horizontal magnetic field profile. The LP MAG data are too spatially coarse to constrain the distribution of magnetic moments within the source structure so we assign equal strength to each of the 32 dipoles in the array. With the depth fixed and the dipole moment magnitudes set to be equal, the parameter space is reduced to three dimensions (total magnitude, inclination, and declination), allowing for a complete search (varying magnitude in increments of $10^{11}\,\mathrm{Am}^2$ and inclination and declination in 1° increments) to find the solution that best fits, in a least squares sense, the LP MAG data. The resulting best-fit solution has the dipoles pointed steeply downward (inclination 75°, declination -20°) with total magnetic moment $3.8 \times 10^{12}\,\mathrm{Am}^2$ (Table 2.3). This source model produces a magnetic field pattern at the surface that mimics the morphology of the albedo anomaly, with the field being strongly horizontal in high albedo areas and vertical in the intra-swirl dark lane (Figure 2.13). Remarkably, this same simple source model produces a field pattern at the spacecraft altitude that substantially resembles the LP MAG observations (Figure 2.14).

2.4.2.2 Reiner Gamma Model

The Airy model (2.4.2.1) suggests that the dark lane is aligned with a cusp between two peaks in the horizontal magnetic field profile. Based on the Airy example, we may view the two dark lanes at Reiner Gamma as suggestive of cusps in the near-surface horizontal magnetic field profile (see *Harnett and*

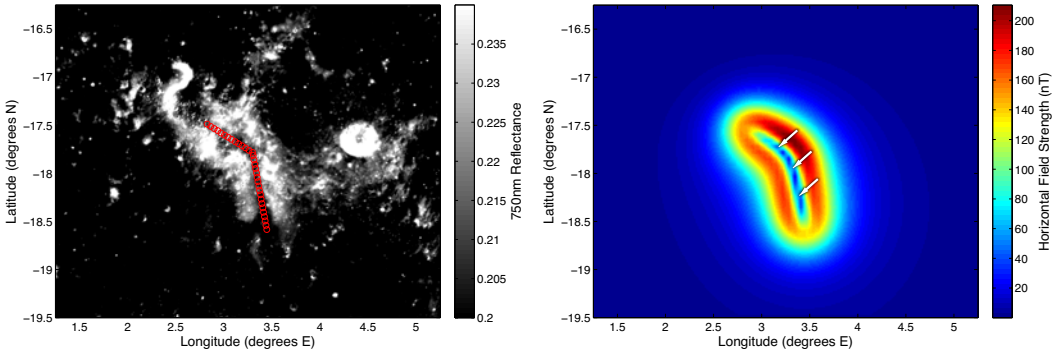

Figure 2.13: Left panel: Airy study area showing Clementine albedo map with red circles indicating the locations of the source model's 32 dipoles; Right panel: resulting horizontal magnetic field strength predicted at the surface. White arrows indicate where field lines become vertical in the intra-swirl dark lane. Figure 2.14 compares the model field predicted at the spacecraft altitude with the LP MAG observations.

Albedo Pattern-Based Model for Airy

Latitude (°N)	**Longitude** (°E)	**Latitude** (°N)	**Longitude** (°E)
-17.489	2.826	-17.906	3.322
-17.512	2.862	-17.951	3.330
-17.534	2.899	-17.996	3.338
-17.557	2.935	-18.041	3.347
-17.579	2.972	-18.087	3.355
-17.602	3.008	-18.132	3.363
-17.624	3.044	-18.177	3.372
-17.647	3.081	-18.223	3.380
-17.669	3.117	-18.268	3.389
-17.692	3.153	-18.313	3.397
-17.714	3.190	-18.359	3.405
-17.737	3.226	-18.404	3.414
-17.759	3.263	-18.449	3.422
-17.782	3.299	-18.494	3.430
-17.815	3.305	-18.540	3.439
-17.860	3.313	-18.585	3.447

Table 2.3: Final dipole array model for Airy as described in section 2.4.2.1 (Figure 2.13). The model consists of 32 dipoles at the indicated latitudes and longitudes, all buried 7.8 km below the surface. The total magnetic moment is 3.8×10^{12} Am^2. All dipoles in the array have inclination 75°, measured positive downward from the horizontal and declination -20°, measured positive clockwise from north.

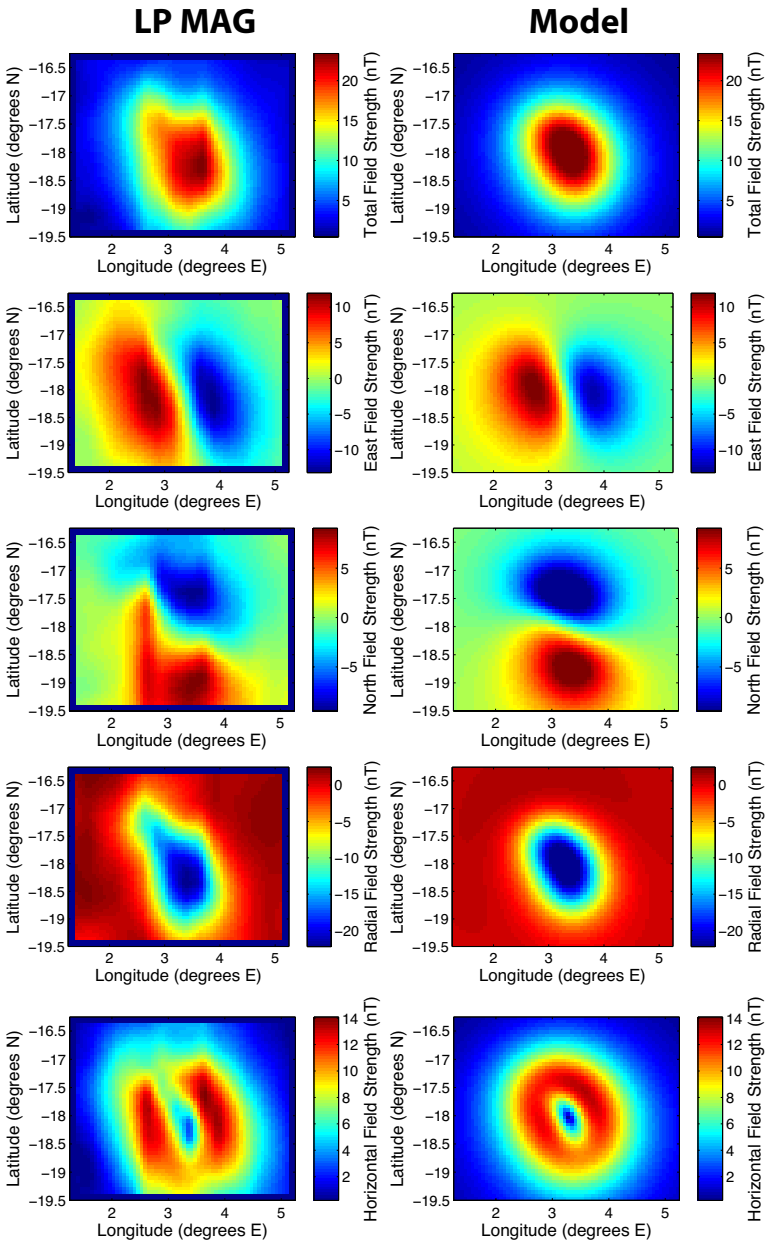

Figure 2.14: Comparison of the observed field at $\sim$ 18 km over Airy (left panels; derived from LP MAG data collected on days 49-50, 77, and 104 of 1999) and the model field (right panels; obtained as described in 2.4.2.1). Figure 2.13 shows the horizontal component of the model field predicted at the surface.

Winglee (2003) for a related discussion). As illustrated in Figure 2.1d, a horizontally magnetized source will produce strongly horizontal fields directly above the source while producing cusps (where the horizontal field strength drops to zero) on either side of the source. This suggests that the horizontally magnetized source material underlies the brightest parts of the Reiner Gamma albedo feature and that the dark lanes may be aligned with the cusps. The appearance of the two dark lanes and the relatively bright material between them may be explained by a superposition of two sources (see Figure 2.15 and compare with Figure 2.1).

As with the case illustrated in Figure 2.1 panels b and d, the field illustrated in Figure 2.15 is strongly horizontal at any altitude over the two horizontally magnetized sources. However, in this case there is an additional region of elevated horizontal field strength where the side lobes interfere constructively between the two sources. Taking this pattern as a cue, we replace the grid of dipoles described in section 2.4.1.5 with an array of 55 dipoles arranged as curvilinear structures beneath the three brightest parts of the swirl (Figure 2.16, left panel). In cross-section, the field pattern from the two approximately linear sources adjacent to the dark lanes resembles the pattern from the two-dipole case illustrated in Figure 2.15, but the cusps in the horizontal magnetic field profile are shifted outward slightly such that they are displaced laterally (in this case to the north and south) from the center of the sources by a distance equal to the altitude above the source rather than $1/\sqrt{2}$ times the altitude above the source (details are given in Appendix B). If we assume the dark lanes at Reiner Gamma (which are displaced $\sim 5\,\mathrm{km}$ from the centers of the bright lobes) are aligned with the cusps in the surface horizontal magnetic field profile, then the depth of the source must be $\sim 5\,\mathrm{km}$. Because

we assume infinitely narrow source structures, this represents the maximum possible source depth consistent with the hypothesis that the dark lanes align with cusps in the horizontal magnetic field profile. The LP MAG data are too spatially coarse to constrain the distribution of magnetic moments within the source structure so we assign equal strength to each of the 55 dipoles in the array. As with the Airy case, we perform a complete search to find the solution that best fits, in a least squares sense, the LP MAG data. The resulting best-fit solution has the dipoles pointed with inclination +2° and declination -8° (i.e., pointed nearly horizontally and slightly west of north) and total magnetic moment $1.0 \times 10^{13}\,\mathrm{Am}^2$ (Table 2.4). This source model produces a magnetic field pattern at the surface that mimics the morphology of the albedo anomaly, with the field being strongly horizontal in high albedo areas and vertical in the intra-swirl dark lanes (Figure 2.16). Remarkably, this same source model produces a field pattern at the spacecraft altitude that agrees with the Lunar Prospector observations (Figure 2.17).

2.5 Discussion

2.5.1 Magnetization

The models described in section 2.4.1 suggest that the source material is concentrated under the central parts of the albedo anomalies. Based on the source material distributions illustrated in Figures 2.8 and 2.10, we can compute the implied magnetizations at Airy and Reiner Gamma for various assumed layer thicknesses. Figure 2.18 illustrates that even when the magnetized layer is assumed to be 10 km thick, typical magnetizations at the Reiner Gamma

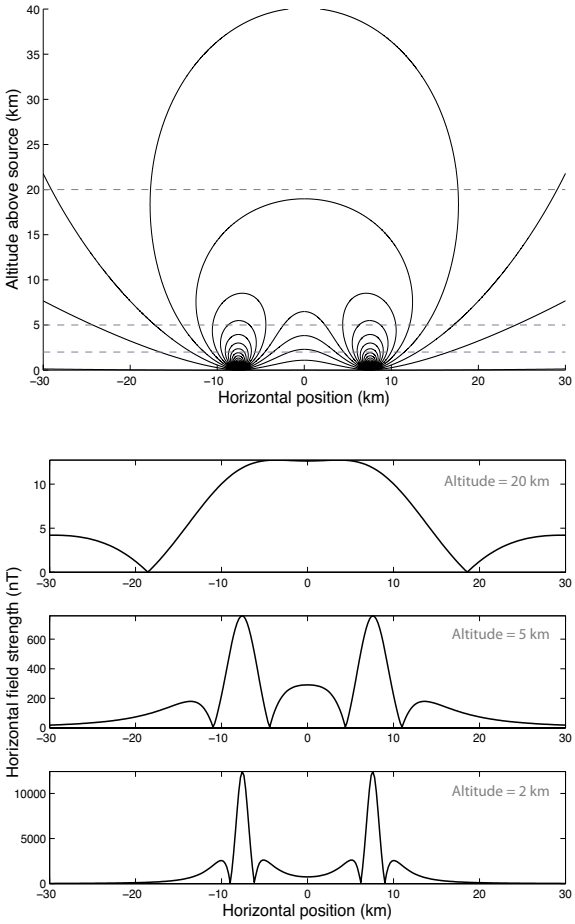

Figure 2.15: Upper panel: magnetic field lines due to a pair of dipoles separated by 15 km and oriented horizontally in the plane of the page; Lower panel: profiles of the horizontal component of the magnetic field shown at the various altitudes represented by dashed lines in the upper panel. Each of the dipoles has a magnetic moment of $10^{12}\,\mathrm{Am}^2$.

Albedo Pattern-Based Model for Reiner Gamma

Latitude (°N)	**Longitude** (°E)	**Latitude** (°N)	**Longitude** (°E)
7.649	301.460	7.073	301.143
7.673	301.418	7.056	301.079
7.693	301.371	7.043	301.014
7.710	301.320	7.035	300.949
7.723	301.264	7.031	300.884
7.731	301.205	7.031	300.820
7.735	301.144	7.035	300.759
7.735	301.080	7.043	300.700
7.731	301.015	7.056	300.644
7.723	300.950	7.073	300.593
7.710	300.885	7.093	300.546
7.693	300.821	7.117	300.504
7.673	300.759	7.542	301.774
7.649	300.700	7.538	301.819
7.622	300.645	7.543	301.878
7.592	300.593	7.555	301.943
7.559	300.546	7.573	302.001
7.525	300.505	7.593	302.043
7.488	300.469	7.612	302.062
7.451	300.439	7.628	302.056
7.315	301.525	7.636	302.024
7.278	301.495	7.637	301.973
7.241	301.459	7.629	301.910
7.207	301.418	7.615	301.847
7.174	301.371	7.596	301.794
7.144	301.319	7.576	301.759
7.117	301.264	7.557	301.749
7.093	301.205		

Table 2.4: Final dipole array model for Reiner Gamma as described in section 2.4.2.2 (Figure 2.16). The model consists of 55 dipoles at the indicated latitudes and longitudes, all buried 5 km below the surface. The total magnetic moment is $1.0 \times 10^{13}\,\mathrm{Am}^2$. All dipoles in the array have inclination 2°, measured positive downward from the horizontal and declination -8°, measured positive clockwise from north.

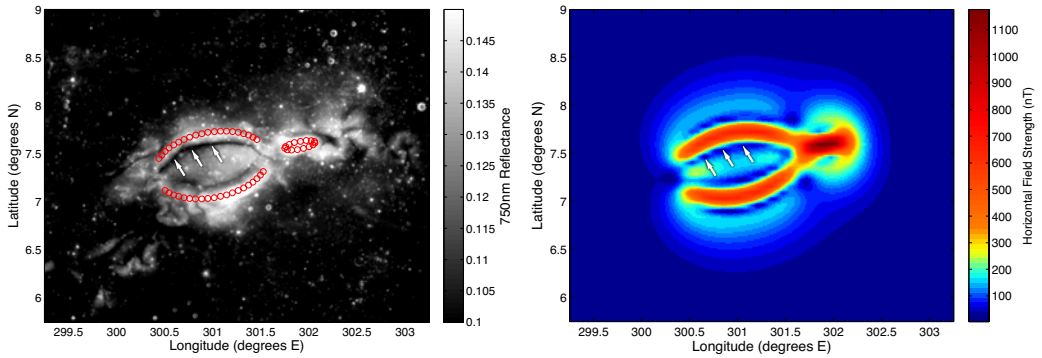

Figure 2.16: Left panel: Reiner Gamma study area showing Clementine albedo map with red circles indicating the locations of the source model's 55 dipoles; Right panel: resulting horizontal magnetic field strength predicted at the surface. White arrows indicate where field lines become vertical in one of the intra-swirl dark lanes. Figure 2.17 compares the model field predicted at the spacecraft altitude with the LP MAG observations.

anomaly are on the order of 1 A/m. If the magnetized layer is only 1 km thick, the implied magnetization approaches 10 A/m at Reiner Gamma. For comparison, *Nicholas et al.* (2007) predict a minimum magnetization of 1 A/m for a layer 1 km thick at Reiner Gamma and *Wieczorek et al.* (2012) calculate ~ 2 A/m for the same layer thickness assuming an anomaly that produces a 10 nT field at 30 km altitude. Terrestrial mid-ocean ridge basalts can have magnetizations of $\sim 1 - 6$ A/m (*Pariso and Johnson*, 1991) and the magnetic lineations in the Martian southern highlands require rock magnetization of ~ 20 A/m (*Connerney*, 1999), suggesting that our lower bounds for magnetization at the Airy and Reiner Gamma anomalies are reasonable. However, if we suppose the source structures are further horizontally concentrated, as the albedo-pattern-constrained models of section 2.4.2 suggest (Figures 2.13 and 2.16), the magnetizations would have to be even greater.

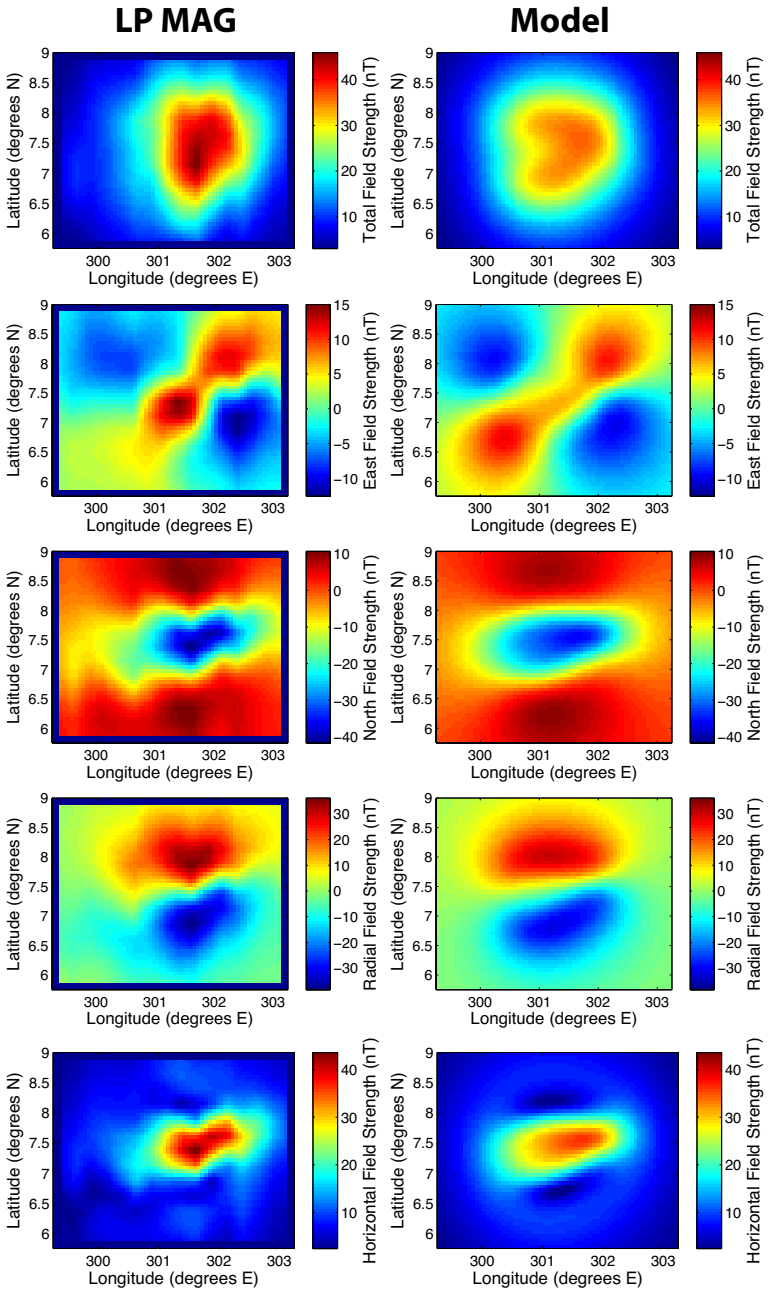

Figure 2.17: Comparison of the observed field at $\sim 18\,\mathrm{km}$ over Reiner Gamma (left panels; derived from LP MAG data collected on days 54, 81-82, and 109 of 1999) and the model field (right panels; obtained as described in 2.4.2.2). Figure 2.16 shows the horizontal component of the model field predicted at the surface.

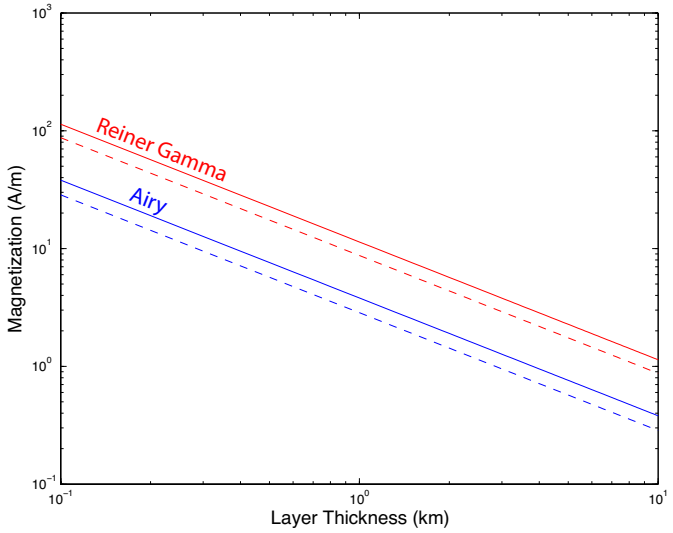

Figure 2.18: Rock magnetization implied by source models illustrated in Figures 2.8 and 2.10 versus assumed layer thickness. Solid lines are based on the maximum individual dipole moments found in those models ($\sim 2.1 \times 10^{11}$ Am^2 for Airy, $\sim 6.5 \times 10^{11}$ Am^2 for Reiner Gamma) and the dashed lines are based on characteristic values of 1.25×10^{11} Am^2 for Airy and 3.4×10^{11} Am^2 for Reiner Gamma.

2.5.2 Magnetizing Field

The strong magnetizations at the Airy and Reiner Gamma anomalies could be the result of the source material having cooled in a long lasting global magnetic field, perhaps generated by a core dynamo (*Garrick-Bethell et al.*, 2009; *Dwyer et al.*, 2011; *Le Bars et al.*, 2011; *Shea et al.*, 2012). As we have shown here, however, the Airy anomaly (located at approximately 17°S, 3°E) is magnetized with a steep downward inclination while the Reiner Gamma anomaly (located at approximately 7°N, 59°W) is magnetized with almost zero inclination and points approximately toward the north. If these two anomalies acquired their magnetizations by cooling in a dipolar dynamo field, they could not have formed contemporaneously. Instead, the two anomalies may have formed during different global field orientation epochs. Alternatively, the Moon's dynamo field may have had substantial higher order components

(i.e., beyond dipolar).

Another possibility that avoids the difficulties associated with inconsistent magnetization directions is that, rather than being the thermal remanent magnetization signatures of an extinct core dynamo, the Moon's crustal magnetic anomalies may instead be the result of shock remanent magnetization that occurs following basin-forming impact events when magnetohydrodynamic shock waves converge near the basin antipode producing strong transient fields and potentially magnetizing iron-rich ejecta materials (*Hood et al.*, 2001; *Halekas et al.*, 2001; *Richmond et al.*, 2005; *Hood and Artemieva*, 2008).

2.6 Conclusions

Our examination of swirls at Airy and Reiner Gamma, two magnetic anomalies with dissimilar orientation, suggests that magnetic field direction and swirl morphology are related in the way we predict based on the solar wind deflection hypothesis: the Reiner Gamma case delivers evidence that swirls are brightest where magnetic field lines are dominantly horizontal and the Airy case demonstrates a connection between dark lanes and vertically oriented field lines. These findings support the solar wind deflection model for swirl formation, implying that differential solar wind darkening is largely responsible for creating the albedo anomalies. Although our source models do not represent unique solutions, they agree with observational constraints while plausibly accounting for the alternating bright and dark bands at both Airy and Reiner Gamma. Our model results suggest that swirl morphology could potentially be used to infer small-scale structure in the near-surface magnetic field as well as the layout and burial depth of the magnetic source material. For Airy and

Reiner Gamma, we infer maximum source burial depths of $\sim 8\,\mathrm{km}$ and $\sim 5\,\mathrm{km}$, respectively, and horizontally concentrated sources with strong magnetizations ($\sim 10\,\mathrm{A/m}$ or greater for a layer 1 km thick). Examination of additional swirls may help to further our understanding of how magnetic field direction relates to swirl morphology, but ultimately, very near-surface magnetic field and solar wind flux measurements (i.e., from altitudes of hundreds of meters or less) will be required to confirm our predictions.

Acknowledgements

This research was performed as part of the World Class University Project at Kyung Hee University and sponsored by the Korean Ministry of Education, Science and Technology. Additional support was provided by the NASA Ames Research Center/University of California Santa Cruz University Affiliated Research Center. We would like to thank Lon Hood, Robert Lin, Jasper Halekas, Greg Delory, Robert Lillis, and Michael Purucker for their comments and suggestions and Joseph Nicholas for the data used to generate Figure 2.12.

Chapter 3

Latitudinal Variation in Spectral Properties of the Lunar Maria and Implications for Space Weathering

This chapter is a modified version of Hemingway, D. J., I. Garrick-Bethell, and M. A. Kreslavsky (2015), Latitudinal Variation in Spectral Properties of the Lunar Maria and Implications for Space Weathering, *Icarus* (in press).

Abstract

Space weathering alters the optical properties of exposed surfaces over time, complicating the interpretation of spectroscopic observations of airless bodies like asteroids, Mercury, and the Moon. Solar wind and micrometeoroids are likely the dominant agents of space weathering, but their relative contributions are not yet well understood. Based primarily on Clementine mosaics, we report a previously unrecognized systematic latitudinal variation in the near-infrared

spectral properties of the lunar maria and show that the characteristics of this latitudinal trend match those observed at 'lunar swirls', where magnetic fields alter local solar wind flux without affecting the flux of micrometeoroids. We show that the observed latitudinal color variations are not artifacts of phase angle effects and cannot be accounted for by compositional variation alone. We propose that reduced solar wind flux, which should occur both at swirls and toward higher latitudes, is the common mechanism behind these color variations. This model helps us quantify the distinct effects of solar wind and micrometeoroid weathering and could aid in interpreting the spectra of airless bodies throughout the solar system.

3.1 Introduction

'Space weathering' refers to the processes by which the optical properties of airless bodies change due to exposure to solar wind and micrometeoroid impacts. However, the difficulties of reproducing space-weathering conditions in the laboratory, or returning weathered samples to Earth, make it challenging to determine precisely how space weathering operates (*Pieters et al.*, 2000; *Hapke*, 2001; *Vernazza et al.*, 2009; *Pieters et al.*, 2012; *Domingue et al.*, 2014). Remote sensing measurements, studies of lunar samples, and laboratory experiments have established that solar wind ion and micrometeoroid bombardment weaken spectral absorption features and cause the lunar surface to darken and redden (increase in spectral continuum slope in the visible and near-infrared) with time. These changes appear to be due to some combination of the formation of impact glasses and agglutinates (*Adams and McCord*, 1971), the regolith's disintegration into increasingly finer soils (*Pieters et al.*, 1993), and

the accumulation of nanophase iron (*Hapke*, 2001; *Sasaki et al.*, 2001; *Noble et al.*, 2007). Larger impacts also expose fresh material, which then gradually matures until the reflectance spectrum reaches a steady state, which we call 'equilibrium color' for simplicity.

The equilibrium color varies considerably across the lunar surface, due primarily to differences in mineralogy. This is most obvious in the dichotomy between the bright, anorthositic highlands and the darker basaltic maria. However, as we will argue, the presence of 'lunar swirls' suggests that equilibrium color may also be influenced by the *flux* of weathering agents, rather than just their total accumulation (see sections 3.3.1 and 3.4). If this is the case, then equilibrium color may also vary with latitude. Both solar wind and micrometeoroids originate primarily from within the ecliptic plane, which is inclined from the Moon's equator by just 1.5°. Hence maximum flux of these weathering agents occurs near the equator, with flux decreasing as incidence angle increases towards the poles.

This paper's central observation is that, when we examine imagery from across the lunar surface, we find that the equilibrium color does vary systematically with latitude. In section 3.3.2, we show that this latitudinal color trend persists across a range of distinct compositions and that it is not an artifact of phase angle biases in the Clementine mosaics. Interestingly, the spectral properties of the latitudinal color trend match the characteristic color variation found at lunar swirls. In section 3.3.1, we quantify the characteristics of the swirl-related color variation and, in section 3.3.2, we show that it is statistically equivalent to the observed latitudinal color trends, with a transition toward higher latitudes being attended by the same color change that occurs towards brighter parts of swirls. Finally, in section 3.4, we argue that the best

candidate for a common mechanism behind these color variations is altered solar wind flux. We present a qualitative empirical model illustrating how this hypothesis comports with the observations and we discuss the possible implications with respect to the interpretation of spectral data, particularly at high latitudes.

3.2 Data Sources

In this study, we primarily use mosaics based on imagery from the 750 nm and 950 nm channels of the Clementine UVVIS (ultraviolet-visible) experiment (*Nozette et al.*, 1994; *Eliason et al.*, 1999), available from the USGS (www.mapaplanet.org). As a point of comparison, we also examine 1064 nm reflectance from the Lunar Orbiter Laser Altimeter (LOLA) experiment on board the Lunar Reconnaissance Orbiter (LRO) (*Lucey et al.*, 2014). In discussing the observed trends in the Moon's spectral properties, we may use the word 'color' in a general sense to refer to combinations of albedo and the ratio between 950 nm and 750 nm reflectance (e.g., as a proxy for continuum slope).

Parts of our analysis require isolating portions of the lunar surface according to composition and/or topographic roughness. For composition, we use results from the Lunar Prospector Gamma Ray Spectrometer (*Lawrence et al.*, 2002; *Prettyman et al.*, 2006), specifically in order to identify FeO and TiO_2 content in the regolith. The topographic roughness metric we use is the interquartile range of the along-profile second derivative of elevation, at 1.8-km baseline (*Kreslavsky et al.*, 2013), derived from Lunar Orbiter Laser Altimeter (LOLA) data. The latter is used to distinguish between the smooth maria and the rougher highlands.

3.3 Analysis

Before discussing the observed latitudinal color variation, we revisit the characteristic color signature observed at swirls, developing a new parameterization that will allow for a quantitative comparison between swirls and the newly observed latitudinal trends.

3.3.1 Color Variation at Lunar Swirls

Lunar swirls are enigmatic collections of sinuous bright markings, often interposed with narrow dark lanes, that are co-located with many of the Moon's crustal magnetic anomalies (Figure 3.1A). The bright parts of swirls superficially resemble optically immature surfaces such as fresh impact craters (*Lucey et al.*, 2000a; *Wilcox et al.*, 2005; *Blewett et al.*, 2011). However, it has been shown (*Garrick-Bethell et al.*, 2011) that swirls exhibit spectral trends that are distinct from those associated with impact-related brightening (*Lucey et al.*, 2000a). The two trends can be distinguished from one another, using Clementine UVVIS (ultraviolet-visible) mosaics (*Nozette et al.*, 1994; *Eliason et al.*, 1999), by plotting 750 nm reflectance against the 950 nm to 750 nm reflectance ratio (*Garrick-Bethell et al.*, 2011; *Blewett et al.*, 2011), the former representing albedo and the latter serving as a proxy for both the near-infrared continuum slope and the 1 μm absorption feature found in iron-bearing silicate minerals. Both the swirl- and impact-related color variations involve changes in both albedo and the 950 nm/750 nm band ratio, but the impact-related variation is accompanied by a proportionally greater change in the 950 nm/750 nm band ratio (Figure 3.1B), as originally reported by *Garrick-Bethell et al.* (2011).

In order to establish a quantitative basis for comparison with the latitu-

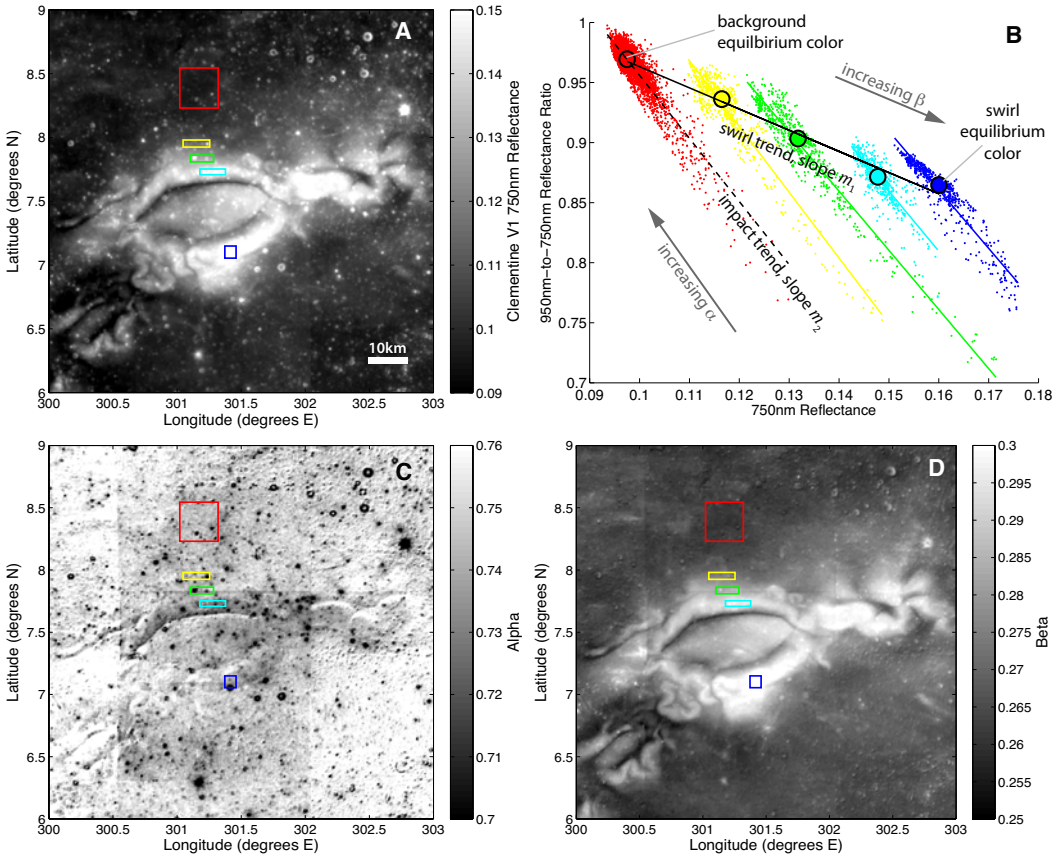

Figure 3.1: (A) 750 nm reflectance (albedo) at the Reiner Gamma swirl. (B) Spectral characteristics (albedo versus 950 nm/750 nm band ratio) of pixels sampled from the five rectangular boxes, with corresponding colors, in (A). The red point cloud corresponds to a representative background region whereas the dark blue point cloud corresponds to the brightest part of the swirl. Each of the point clouds displays a steep trend that follows the progression from fresh impact craters (lower right part of each point cloud) to darker background soils (upper left part of each point cloud); the dashed black line is a best fit through the red point cloud and, averaging over three separate mare swirl areas, has a slope of $m_2 = -5.7 \pm 0.5$. The black circles represent the steady state (equilibrium) colors reached with maximum optical maturity in each rectangle (since the majority of pixels are likely near saturation maturity, we take the median point in each cluster to represent the equilibrium color). The solid black line is a best fit through the centroids (black circles) of each cluster and has a slope of $m_1 = -1.6 \pm 0.2$, averaged over the three separate mare swirl areas. (C) and (D) are maps of the α and β parameters, defined according to equations (3.1) and (3.2), respectively.

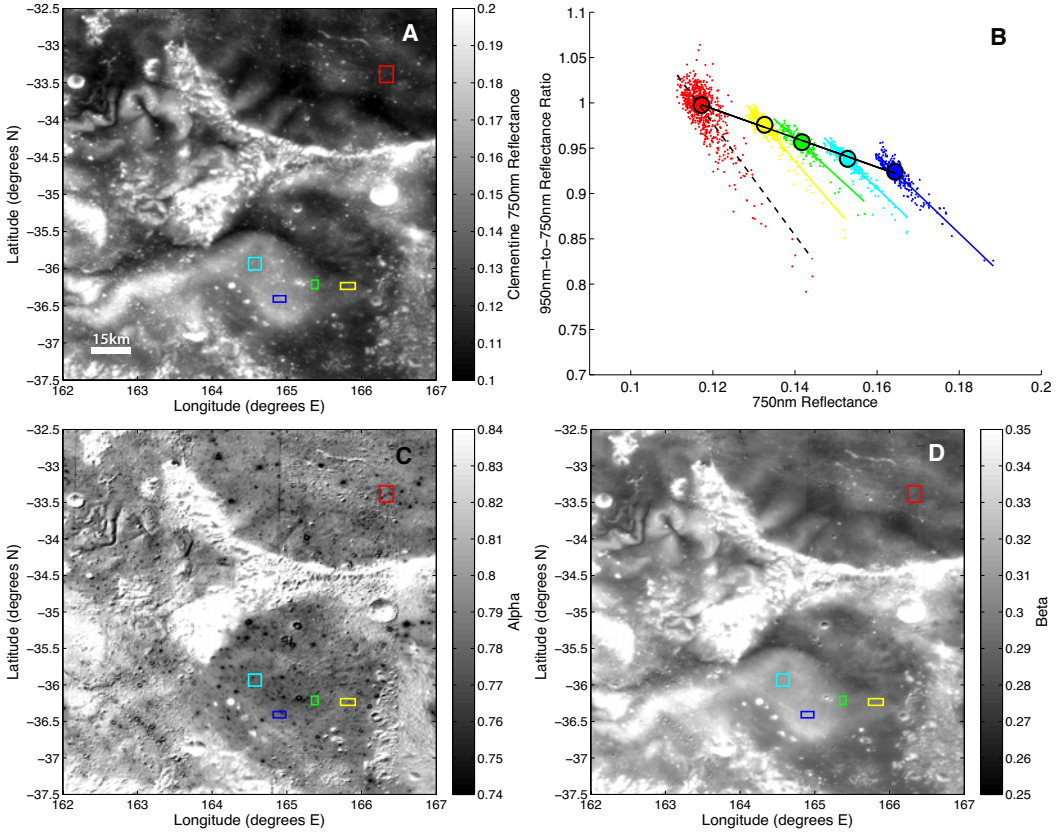

Figure 3.2: (A) 750 nm reflectance at the Ingenii swirl. (B) Spectral characteristics (albedo versus 950 nm/750 nm band ratio) of pixels sampled from the five rectangular boxes, with corresponding colors, in (A). (C) and (D) are maps of the α and β parameters, defined according to equations (3.1) and (3.2), respectively.

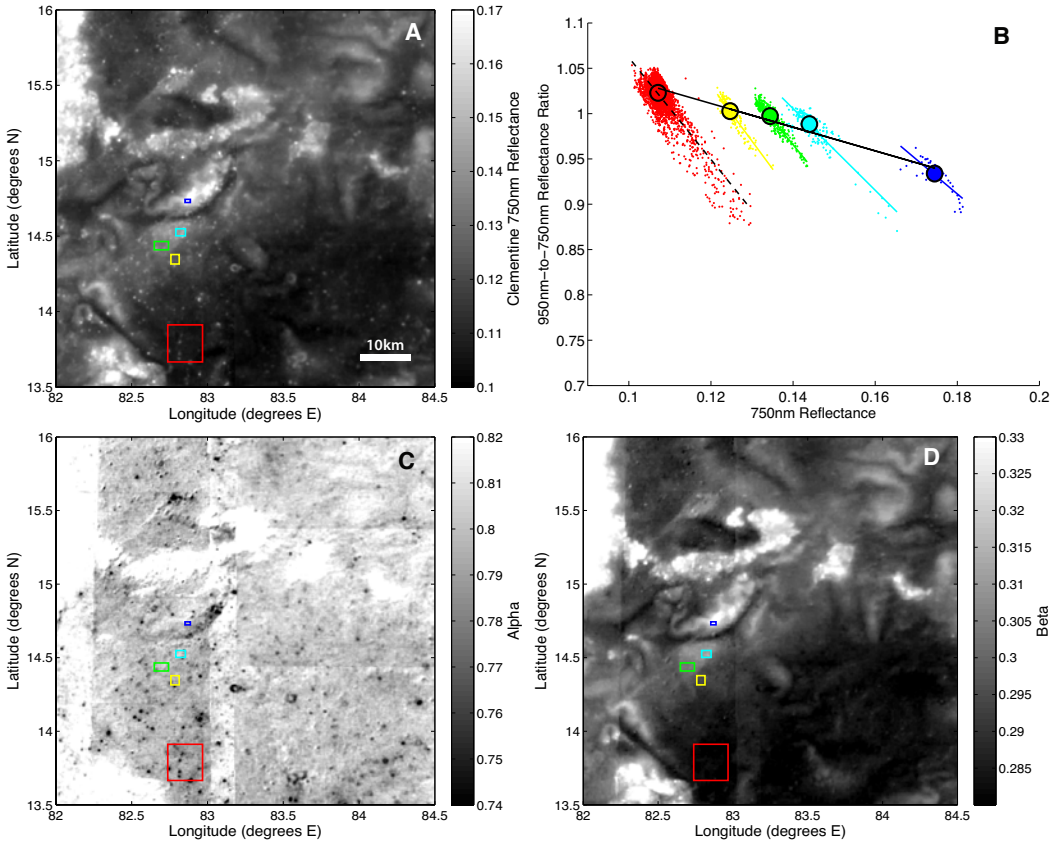

Figure 3.3: (A) 750 nm reflectance at the Marginis swirl. (B) Spectral characteristics (albedo versus 950 nm/750 nm band ratio) of pixels sampled from the five rectangular boxes, with corresponding colors, in (A). (C) and (D) are maps of the α and β parameters, defined according to equations (3.1) and (3.2), respectively.

dinal trends we discuss in section 3.3.2, we parameterize the color variations that are characteristic of swirls, averaging over three different mare swirl areas: Reiner Gamma in western Oceanus Procellarum, Mare Ingenii on the farside, and Mare Marginis on the eastern limb. In each case, in the albedo versus band ratio diagrams, we found similar steep trends associated with the transition between impact craters and background soils, and shallower trends associated with the transition between dark and bright parts of swirls (Figure 3.1B, Figure 3.2B, Figure 3.3B), in accord with *Garrick-Bethell et al.* (2011). The distinct color variations associated with impacts and swirls allow us to define parameters that clearly separate the two trends (Figure 3.1C and D). The impact-related progression from bright craters to the more mature background soils can be characterized by an impact maturity parameter

$$\alpha = R_{750} - \left(\frac{R_{950}}{R_{750}}\right)/m_1 \tag{3.1}$$

where R_{750} and R_{950} are the Clementine 750 nm and 950 nm reflectances, respectively, and where

$$m_1 = -1.6 \pm 0.2$$

is the slope of the swirl-related trends ($\pm 1\sigma$), averaged from the three separate mare swirl areas. The swirl-related trend slope is used in equation (3.1) so that impact maturity (α) is not affected by swirl-related color variations. Equation (3.1) resembles previously developed optical maturity parameters (*Lucey et al.*, 2000a; *Wilcox et al.*, 2005) except that here, the goal is explicitly to isolate the impact-related color variation from that associated with swirls, and so the constants are different. Similarly, we can represent the swirl-related color

variation, which we regard as distinct from optical maturity, as

$$\beta = R_{750} - \left(\frac{R_{950}}{R_{750}}\right)/m_2 \tag{3.2}$$

where

$$m_2 = -5.7 \pm 0.5$$

is the typical slope of the impact-related trends ($\pm 1\sigma$). The impact-related trend slope is used in equation (3.2) so that β is not affected by impact-related color variations.

Although the α and β values vary according to local composition, the slopes of the impact- and swirl-related trends do not vary significantly across different mare regions. The values given here for m_1 and m_2 are therefore largely composition independent, at least within the maria. The α parameter is designed to have constant values along the swirl-related trends such that swirl features do not influence the value of α and so maps generated for the α parameter show impact features but not swirl features (Figure 3.1C). Conversely, the β parameter is designed to have constant values along the impact-related trends such that maps of the β parameter highlight swirl features while muting impact features (Figure 3.1D).

3.3.2 Latitudinal Color Variation

When we examine imagery from across the lunar surface, we find that the reflectance spectra vary systematically with latitude. The effect is not obvious when we examine the Moon as a whole, likely because the spectra are so strongly affected by composition, which varies considerably across the surface.

However, when we account for variations in composition, the latitudinal trends emerge. As we will show, the latitudinal trends are especially pronounced within the maria, and may help to account for the unusually high albedo of Mare Frigoris—the highest latitude mare region.

Color anomalies have been identified previously in polar regions (*Yokota et al.*, 2011; *Zuber et al.*, 2012) and latitudinal variation in space weathering has been considered previously (*Yokota et al.*, 2011; *Hendrix et al.*, 2012), however, this is the first observation of a broad systematic latitudinal color trend that is visible across the lunar maria. Moreover, the spectral characteristics of this trend match those found at lunar swirls (section 3.3.1), suggesting a link between the two phenomena that may be helpful for understanding space weathering (see section 3.4).

In addition to controlling for composition, below we examine the possible contributing effects of highland contamination in the maria and phase angle biases in the Clementine mosaics; we show that the observed latitudinal trends cannot be artifacts of such effects.

3.3.2.1 Effect of Composition

Because surface color is strongly affected by composition, we separate the data into bins according to TiO_2 and FeO content (as measured by the Lunar Prospector Gamma Ray Spectrometer (*Lawrence et al.*, 2002; *Prettyman et al.*, 2006)), and examine the spectral characteristics separately for each compositional bin. Figure 3.4A shows, in the same parameter space we used to characterize swirls, that pixels sampled from higher latitudes tend to have higher albedo (750 nm reflectance) and lower 950 nm to 750 nm band ratios, than those sampled from lower latitudes.

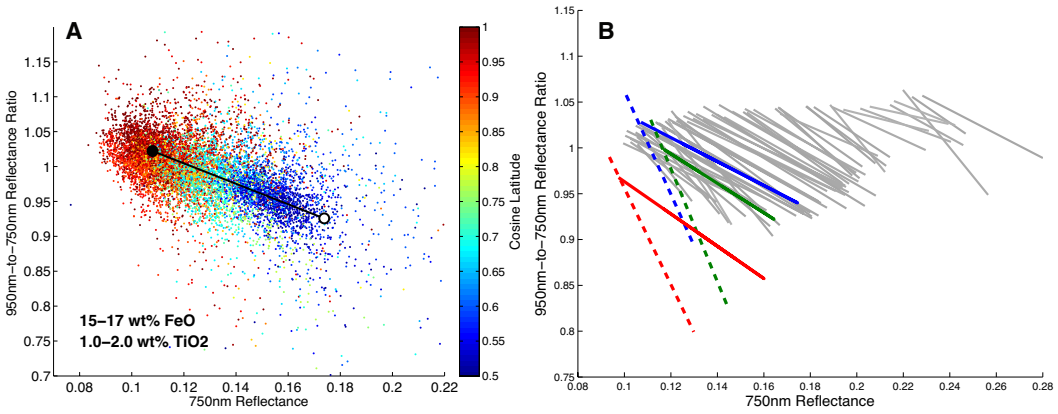

Figure 3.4: Color variation as a function of latitude. (A) Spectral characteristics of pixels sampled from regions with between 15 and 17 wt% FeO and between 1 and 2 wt% TiO_2. Points are color-coded according to cosine latitude, illustrating that the optical characteristics of the surface vary systematically with latitude. Equatorial regions (red points) tend to have lower albedo and higher 950 nm/750 nm reflectance ratios than regions farther from the equator (blue points). The black trend line represents a least squares best fit through the data points. The solid black circle corresponds to the color predicted by the best-fit line at the equator and the white circle represents the color predicted at latitudes of $\pm 70^{\circ}$. (B) Compilation of the 59 latitudinal trends we examined (grey lines), one for each compositional bin, compared with the trends discussed in section 3.3.1: the solid red, green and blue lines represent the swirl-related color trends observed at Reiner Gamma, Ingenii, and Marginis, respectively; the dashed lines represent the impact-related color trends observed at each of those swirls.

While Figure 3.4A shows just one illustrative example, we examined all combinations of FeO and TiO_2 content using bins of 2 wt% width in FeO and 1 wt% width in TiO_2, set at half bin width increments (see Figure 3.5 for additional examples). Because the latitudinal trend can only emerge if pixels are sampled from a wide range of latitudes, we discard compositional bins whose pixels do not reach latitudes of at least $\pm 50^\circ$ or do not span at least 50 total degrees of latitude. To ensure that slopes are estimated from robust samples only, we also discard bins whose pixels cover less than 0.25% of the lunar surface. Finally, to avoid artifacts in the Clementine mosaics that are related to severe illumination conditions at high latitudes, we also discard data within 20° of the poles. After applying these selection criteria, 59 compositional bins were retained for analysis. Figure 3.4B shows a summary of all 59 latitudinal trend lines (grey lines) along with the swirl- and impact-related trends discussed in section 3.3.1.

The effect of iron content is apparent when the trend lines are color-coded by weight % FeO, as determined by the Lunar Prospector Gamma Ray Spectrometer (*Lawrence et al.*, 2002) (Figure 3.6). Lower iron regions (pale orange lines) tend to plot farther up and to the right in Figure 3.6, in accord with *Wilcox et al.* (2005), whereas high iron regions (dark lines) plot farther down and to the left. This means that both α and β tend to be larger for low iron regions (in section 3.3.2.5, we discuss the implications of this observation with respect to highland contamination).

Although the latitudinal trend slopes are largely similar across different compositional bins, they become less consistent when iron content is very low, such as in the highlands. This is not surprising given that several studies suggest that the production of nanophase iron plays an important role in space

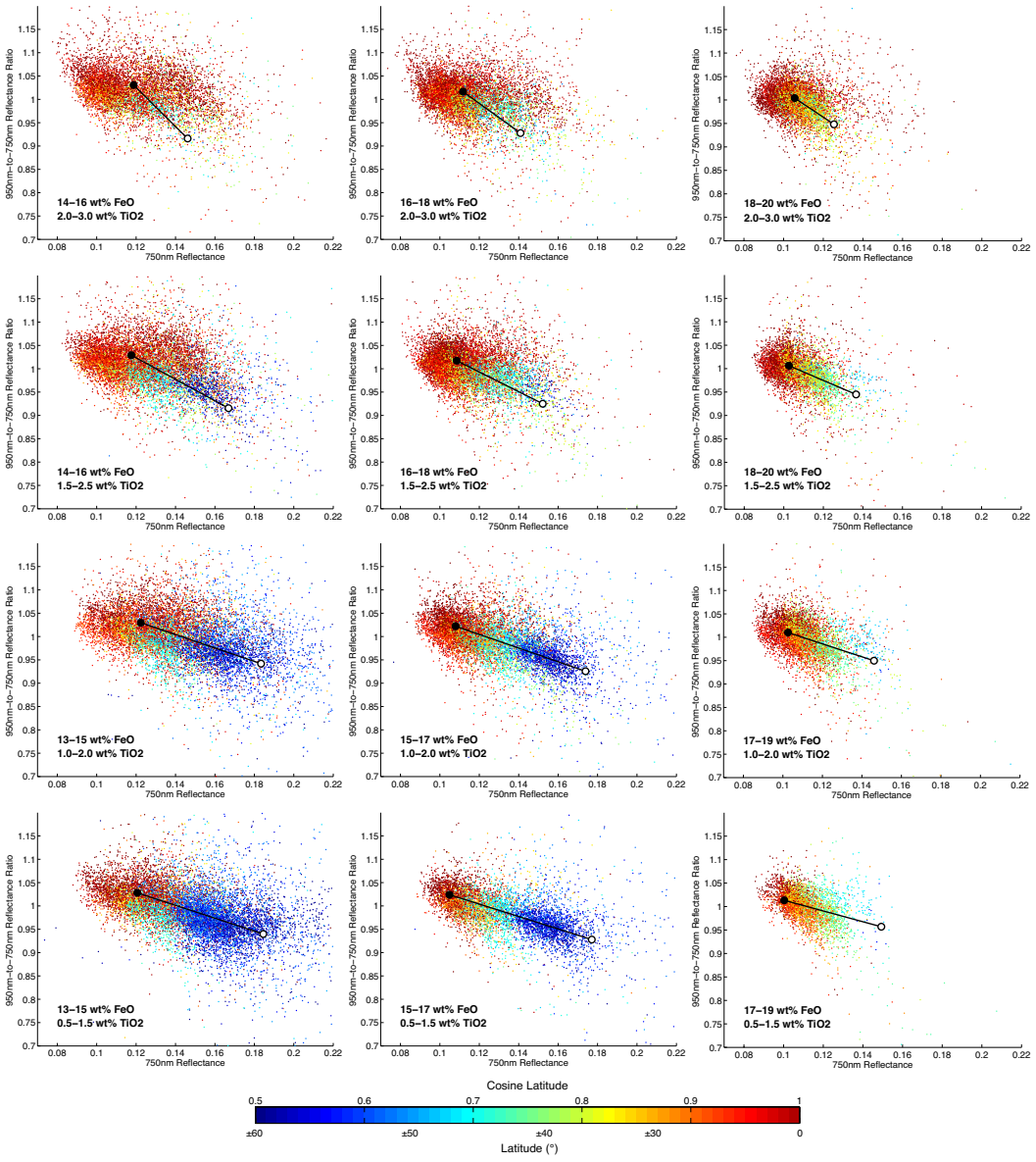

Figure 3.5: Latitudinal color variation across 12 distinct compositional bins. Equatorial regions (red points) tend to have lower albedo and higher 950 nm/750 nm reflectance ratios than regions farther from the equator (blue points). Each of the black trend lines represents the best-fit color variation between the equator (solid black circle) and latitudes of ±70° (white circle). Although only 12 are shown here, we examined 59 compositional bins in total.

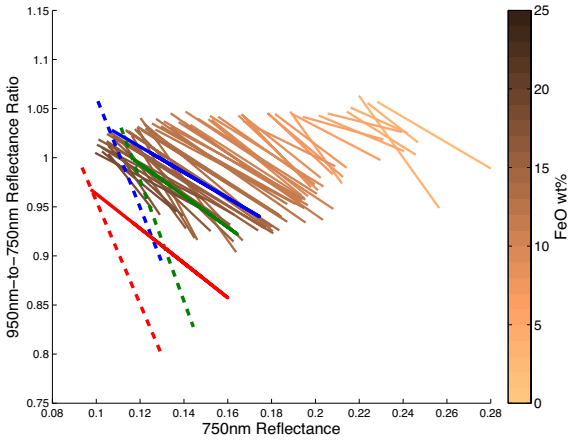

Figure 3.6: Compilation of latitudinal trend lines for all 59 compositional bins, color-coded by iron content (*Lawrence et al.*, 2002). Dark trend lines correspond to high iron bins while pale trend lines correspond to low iron bins. For comparison, the swirl- and impact-related trends are also shown: the solid red, green and blue lines represent the swirl-related color trends observed at Reiner Gamma, Ingenii, and Marginis, respectively; the dashed lines represent the impact-related color trends observed at each of those swirls.

weathering (*Hapke*, 2001; *Sasaki et al.*, 2001; *Noble et al.*, 2007). A paucity of iron in the highlands may prevent a clear appearance of the type of latitudinal trends we observe in the maria. In order to obtain as clear a signal as possible, we therefore focus our subsequent analysis on the maria.

3.3.2.2 Isolation of the Maria

Because the latitudinal trends are most consistent within the maria, and because we are interested in comparing these trends with the spectral characteristics we analyzed for three mare-based swirls (section 3.3.1), we restrict the remainder of our analysis to the lunar maria.

As previously discussed, we use Lunar Prospector Gamma Ray Spectrometer (GRS) data to determine both iron and titanium content in the soils we examine. Unfortunately, in comparison to the Clementine data, the relatively

coarse resolution of the GRS data (the effective footprint is roughly 45 km wide (*Lawrence et al.*, 2002)) means that we cannot use GRS-based iron estimates to isolate the maria—choosing a conservatively high threshold for iron content would result in the exclusion of significant portions of the maria, while choosing a low threshold would result in the inclusion of highland pixels. Inclusion of low-iron highland pixels is undesired as it could artificially skew the spectral characteristics towards higher 750 nm reflectance and higher 950 nm/750 nm reflectance ratios (see Figure 3.6 and section 3.3.2.5).

We cannot isolate the maria using iron estimates obtained from Clementine-based spectral techniques (e.g., (*Lucey et al.*, 2000b; *Wilcox et al.*, 2005)) because these techniques rely on the same parameter space we use in our own spectral analysis, namely 750 nm reflectance versus the 950 nm/750 nm reflectance ratio. Attempting to isolate the maria according to such spectral-based iron estimates would necessarily bias our results, artificially altering the slope of the best-fit latitudinal trends shown in Figure 3.4.

To distinguish mare from highland terrain, we instead adopt an independent metric that characterizes topographic roughness at 1.8-km baseline (*Kreslavsky et al.*, 2013). A histogram of the topographic roughness (Figure 3.7) shows a bimodal distribution, reflecting the dichotomy of kilometer-scale roughness between smoother maria and rougher highlands, with maria peaking at a roughness value of $2.3\,\mathrm{m/km^2}$ and highland terrain peaking at a roughness value of approximately $19\,\mathrm{m/km^2}$. We identify mare terrain as areas exhibiting roughness values below $5\,\mathrm{m/km^2}$. After applying a de-speckling filter, designed to remove isolated features less than approximately one degree in diameter, we obtain a mask that we use to exclude non-mare pixels from our subsequent analysis. Figure 3.8 illustrates the boundaries of our mare mask.

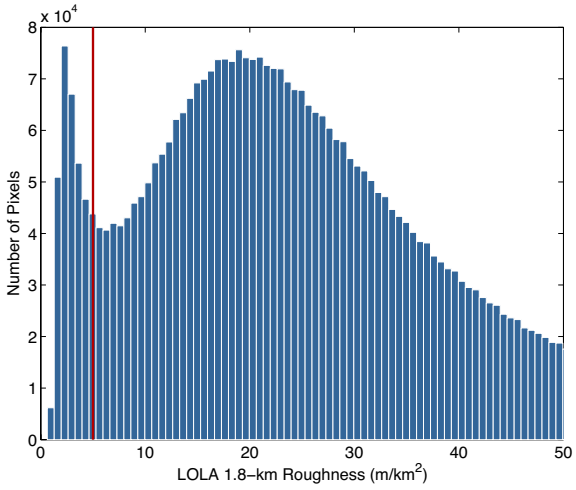

Figure 3.7: Histogram of topographic roughness with red line indicating the threshold below which we consider pixels to belong to the lunar maria; pixels above the threshold are discarded in our subsequent analysis.

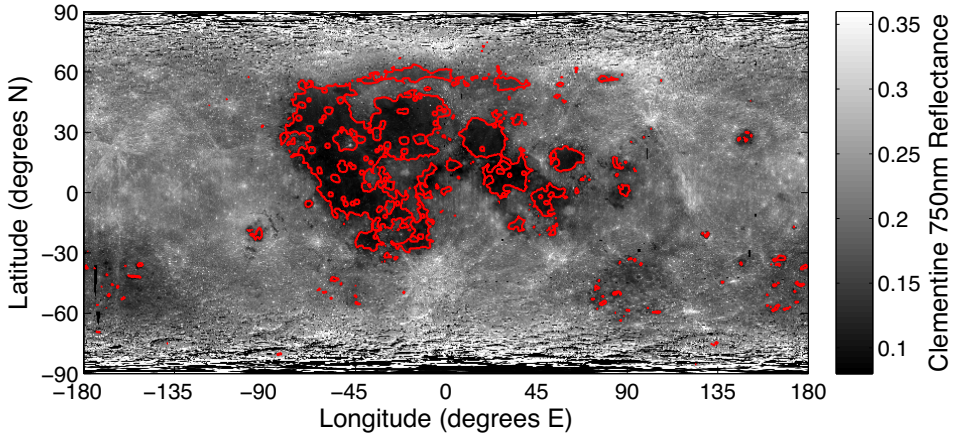

Figure 3.8: Clementine 750 nm reflectance with red lines indicting the boundaries of the mare regions as identified by our topographic roughness criterion (regions with less than 5 m/km^2 roughness at 1.8-km baseline).

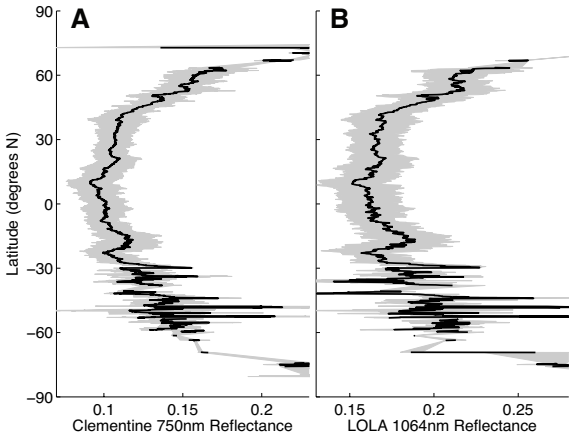

Figure 3.9: (A) Clementine 750 nm reflectance profile across the lunar maria (as identified by surface roughness, see Figure 3.8). (B) Profile of LOLA 1064 nm reflectance for the same region. In both profiles, reflectance tends to be lowest near the equator and higher towards higher northern and southern latitudes. The black lines and grey bands represent the mean and standard deviation at each latitude.

After excluding data from the lunar highlands, a clear latitudinal trend emerges in the Clementine 750 nm reflectance profile (Figure 3.9A): mare surfaces are darkest near the equator and become increasingly bright towards higher latitudes, with the profile being approximately symmetric about the equator. This is a straightforward visualization of the latitudinal trend and allows for simple comparison with different datasets (e.g., reflectance from the Lunar Orbiter Laser Altimeter; see section 3.3.2.6 and Figure 3.9B), but in order to facilitate comparison with the swirl-related spectral trends, we now return to plots of 750 nm reflectance versus the 950 nm/750 nm reflectance ratio.

3.3.2.3 Comparison with Swirl Trends

After excluding the highlands, 28 of the original 59 compositional bins survive the selection criteria we described in section 3.3.2.1. Figure 3.10 illustrates not only that the latitudinal color trends persist across a range of different compo-

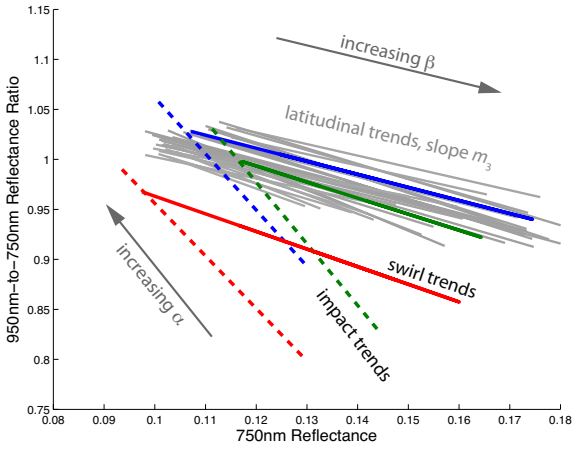

Figure 3.10: Summary of latitudinal trend lines (grey lines) for the 28 compositional bins that correspond to the maria. The solid red, green and blue lines represent the swirl-related color trends observed at Reiner Gamma, Ingenii, and Marginis, respectively. The dashed lines represent the impact-related color trends observed at each of those swirls. The latitudinal trends have slopes of -1.5 ± 0.3, whereas the swirl-related trends have slopes of -1.6 ± 0.2.

sitions, but also that these trends are remarkably similar to those associated with lunar swirls. That is, low latitude regions tend to have lower albedo and higher 950 nm/750 nm band ratios when compared with high latitude regions, and these changes occur in the ratio $m_3 = -1.5 \pm 0.3$, a slope that is indistinguishable from the swirl-related slope, $m_1 = -1.6 \pm 0.2$, at the one-sigma level (Figure 3.11). Figure 3.12 further demonstrates this result by showing that a transition to higher latitudes is attended by the same type of color change that occurs towards brighter parts of swirls (Figure 3.1D)—that is, increasing β.

3.3.2.4 Mare Frigoris

Mare Frigoris, spanning much of the near side at roughly 60°N, is the highest latitude and visibly brightest mare region, meaning that it makes a significant contribution to the latitudinal trend we observe (Figure 3.12). The high β

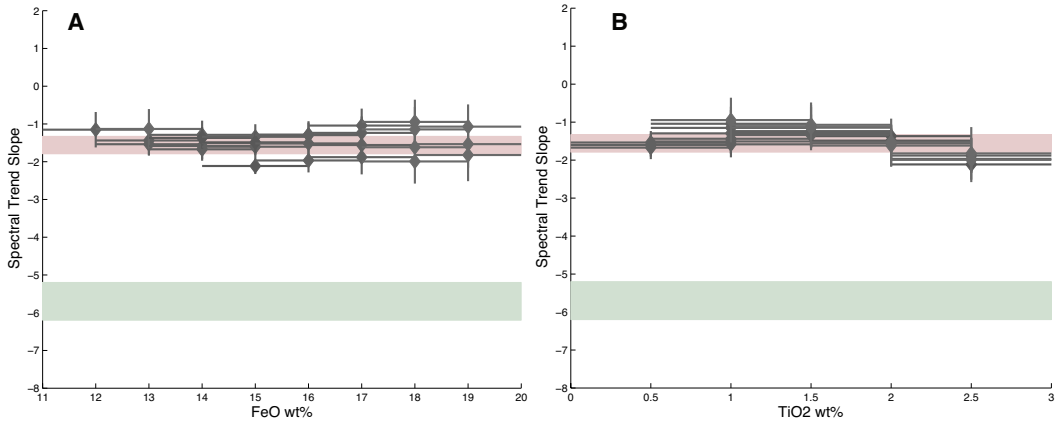

Figure 3.11: Latitudinal trend slopes (crosshairs) compared with swirl trend (pale red band) and impact trend (pale green band) slopes (with $\pm 1\sigma$ variability illustrated by the width of each band). All 28 mare-based slope estimates (the same trends illustrated in Figure 3.10) are shown versus the FeO bins (A) and the TiO_2 bins (B). In each case, the crosshairs show the width of the FeO or TiO_2 bin and the $\pm 1\sigma$ uncertainty on the estimated slope.

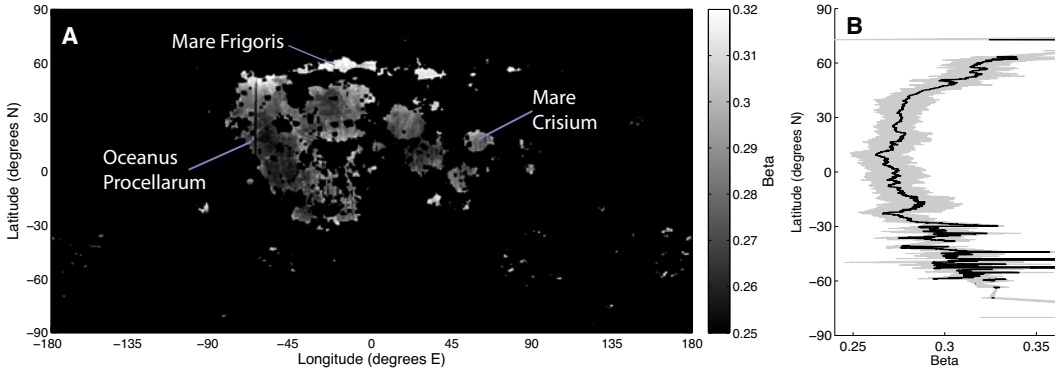

Figure 3.12: (A) Map of β, computed according to equation (3.2), over the lunar maria (as identified by surface roughness, see section 3.3.2.2). (B) Latitudinal profile of β across the lunar maria. The black line and grey band represent the mean and standard deviation at each latitude, averaged over all longitudes.

(high albedo and low 950 nm/750 nm band ratio) of Mare Frigoris could be attributed in part to its low FeO and TiO_2 content (*Lucchitta*, 1978; *Pieters*, 1978; *Staid and Pieters*, 2000). However, the FeO and TiO_2 abundances typical of Mare Frigoris (14±2 wt% FeO; 0.9±0.4 wt% TiO_2, see crosshairs in Figure 3.13A) are also found in lower latitude mare regions, which, by comparison, appear darker and have higher 950 nm/750 nm band ratios (and therefore lower β). The albedo and band ratio of Mare Frigoris differ significantly from those of low-latitude maria of equal composition (Figure 3.13B, see also lower left panel in Figure 3.5).

Given that Mare Frigoris is apparently compositionally unexceptional, its spectral characteristics cannot be attributed merely to low FeO and TiO_2 content. While it remains possible that they are the result of anomalous surface contamination (see section 3.3.2.5), our results suggest that the high albedo and low 950 nm/750 nm band ratio of Mare Frigoris are better understood as part of the broad latitudinal trend we observe across the lunar maria. Although Mare Frigoris accounts for an important component of the observed latitudinal trend, the analysis is not significantly affected by its removal (Figure 3.14). After manually removing those mare pixels belonging to Mare Frigoris, five of the original 28 compositional bins must be excluded from analysis due to their reduced area and latitudinal span, leaving a total of 23 bins. After Mare Frigoris is removed, fewer high latitude pixels are included. Nevertheless, the latitudinal trends remain, and the estimated latitudinal trend slope is unaffected ($m_3 = -1.5 \pm 0.3$ with or without Mare Frigoris). Hence, anomalous spectral characteristics of Mare Frigoris alone cannot account for the latitudinal color trend, but the latitudinal color trend *can* account for the spectral characteristics observed at Mare Frigoris.

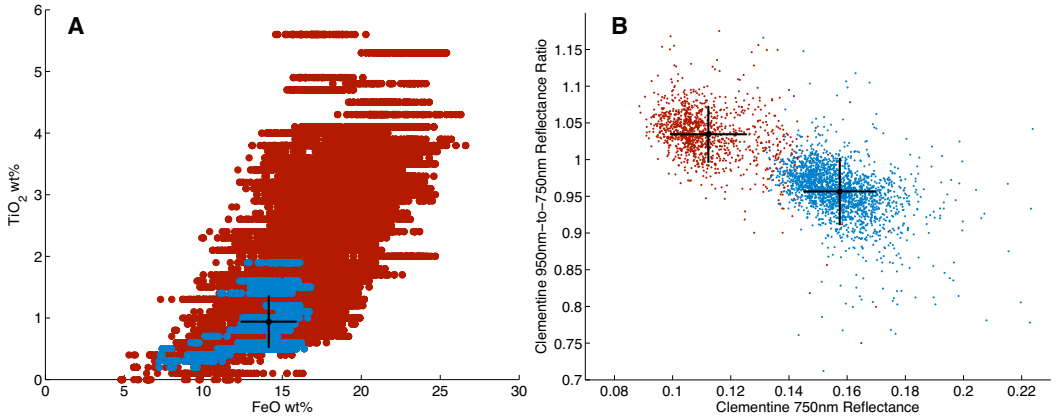

Figure 3.13: (A) FeO and TiO_2 content (based on Lunar Prospector Gamma Ray Spectrometer data (*Lawrence et al.*, 2002; *Prettyman et al.*, 2006)) of Mare Frigoris (blue points) compared to other mare regions (red points). The black crosshairs illustrate the mean and standard deviation FeO and TiO_2 abundances for Mare Frigoris (14±2 wt% FeO; 0.9±0.4 wt% TiO_2). (B) Pixels from Mare Frigoris (blue points) have higher albedo and lower band ratio than low latitude mare regions (red points, restricted to within ±15° of the equator) of equal composition. The mean and standard deviation of each cluster is marked with crosshairs.

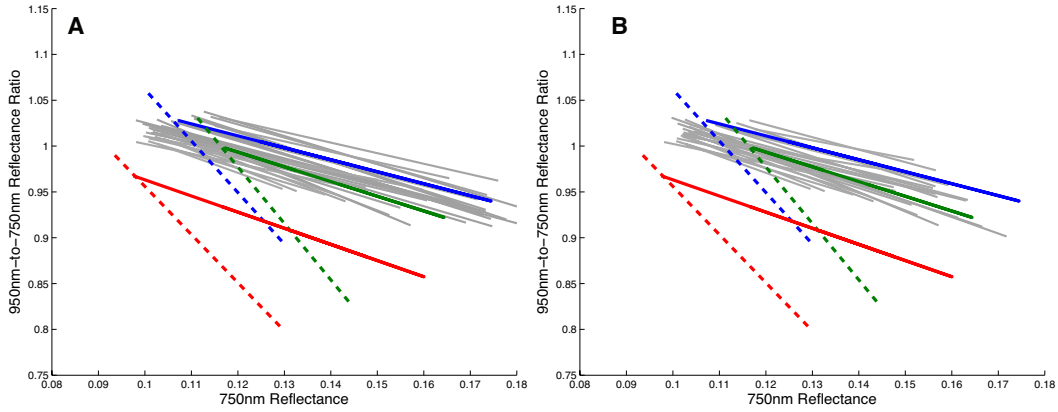

Figure 3.14: Comparison of latitudinal trends with and without pixels from Mare Frigoris. (A) Summary of all 28 mare-based latitudinal trend lines, including data from Mare Frigoris. (B) Summary of the 23 mare-based latitudinal trend lines that remain after Mare Frigoris pixels are excluded. The mean slope differs by less than 0.04 between the two cases (much less than $1\sigma = 0.3$). In both cases, the swirl- and impact-related trends are shown for comparison as solid and dashed lines, respectively.

3.3.2.5 Highlands Contamination

Diffusive contamination near mare/highland boundaries and contamination from major crater rays could be partly responsible for the latitudinal trends we observe if, by chance, such contamination occurs preferentially at higher latitudes, and if it produces the same relative changes in albedo and the 950 nm/750 nm band ratio. Here, we examine these factors and conclude that their contributions to the observed latitudinal trend are not significant.

Impact-induced diffusive mixing of highland and mare materials occurs near the mare/highland boundaries, and may be significant within 10–20 km of the boundary (*Mustard et al.*, 1998). The edges of the maria may therefore be relatively bright compared with other mare regions of similar underlying composition. If the morphology of high latitude mare regions is such that their perimeter length to surface area ratios tend to be larger (e.g., Mare Frigoris is narrow compared with Mare Imbrium), the amount of highland contamination may be relatively greater at high latitudes, potentially contributing to the latitudinal color trends we observe. If true, this would imply that the color variation we observe for any given compositional bin (e.g., Figure 3.4A) is, to some extent, a function of each pixel's distance from the nearest highlands, with pixels close to the highlands being brighter than pixels that are farther from the highlands, where contamination is weaker.

We test this hypothesis in two ways. First, we restrict our latitudinal color trend analysis to mare regions that are at least 50 km from the nearest highlands. *Mustard et al.* (1998) show that diffusive mare-highland mixing is significant only within <10 km of the mare-highland boundary and they find no evidence for mixing beyond 40 km from the boundary. We use the great-

circle distance (in kilometers) from the center of each mare pixel to the center of its nearest highland neighbor pixel, where mare/highland surfaces are identified according to our topographic roughness metric (see section 3.3.2.2). After excluding mare regions within 50 km of the nearest highlands, and again applying the selection criteria described in section 3.3.2.1, only 13 compositional bins remain. The surface area coverage is considerably more limited than in our full-mare analysis (Figure 3.10), but the resulting latitudinal trend slopes (-1.2 $\pm$0.3) are not significantly different (see Figure 3.15A and B and compare with Figure 3.4). Note that the 50-km threshold we use here is also larger than the Lunar Prospector Gamma Ray Spectrometer footprint ($\sim$ 45 km), helping to improve the compositional accuracy of the bins.

As a further test, we once again plot 750 nm reflectance versus the 950 nm/750 nm reflectance ratio, except that in this case, we color-code points not by cosine latitude, but instead by each pixel's distance from the highlands, from 50 km up to 100 km (Figure 3.15C). No significant color trend is obvious in Figure 3.15C and a least squares best fit line through the data (black line) predicts only a slight tendency for pixels 50 km from the mare/highland boundary (white circle) to be brighter than pixels 100 km from the boundary (black circle). This is not to say that mare pixels are not typically brighter near mare/highland boundaries, only that (within a given compositional bin) this effect is relatively small compared to the effect of varying latitudes (Figure 3.15A). While Figure 3.15C shows just one illustrative example, we repeated this analysis for each of the 13 compositional bins described above. The resulting highland-distance trends do not resemble the latitudinal trends and, in some cases, even oppose them (Figure 3.15D). Across the 13 bins, the highland-distance color trends are often poorly determined (large uncertain-

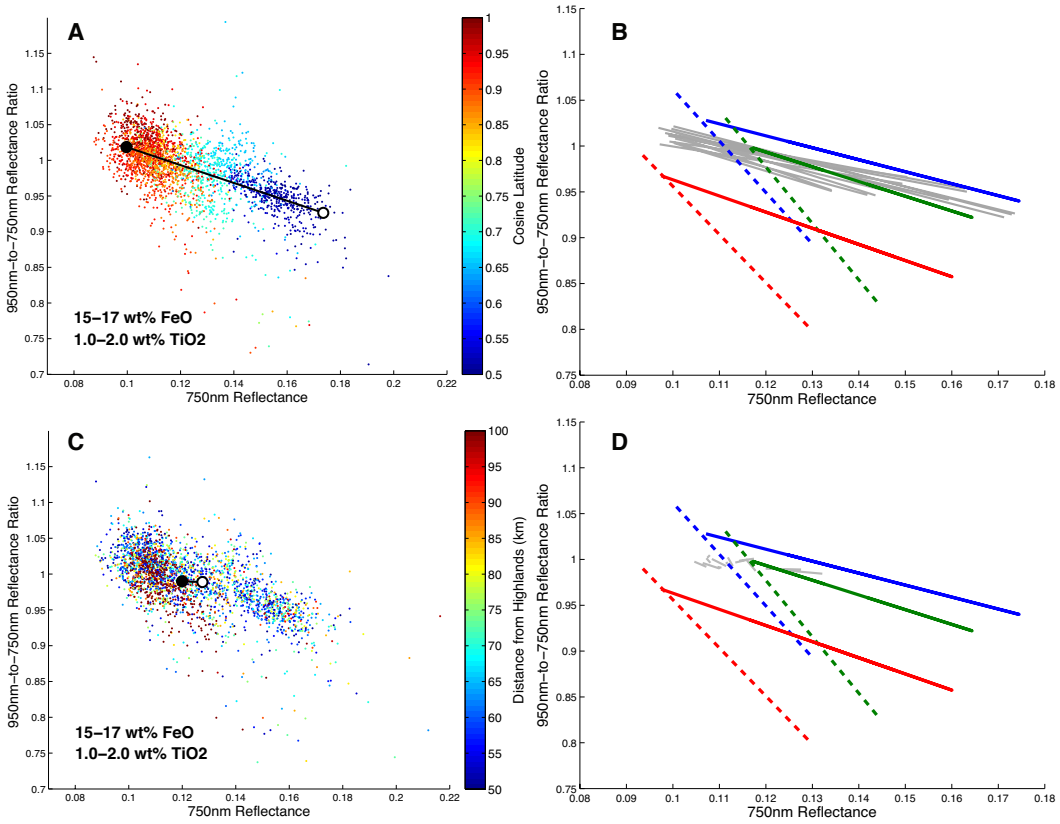

Figure 3.15: Color variation of mare surfaces that are at least 50 km from the nearest highlands (compare with Figure 3.4, which characterizes the entire lunar surface). (A) Spectral characteristics of pixels sampled from regions with between 15 and 17 wt% FeO and between 1 and 2 wt% TiO_2. Points are color-coded according to cosine latitude, as in Figure 3.4. (B) Compilation of latitudinal trends across the 13 compositional bins compared to the swirl- and impact-related trends (red, green, and blue lines). (C) Spectral characteristics of the same pixels as in (A), except that points are color-coded according to distance from the highlands: blue points correspond to locations that are 50 km from the mare/highland boundary whereas red points correspond to locations that are 100 km or more from the nearest highlands (pixels within 50 km of the nearest highlands are excluded). The black trend line represents a least squares best fit through the data points with the end points indicating the color predicted by the best-fit line at locations 50 km (white circle) and 100 km (black circle) from the mare/highland boundary. (D) Compilation of the 13 highland-distance trend lines (grey lines) compared to the swirl- and impact-related trends (red, green, and blue lines).

ties), inconsistent (slopes are highly variable, with standard deviation ±3.9), and generally weak (most of the trend lines are relatively short). For example, the average change in 750 nm reflectance between 50 km and 100 km away from the mare/highland boundary is 0.001 ± 0.004, whereas the average change in 750 nm reflectance between the equator and latitudes of ±70° is 0.05 ± 0.01 (ranges are 1σ). Although the effects of highland contamination cannot be said to make no contribution whatsoever, we conclude that they cannot be responsible for the stronger and more consistent latitudinal trends we observe (Figures 3.4, 3.10, 3.14, 3.15A and 3.15B).

Ray systems from major young impacts could also contribute to the high albedo of Mare Frigoris and other high latitude maria, however, ray systems similarly cross the low latitude mare regions and should have similar effects there. For example, rays from Copernicus, Aristarcus, and Kepler all extend across low latitude mare regions. The young crater Anaxagoras ($\sim$ 50 km in diameter) is the main contributor to contamination of Mare Frigoris but lies more than 300 km from its edge, at the closest point. Significant brightening associated with the similarly young, but larger, Copernicus crater ($\sim$ 100 km in diameter) is limited to within $\sim$ 300 km, suggesting that Anaxagoras contamination is unlikely to dominate the spectra of Mare Frigoris. Moreover, although contamination from crater ray systems may affect the spectra of certain parts of the maria, there is no reason to expect such contamination to vary systematically with latitude in such a way as to create the latitudinal trends we report here. *Werner and Medvedev* (2010) found no concentration of rayed craters at high latitudes and, due to the present impact rate inhomogeneity (*Le Feuvre and Wieczorek*, 2011), we would actually expect less contamination from young crater ejecta at high latitudes. Crater ray contam-

ination could be substantially responsible for the trends we observe only if such contamination favors high latitudes by chance. Although we cannot rule out this possibility, we regard it as unlikely, especially given the symmetry of the latitudinal trends (Figure 3.9) and the consistency of their slopes across a range of different compositions (Figure 3.10, Figure 3.14, Figure 3.15B).

Finally, even if highland contamination were to have a significant effect on the observed spectral characteristics, the effect would more likely involve an increase (rather than a decrease) in the 950 nm/750 nm reflectance ratio. As illustrated in Figure 3.6, low-iron regions, such as the highlands, tend to plot farther up and to the right compared with high-iron regions, such as the maria, meaning that spectral trends due to highland contamination should have a positive slope, unlike the negative latitudinal trend slopes we observe ($m_1 = -1.5$).

3.3.2.6 Phase Angle Biases and LOLA Reflectance

The Clementine spacecraft imaged the lunar surface over a range of phase angles (sun-surface-spacecraft angle), from typically less than 25° at the equator, to as high as $\sim 100\,^{\circ}$ at high latitudes. The Clementine mosaics are photometrically normalized and calibrated such that they provide an estimate of reflectance reduced to standard illumination conditions (*Eliason et al.*, 1999), but the imperfect calibration and imperfect knowledge of photometric behavior, leave small but systematic errors in the mosaics. In particular, the 950 nm reflectance mosaics exhibit artificially low reflectance values when based on imagery collected at relatively high phase angles (imperfections in the 750 nm reflectance mosaics are insignificant by comparison). This can be seen by comparing adjacent parts of the mosaic that are based on imagery collected

at differing phase angles (Figure 3.16). From equation (3.2), and bearing in mind that m_2 is negative, it follows that this has the effect of making relatively higher phase angle areas artificially low in β (and therefore appearing less like the bright parts and more like the dark parts of swirls). Because the high latitude Clementine data correspond to systematically higher phase angles, β therefore tends to be underestimated at high latitudes. This is the opposite of the trend we observe, indicating that the reported latitudinal effect on color must be even stronger than it appears in Figure 3.4, Figure 3.10 and Figure 3.12.

The conclusion that phase angle biases are not the source of the observed latitudinal color variation is further supported by examination of an independent dataset obtained from the Lunar Orbiter Laser Altimeter (LOLA). LOLA was recently used to measure lunar surface reflectance at 1064 nm (*Lucey et al.*, 2014). Because LOLA uses its own laser light source to illuminate the surface, reflectance estimates are obtained at a constant phase angle of nearly zero. Figure 3.9B shows LOLA 1064 nm reflectance across the lunar maria, confirming that, independent of phase angle, higher latitude maria appear to exhibit higher reflectance, as seen in the Clementine data.

3.4 Discussion

The latitudinal color variation we observe is unlike the color trends associated with impacts but statistically equivalent to those observed at swirls (Figure 3.10, Figure 3.11), suggesting a common mechanism. It has been proposed that the swirl-related color trend could be the result of magnetic and/or electric field-related alteration of the regolith microstructure (*Pieters et al.*, 2014),

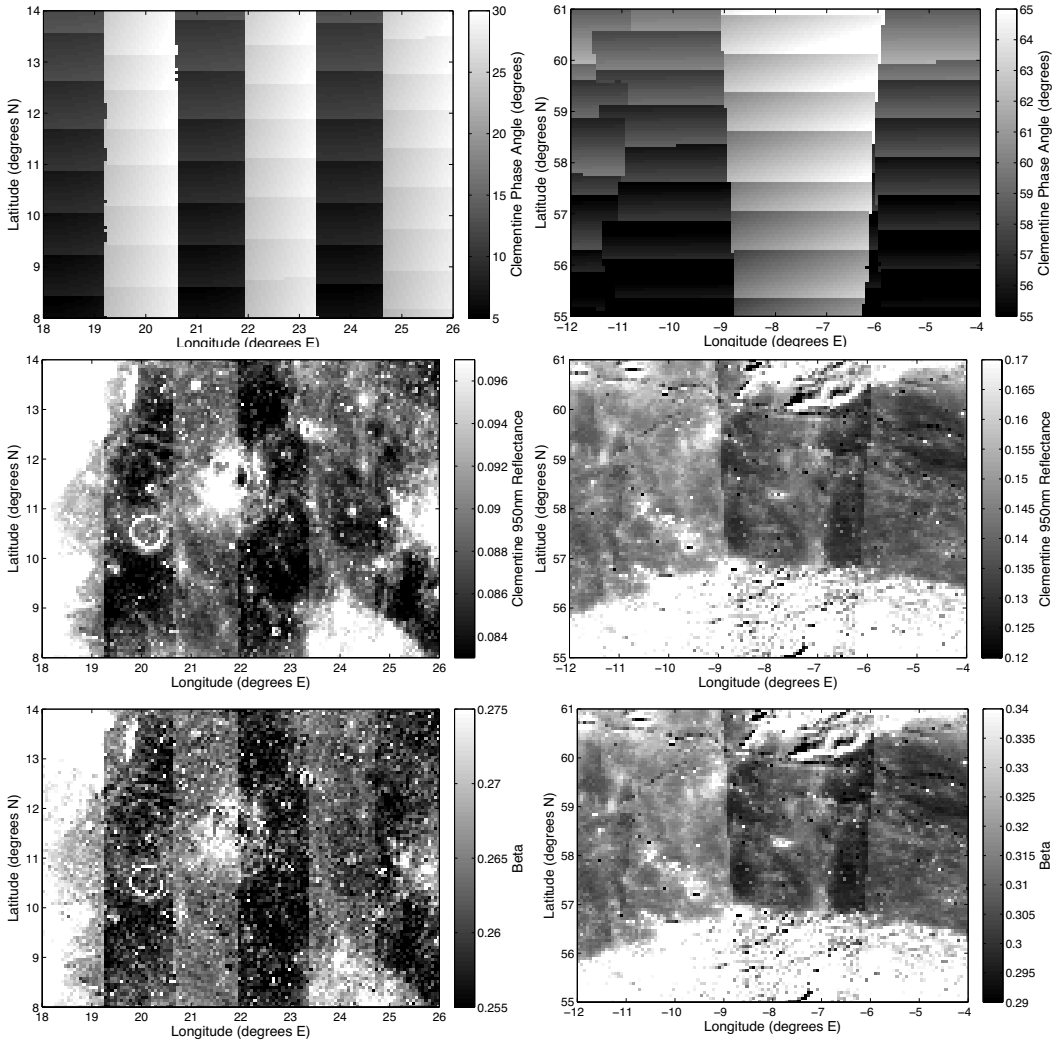

Figure 3.16: Phase angle effects on 950 nm reflectance mosaics and derived β. Left panels show a low-latitude region in Mare Tranquillitatis. Right panels show a high-latitude region in Mare Frigoris. Top panels show the phase angle corresponding to the imagery collected across the regions. The middle panels show Clementine 950 nm reflectance, illustrating a bias toward lower reflectance values for imagery collected at relatively higher phase angles. The bottom panels show the derived parameter β, illustrating that the phase angle bias means that β is underestimated for higher phase angle imagery.

electrostatic sorting of fine dust (*Garrick-Bethell et al.*, 2011), or similar mixing of compositionally distinct materials (*Blewett et al.*, 2011). However, it is not clear how such mechanisms could also produce the latitudinal color variation we report here. Instead, we propose that reduced solar wind flux is the most likely common mechanism behind the latitudinal and swirl-related color trends. Solar wind flux is reduced both with increasing latitude (due to the increasing incidence angle), and very likely at swirls, where strong magnetic fields may be partially shielding the surface from the impinging solar wind (*Hood and Schubert*, 1980; *Hood and Williams*, 1989; *Hemingway and Garrick-Bethell*, 2012). Micrometeoroid flux, in contrast, varies with latitude but should be unaffected by magnetic fields (*Richmond et al.*, 2003) and therefore cannot account for the color variations observed at swirls.

The observed latitudinal and swirl-related variations in spectral characteristics (i.e., those described by the β parameter) suggest a dependence on average flux rather than on the total accumulation of solar wind ions. A single grain saturates after only $\sim 100,000$ years (*Hapke*, 2001) such that even a surface shielded by as much as 90% would saturate after only ~ 1 million years. Consistent with this constraint, swirls often exhibit diffuse morphologies, with gradual transitions from the bright parts to darker background soils. In these regions, mean solar wind flux could vary smoothly between the bright parts of swirls and the darker background soils. Hence, if swirls are the result of locally altered solar wind weathering, their color must be controlled not by total accumulation of solar wind ions, but instead by some flux-dependent equilibrium—for instance between regolith gardening and solar-wind-induced alteration of exposed grain surfaces.

These observations lead us to propose a new model of how space weath-

ering operates for solar wind and micrometeoroids. Over length scales of a few kilometers, the surface exhibits considerable variability in α, owing to the appearance of fresh craters (low α) among the darker background soils (high α), whereas variability in β is low (Figure 3.1B, Figure 3.2B, Figure 3.3B). Our interpretation is that the equilibrium β is reached so rapidly that we do not observe variability in its value over $\sim$ kilometer scales, whereas the evolution of α occurs gradually, as impact craters transition into mature soils over longer timescales. We propose a model in which fresh impact craters begin with high albedo and low 950 nm/750 nm band ratios (the hypothetical "hyperfresh" point illustrated in Figure 3.17, which should depend only on local mineralogy), then rapidly evolve to an equilibrium value of β (controlled by solar wind flux), and finally follow the steeper progression towards larger values of α, as they gradually mature toward the local equilibrium color. Both the rapid weathering to a solar wind flux-dependent β and the gradual weathering toward the local saturation level of α involve decreases in albedo and increases in the 950 nm/750 nm band ratio. However, the initial rapid weathering process (change in β) has a proportionally greater effect (by a factor of ~ 3.6) on albedo (Figure 3.17). In this model, the trends are parallel, as the soil matures toward distinct solar wind flux-dependent equilibrium colors, rather than converging to a common point, contrary to expectations for a simple mixing process (see also (*Staid and Pieters*, 2000; *Wilcox et al.*, 2005)).

The differences in optical effects may reflect differences in the way solar wind and micrometeoroid bombardment affect lunar soils. For example, the darkening may be due primarily to the accumulation of nanophase reduced iron (*Hapke*, 2001; *Noble et al.*, 2007) generated both by solar wind and micrometeorites, whereas the increased 950 nm/750 nm band ratio, which

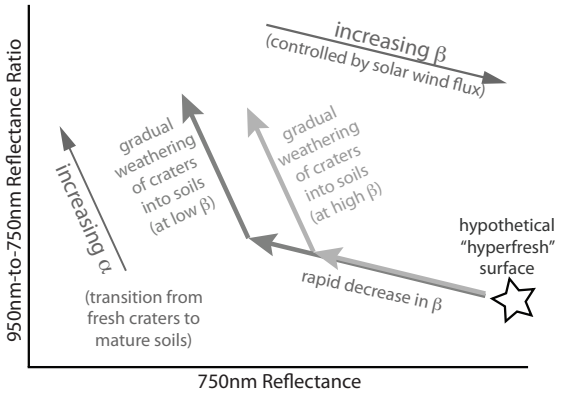

Figure 3.17: Inferred optical evolution process. For a given composition, all impact craters large enough to excavate fresh material should begin with the same characteristic color (the hypothetical "hyperfresh" point at right). In this model, following the impact event, the freshly exposed material experiences rapid weathering until it reaches an equilibrium value of β, controlled by solar wind flux. This rapid color change occurs primarily in albedo, but is accompanied by a small change in the 950 nm/750 nm band ratio. Subsequently, the crater material matures gradually (increases in α) until it reaches the local saturation maturity level of the surrounding, well-developed soils. This gradual maturation involves additional darkening, but is also accompanied by a proportionally greater band ratio increase than during the initial mode of rapid weathering.

reflects both suppression of spectral features and increased continuum slope, may also be influenced by impact vitrification (*Adams and McCord*, 1971) and the soil's impact-induced disintegration into increasingly finer grains (*Pieters et al.*, 1993), neither of which depend on solar wind.

In spite of the uncertainties regarding the precise mechanism for the observed latitudinal trends, our results help to quantify the effects of latitude-dependent space weathering, which may need to be accounted for when interpreting spectral measurements at different latitudes (*Zuber et al.*, 2012; *Cohen et al.*, 2014). The production and retention of hydroxyl (OH) groups, for instance, reportedly varies with latitude (*Clark*, 2009; *Pieters et al.*, 2009; *Sunshine et al.*, 2009; *McCord et al.*, 2011; *Hendrix et al.*, 2012) as well as at swirls (*Kramer et al.*, 2011). The latitudinal variation in space weathering effects we report here may influence the interpretation of the spectral observations behind such findings.

Our results also suggest that it may be possible to use variations in surface color to quantify the reduction in solar wind flux at swirls. For example, the magnitude of color variation at the Reiner Gamma swirl is approximately equivalent to the color variation observed between the equator and 60° latitude, suggesting that this magnitude of color variation corresponds to a $\sim$ 50% reduction in solar wind flux. This type of analysis, in conjunction with other methods, may in turn help in estimating the strength of surface fields at swirls and in making predictions that can eventually be tested with near surface magnetic field and solar wind flux measurements.

3.5 Conclusions

Our analysis reveals a systematic latitudinal variation in the near-infrared spectral properties of the lunar surface, and in particular, across the maria. Specifically, low latitude mare regions tend to be darker and have higher 950 nm/750 nm reflectance ratios than high latitude mare regions, such as the noticeably bright Mare Frigoris. This latitudinal trend persists across a range of distinct compositions, confirming that it is not an artifact of the fact that regions with the highest iron and titanium content happen to be concentrated at low latitudes. Our analysis also shows that the trends are not significantly affected by contamination from the highlands, nor can they be artifacts of phase angle biases, as confirmed by our comparison with the constant phase angle LOLA reflectance data. Furthermore, the spectral characteristics of the latitudinal color trend are statistically equivalent to those observed at lunar swirls; higher latitude regions appear more like the bright parts of swirls. We propose that reduced solar wind flux, which should occur both at swirls and toward higher latitudes, is the common mechanism behind the observed color variations. We suggest a process by which freshly exposed materials initially experience rapid changes in color until reaching a solar wind flux-dependent equilibrium, followed by a more gradual period of optical maturation driven mainly by micrometeoroid impacts. If correct, this model could help quantify the distinct effects of solar wind versus micrometeoroid weathering and may be important for the interpretation of spectral observations made at different latitudes on the Moon and other airless bodies throughout the solar system.

Acknowledgements

This work was supported by the BK21 plus program through the National Research Foundation (NRF), funded by the Ministry of Education of Korea. Partial support was provided by the UCSC/NASA Ames University Affiliated Research Center, Aligned Research Program; the Alfred P. Sloan Foundation; and NASA grant NNX13AJ51G. We thank Carle Pieters for important discussions and advice, Paul Lucey for supplying the LOLA reflectance data, and the two reviewers for their helpful comments and suggestions.

Chapter 4

A Rigid and Weathered Ice Shell on Titan

This chapter is adapted from Hemingway, D., F. Nimmo, H. Zebker, and L. Iess (2013), A rigid and weathered ice shell on Titan, *Nature, 500*(7464), 550–552, doi:10.1038/nature12400.

Abstract

Several lines of evidence suggest that Saturn's largest moon, Titan, has a global subsurface ocean beneath an outer ice shell 50 to 200 kilometers thick (*Béghin et al.*, 2010; *Bills and Nimmo*, 2011; *Iess et al.*, 2012; *Tobie et al.*, 2006). If convection is occurring (*Mitri and Showman*, 2008; *Tobie et al.*, 2005), the rigid portion of the shell is expected to be thin; similarly, a weak, isostatically-compensated shell has been proposed to explain the observed topography (*Choukroun and Sotin*, 2012; *Nimmo and Bills*, 2010). Here we report a strong inverse correlation between gravity (*Iess et al.*, 2012) and to-

pography (*Zebker et al.*, 2012) at long wavelengths that are not dominated by tides and rotation. We argue that negative gravity anomalies (mass deficits) produced by crustal thickening at the base of the ice shell overwhelm positive gravity anomalies (mass excesses) produced by the small surface topography, giving rise to this inverse correlation. We show that this situation requires a substantially rigid ice shell with an elastic thickness exceeding 40 kilometers, and hundreds of meters of surface erosion and deposition, consistent with recent estimates from local features (*Moore et al.*, 2013; *Neish et al.*, 2013). Our results are therefore not compatible with a geologically active, low-rigidity ice shell. After extrapolating to wavelengths that are controlled by tides and rotation, we suggest that Titan's moment of inertia may be even higher (that is, Titan may be even less centrally-condensed) than is currently thought (*Iess et al.*, 2010).

4.1 Introduction

Combined studies of gravity and topography can yield useful information about the near-surface interior structure of solid planetary bodies (*Wieczorek*, 2007). In particular, the ratio between the gravity and topography at a particular wavelength, known as the spectral admittance, is generally a function of the thickness of the lithosphere and the degree to which the topography is compensated by subsurface density anomalies. For example, small admittances arise when topography is compensated isostatically such that the additional gravity associated with surface topography is offset by the reduced gravity associated with the corresponding low-density isostatic roots. Conversely, large admittances usually indicate incomplete isostatic compensation. Large admittances

are typical at short wavelengths, for which elastic flexure of the lithosphere is an effective means of supporting the topography. The wavelength at which the primary support mechanism transitions from flexural to isostatic is generally a function of the effective elastic layer thickness, which, in turn, tells us about the thermal structure of the lithosphere.

In the case of Titan, our limited knowledge of the gravity field restricts our analysis to the longest of wavelengths (mainly degrees 2 and 3). The degree-2 gravity field is well determined, but is dominated by the effects of tidal and rotational distortion. The gravitational effects of isostatically supported topography at degree 2 are small by comparison and, in any case, difficult to distinguish from the tidal and rotational effects. In this analysis, we will therefore focus on the degree-3 gravity and topography. The degree-3 signal is useful because, although it is small compared to those at degrees 2 and 4, it is not directly affected by tides, rotation, or tidal heating (*Nimmo and Bills*, 2010). Though our analysis will focus primarily on degree 3, we will also discuss the implications of extrapolating our results to degree 2.

Titan is thought to consist of a large, rocky inner core, surrounded by layers of H_2O in various phases, and covered by a dense nitrogen atmosphere. The outer-most layer of the H_2O mantle is thought to consist primarily of ice-I and estimates for its thickness range from 50 to 200 km (*Béghin et al.*, 2010; *Bills and Nimmo*, 2011; *Iess et al.*, 2012; *Tobie et al.*, 2006). The surface is geomorphologically varied, with seas of liquid hydrocarbons, dendritic river networks, and large fields of sand dunes. Several surface features have been described as icy volcanoes, suggesting ongoing geologic activity in the ice shell. However, evidence for such "cryovolcanism" is not entirely conclusive and there is considerable disagreement about the present level of geologic activity on

Titan. Obtaining constraints on the loading history and elastic thickness of the ice shell will help in understanding the evolution of Titan's surface and the likely level of ongoing geologic activity (*Moore and Pappalardo*, 2011).

Section 4.2 describes the observed gravity and topography, as well as the implied admittance. In section 4.3, we describe our model and use it to interpret the observed admittance, leading to estimates for the ice shell's elastic thickness and the magnitude of surface erosion that has taken place. In section 4.4, we discuss the implications of our results before concluding in section 4.5.

4.2 Observations

4.2.1 Gravity Field

The description of Titan's gravitational field is given by *Iess et al.* (2012) as non-normalized, dimensionless potential coefficients C^g_{lm}, S^g_{lm} such that the gravitational potential at the reference radius (R) can be written

$$U(\theta,\phi) = -\frac{GM}{R}\sum_{l=0}^{\infty}\sum_{m=0}^{l}\left(C^g_{lm}\cos m\phi + S^g_{lm}\sin m\phi\right)P_{lm}(\cos\theta)$$

where $P_{lm}(\cos\theta)$ are the non-normalized associated Legendre functions, θ is colatitude, ϕ is longitude and C^g_{lm} and S^g_{lm} are non-normalized spherical harmonic coefficients of degree l and order m. In terms of the non-normalized coefficients, the radial component of the gravitational acceleration at the ref-

erence radius (R) can be written

$$g_r(\theta,\phi) = \frac{GM}{R^2}\sum_{l=0}^{\infty}\sum_{m=0}^{l}(l+1)\left(C^g_{lm}\cos m\phi + S^g_{lm}\sin m\phi\right)P_{lm}(\cos\theta)$$

In our admittance analysis (section 4.2.3), we will use fully normalized, dimensionalized gravitational acceleration coefficients, $\bar{C}^g_{lm}$, $\bar{S}^g_{lm}$, such that

$$g_r(\theta,\phi) = \sum_{l=0}^{\infty}\sum_{m=0}^{l}\left(\bar{C}^g_{lm}\cos m\phi + \bar{S}^g_{lm}\sin m\phi\right)\bar{P}_{lm}(\cos\theta)$$

where $\bar{P}_{lm}(\cos\theta)$ are the fully normalized associated Legendre functions (see Appendix A). The fully normalized and dimensionalized gravity coefficients, $\bar{C}^g_{lm}$, $\bar{S}^g_{lm}$, are related to the non-normalized, dimensionless potential coefficients C^g_{lm}, S^g_{lm} by

$$\left\{\bar{C},\bar{S}\right\}^g_{lm} = \left((2-\delta_{0m})(2l+1)\frac{(l-m)!}{(l+m)!}\right)^{-\frac{1}{2}}(l+1)\frac{GM}{R^2}\left\{C,S\right\}^g_{lm} \qquad (4.1)$$

where the square root term does the normalization, the $(l+1)$ term arises from the differentiation associated with converting from potential to gravity, the $\frac{GM}{R^2}$ term generates dimensional coefficients (which we will express in terms of mGal $= 10^{-5}\,\mathrm{ms}^{-2}$), and where δ_{0m} is the Kronecker delta.

Three solutions for Titan's low-order gravity field have been obtained via radio tracking of the *Cassini* spacecraft (*Iess et al.*, 2010, 2012), with the results being well constrained up to spherical harmonic degree 3. In the first two (SOL1a and SOL1b), results from six *Cassini* gravity flybys were analyzed separately and then combined into multi-arc solutions. Whereas SOL1a attempts to model the gravity field only up to degree 3, SOL1b attempts to

model the field up to degree 4, but only as a means of verifying the robustness of the degree-3 solution. It is found that the degree-3 solution differs only modestly between SOL1a and SOL1b. For the last solution (SOL2), a global model extending to $l = 3$ was derived using *Pioneer* and *Voyager* data and satellite ephemerides in addition to *Cassini* observations. In spite of the different approaches, the SOL2 field closely resembles the SOL1a field. The SOL1b solution matches less closely, likely because it also attempts to include the degree-4 component of the field. Although all three solutions give a consistent estimate of the periodic (tidal) k_2 Love number (with a central value of 0.6), the static part of the degree-4 field is currently not well constrained due to the limited nature of the observations. Our calculations will be based primarily on the SOL1a gravity field.

4.2.2 Topography

Titan's topography is likewise described by *Zebker et al.* (2012) in terms of non-normalized spherical harmonic coefficients C^h_{lm}, S^h_{lm} and can be written as

$$H(\theta, \phi) = \sum_{l=0}^{\infty} \sum_{m=0}^{l} \left(C^h_{lm} \cos m\phi + S^h_{lm} \sin m\phi \right) P_{lm}(\cos \theta)$$

where, again, $P_{lm}(\cos \theta)$ are the non-normalized associated Legendre functions, θ is colatitude, ϕ is longitude and C^h_{lm} and S^h_{lm} are non-normalized spherical harmonic coefficients of degree l and order m. To convert from non-normalized coefficients to fully normalized coefficients, $\bar{C}^h_{lm}$, $\bar{S}^h_{lm}$, we write

$$\left\{ \bar{C}, \bar{S} \right\}^{\,h}_{lm} = \left((2 - \delta_{0m})(2l + 1) \frac{(l - m)!}{(l + m)!} \right)^{-\frac{1}{2}} \{C, S\}^h_{lm} \tag{4.2}$$

and the topography is described (in meters) by

$$H(\theta,\phi) = \sum_{l=0}^{\infty} \sum_{m=0}^{l} \left(\bar{C}^h_{lm} \cos m\phi + \bar{S}^h_{lm} \sin m\phi \right) \bar{P}_{lm}(\cos\theta)$$

where $\bar{P}_{lm}(\cos\theta)$ are the fully normalized associated Legendre functions (see Appendix A).

The topography models are derived from a combination of radar altimetry and analysis of the overlapping regions of radar images, in a technique known as SARtopo (*Zebker et al.*, 2009; *Stiles et al.*, 2009; *Zebker et al.*, 2012), and were used to derive shape solutions up to $l = m = 11$. Several distinct solutions were produced, depending on where the harmonic expansion was truncated. We denote these solutions Deg4-exp, Deg5-exp, ... Deg11-exp, where the number indicates the highest degree and order used to fit the observations.

Due to the large gaps in *Cassini* radar coverage (Figure 4.1), topography models with power beyond degree 6 are not adequately constrained unless an *a priori* restriction is applied (e.g., minimize rms deviation from best-fit sphere). Even when *a priori* constraints are applied, the coefficients tend to be less stable when the model's expansion limit exceeds degree 6 (Figure 4.2).

For our purposes, we prefer to use the highest resolution data available without requiring *a priori* constraints in the model fits. We therefore primarily use the Deg6-exp model (*Zebker et al.*, 2012) in our analysis, the coefficients for which are given in Table 4.1.

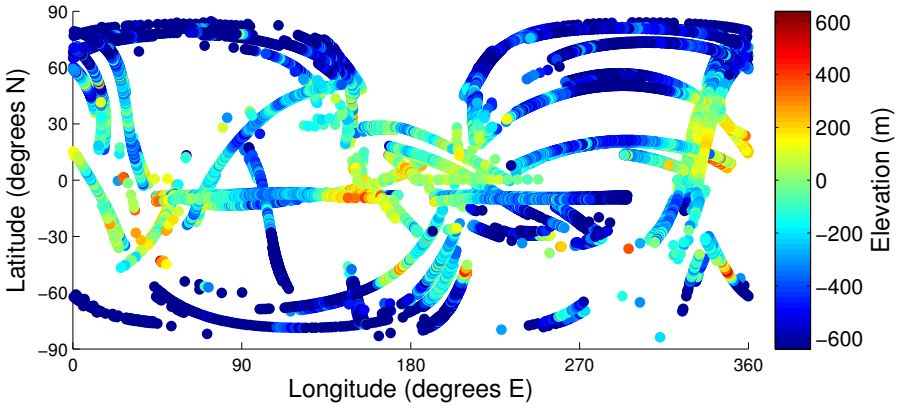

Figure 4.1: *Cassini* radar-derived elevation data for Titan. Elevation is given relative to the 2575-km reference sphere.

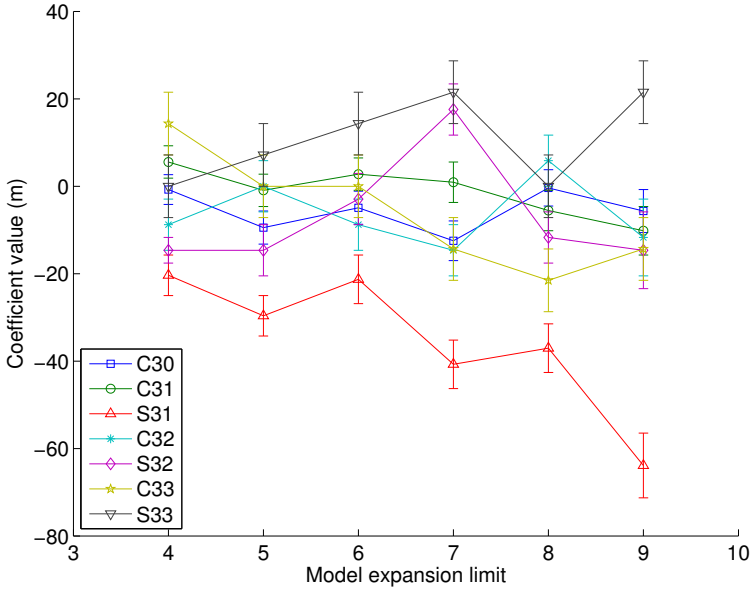

Figure 4.2: Degree-3 normalized topography model (*Zebker et al.*, 2012) coefficients (with 1-σ error bars) as a function of the maximum spherical harmonic degree allowed when fitting the data.

Table 4.1: Fully normalized Deg6-exp topography model (*Zebker et al.*, 2012) coefficients (in meters).

Term	Estimate	1σ error
C00	2574750.0	6.0
C10	0.0	5.8
C11	23.1	5.2
S11	18.5	5.8
C20	-169.5	4.5
C21	-17.8	5.4
S21	31.8	7.0
C22	120.8	4.6
S22	20.1	4.6
C30	-4.9	3.8
C31	2.8	3.7
S31	-21.3	5.6
C32	-8.8	5.9
S32	-2.9	5.9
C33	0.0	7.2
S33	14.3	7.2
C40	-39.3	3.7
C41	22.1	3.2
S41	75.9	4.2
C42	4.5	4.5
S42	-26.8	4.5
C43	16.7	0.0
S43	-50.2	0.0
C44	0.0	0.0
S44	-47.3	0.0

Term	Estimate	1σ error
C50	28.6	3.3
C51	-26.9	2.3
S51	-14.0	4.7
C52	37.1	6.2
S52	-12.4	6.2
C53	0.0	0.0
S53	0.0	0.0
C54	0.0	0.0
S54	0.0	0.0
C55	0.0	0.0
S55	0.0	0.0
C60	-2.5	3.1
C61	8.9	2.5
S61	-61.0	3.8
C62	-24.1	0.0
S62	0.0	0.0
C63	0.0	0.0
S63	0.0	0.0
C64	0.0	0.0
S64	0.0	0.0
C65	0.0	0.0
S65	0.0	0.0
C66	0.0	0.0
S66	0.0	0.0

4.2.3 Observed Admittance

When we compare the degree-3 gravity and topography signals, a striking negative correlation is apparent (Figure 4.3). We quantify this relationship by employing an admittance analysis (*McKenzie*, 1994; *Wieczorek*, 2007), which measures the gravity-to-topography ratio in a way that is not biased by uncorrelated signals in the gravity data. The degree-l admittance, $Z\,(l)$, is given by

$$Z(l) = \frac{D_{hg}(l)}{D_{hh}(l)} \tag{4.3}$$

where $D_{ij}(l)$ represents the cross-power spectrum between fields i and j and is given by

$$D_{ij}(l) = \sum_{m=0}^{l} \left(C_{lm}^{i} C_{lm}^{j} + S_{lm}^{i} S_{lm}^{j} \right) \tag{4.4}$$

The correlation between the two signals is given by

$$\gamma(l) = \frac{D_{hg}(l)}{\sqrt{D_{hh}(l) D_{gg}(l)}} \tag{4.5}$$

If some fraction of the gravity signal is not correlated with the surface topography, then the coherence (γ^2) will be less than one. However, the crucial advantage of equation (4.3) is that any such gravity noise does not affect the estimated admittance, Z. For the case of Titan, contributions to gravity from deeper interfaces (such as the silicate interior) are likely to be important, while contributions to the surface topography from these processes are likely negligible. An approach like that embodied in equation (4.3), which is unaffected by noisy gravity, is essential for interpreting the limited observations available at Titan.

For each of the three gravity models, we computed admittances based on

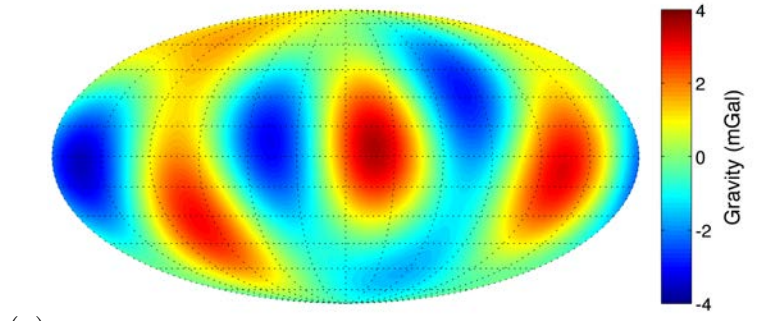

(a)

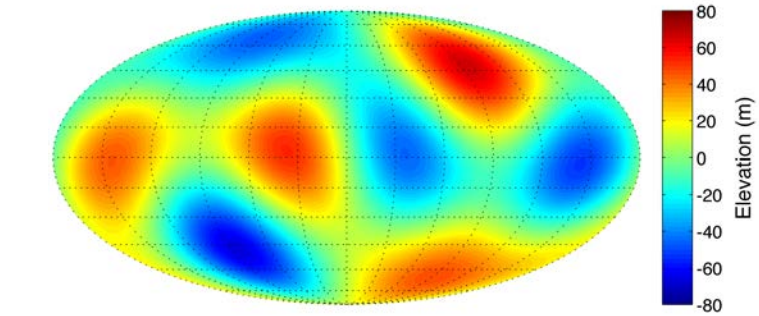

(b)

Figure 4.3: Titan's degree-3 gravity and topography. (a) Gravity field derived from the potential coefficients of the SOL1a gravity field representation of *Iess et al.* (2012) (multi-arc analysis, 3×3 gravity field). (b) Spherically referenced topography based on degree-6 harmonic expansion (*Zebker et al.*, 2012). The two signals display a strong negative correlation (with correlation coefficient $\gamma = -0.61$) and give rise to an admittance of -32 mGal/km, based on a Monte Carlo analysis accounting for the uncertainty in the two signals. Maps are shown in Mollweide projection, centered on the anti-Saturnian point (180° longitude).

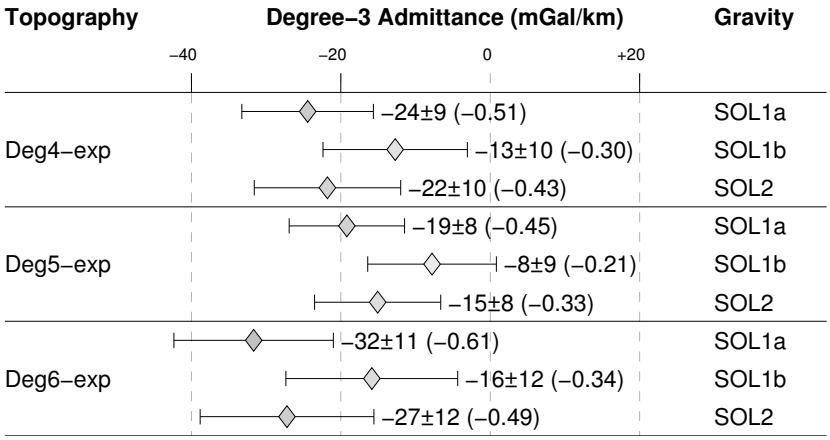

Figure 4.4: Admittance estimates for nine sets of gravity and topography data. Three distinct gravity models (*Iess et al.*, 2012) and three distinct topography models (*Zebker et al.*, 2012) (truncated at harmonic degrees 4, 5 and 6) were used to produce a total of nine separate admittance estimates. Each estimate is based on a Monte Carlo analysis in which the admittance was computed for each of 100,000 distinct sets of gravity and topography coefficients, distributed according to the 1σ uncertainties in the model coefficients. For each Monte Carlo analysis, diamonds are plotted at the mean admittance estimate, and 1σ error bars are shown to represent the distribution. To the right of the error bars are the mean $\pm$ standard deviation of the admittance estimates in milligals per kilometer (mGal/km), followed by the correlation coefficients (γ) in parentheses.

three separate topography models (Figure 4.4). The admittance and correlation estimates in Figure 4.4 were obtained through a Monte Carlo analysis. For each gravity/topography combination, the results were obtained from a distribution of 100,000 distinct admittance and correlation estimates, each of which was based on gravity and topography coefficients that were generated randomly and distributed according to the 1-σ uncertainties in the model coefficients. Individual correlations and admittance estimates were computed according to equations (4.3) and (4.5). In spite of the variability between the estimates, the degree-3 admittance appears to be substantially negative, and the Monte Carlo analysis shows that this result is robust to the model uncertainties (Figure 4.4).

The admittance estimated based on the Monte Carlo analysis will have a slightly smaller magnitude than the admittance estimated directly from the coefficients (i.e., when uncertainties are ignored). This is because, as long as there is uncertainty in the topography coefficients, the mean of the distribution of D_{hh} (see equation 4.4) will always be greater than the value of D_{hh} obtained directly from the estimated topography coefficients (because if x is normally distributed, then $E(x^2) > [E(x)]^2$). For example, if uncertainties are ignored, the admittance computed directly from the SOL1a gravity (*Iess et al.*, 2012) coefficients and the Deg6-exp topography (*Zebker et al.*, 2012) coefficients is -39 mGal/km, whereas when uncertainties are accounted for using a Monte Carlo analysis, the mean estimated admittance is -32 mGal/km. We adopt the latter value because it is more conservative—more negative admittances would require higher magnitudes of erosion and/or larger elastic thicknesses (see section 4.3.2).

4.3 Model and Results

The negative correlation we observe between the gravity and topography signals (section 4.2.3) is surprising—negative admittances are rare. They can occur in convecting systems with strong viscosity stratification (*Richards and Hager*, 1984), but it is unclear why Titan's ice shell would have such layering, and the shell is sufficiently thin that—as for Enceladus (*Roberts and Nimmo*, 2008)—convective features should have much shorter horizontal length scales than degree 3. Below we construct a model that allows for negative admittances under certain conditions.

4.3.1 Admittance and Flexure Model

Here, we will assume that the topography is supported by some combination of shell thickness variations (Airy isostasy, e.g., *Nimmo and Bills* (2010)) and elastic flexure. An admittance model requires that we describe how the gravity (g) is affected by topography (h).

Gravity Anomalies

The gravity anomaly at degree l due to a thin surface layer of amplitude h_l and density ρ_c is given by (*Jeffreys*, 1976)

$$\Delta g_l^t = \frac{(l+1)}{(2l+1)} 4\pi G h_l \rho_c \tag{4.6}$$

and similarly, the gravity anomaly due to a thin layer (a "root") of thickness r_l and density contrast $\Delta\rho = \rho_m - \rho_c$ at the base of the shell, is given by

$$\Delta g_l^b = -\frac{(l+1)}{(2l+1)} 4\pi G r_l \Delta\rho \left(1 - \frac{d}{R}\right)^{l+2} \tag{4.7}$$

where the mean thickness of the shell is d, the radius of the body is R, and ρ_m is the density of the material underlying the shell (i.e., the subsurface ocean). In the short-wavelength limit ($l \gg 1$), equation (4.6) reduces to the usual flat-plate formula, as required.

When the net gravity anomaly and the surface topography (h_l) are known, the theoretical admittance is given by

$$Z_l = \frac{\Delta g_l^t + \Delta g_l^b}{h_l} \tag{4.8}$$

In the remainder of this development, we drop the subscripts from both h and r and take it as understood that these parameters correspond to a specific wavelength.

In practice, it will be difficult to observe r and therefore to compute Δg_l^b according to equation (4.7). Instead, we would like to find an expression for r in terms of h, which can be more readily observed. This is generally possible because, for a finite elastic thickness, there will be a balance between the overburden pressure of positive surface topography ($\rho_c g h$), the buoyancy of the root ($\Delta\rho g r$), and the restoring forces due to flexure.

Lithospheric Deflection, Cartesian case

If the deflection of the initial ice shell is w, in a Cartesian system, and if geoid undulations are neglected for the moment, this pressure balance can be written as

$$D\nabla^4 w = \Delta\rho g r - \rho_c g h \tag{4.9}$$

Here, D represents flexural rigidity and is given by

$$D = \frac{ET^3}{12(1-\nu^2)} \tag{4.10}$$

where T is the effective elastic thickness, E is Young's modulus and ν is Poisson's ratio. We treat w as positive upward bending, h as positive upward relief above the reference ice shell surface, and r as positive downward relief from the base of the ice shell. The relationship between r and h depends on the elastic properties of the shell and the thickness of loads applied at the top (d_t) and bottom (d_b) of the shell (Figure 4.5); d_t is the thickness of material added at the surface (a negative value would indicate erosion), and d_b is the thickness of material added at the base of the ice shell (a positive value would indicate basal freezing, a negative value, basal melting). Our model represents the equilibrium state achieved after the lithosphere has finished deflecting in response to the applied load(s). The model also assumes that the ice shell properties do not change over time.

Our formulation is similar to those of *Turcotte et al.* (1981) and *McGovern et al.* (2002), however, our sign convention differs slightly and, for simplicity, we assume that material added at the top or bottom of the shell is also of density ρ_c. Our formulation also differs in that we handle top and bottom loads

simultaneously with w being the total deflection resulting from the combined effects of top and bottom loading.

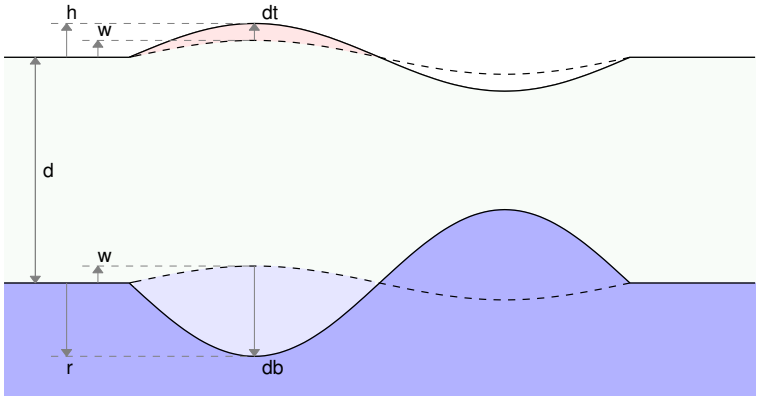

Figure 4.5: Illustration of the influence of top loading (pale pink material, d_t) and bottom loading (pale blue material, d_b) on ice shell flexure (w), surface relief (h) and root thickness (r).

From Figure 4.5, we have

$$h = w + d_t \tag{4.11}$$

$$r = d_b - w \tag{4.12}$$

Then, assuming the loads are periodic and in-phase, we can solve (4.9) for w, obtaining

$$w = \frac{\Delta\rho d_b - \rho_c d_t}{\rho_m + \mu} \tag{4.13}$$

Here, we have introduced a parameter, μ, which has units of density and will serve as a shorthand for the flexural rigidity at a particular wavelength and gravity. In a Cartesian system,

$$\mu(k) = \frac{ET^3k^4}{12(1-\nu^2)g} \tag{4.14}$$

where k is a wavenumber. The advantage of using this shorthand will become clear when we move from a Cartesian to a spherical system.

It is useful to define a compensation function, $C(\rho)$, that expresses the degree of compensation under flexural support compared with the case of pure isostasy. This can be defined as the ratio of the deflection, w, according to (4.13) to the zero-rigidity deflection, w_0, obtained from (4.13) when $\mu = 0$. That is, $C = w/w_0$, or

$$C(\rho) = \frac{1}{1 + \frac{\mu}{\rho}} \tag{4.15}$$

When the elastic thickness, T, is zero, $C = 1$ (fully compensated). The parameter ρ is the density contrast that is resisting the flexure (i.e., related to buoyancy, overburden pressure, or both). In the isostatic limit, $\Delta\rho r = \rho_c h$, whereas in the top loading case, $\Delta\rho r = \rho_c h C(\Delta\rho)$, while in the bottom loading case, $C(\rho_c)\Delta\rho r = \rho_c h$, as we will see. The theoretical value of $C = 0$ corresponds to the zero compensation case which occurs when the ice shell is infinitely rigid (i.e., as $\mu \to \infty$). In this case, deflection (w) becomes zero (equation 4.13) and so, from (4.11) and (4.12), $h = d_t$ and $r = d_b$. In this scenario, h and r are independent of one another and so both d_t and d_b must be specified in order to predict admittance. However, as long as $C > 0$, there will be some finite deflection and it will be possible to obtain r as a function of h.

If $C > 0$ and both h and d_t are specified, then from (4.11), (4.12), (4.13) and (4.15), it can be shown that

$$r = \frac{\rho_c h}{\Delta\rho}\left[\frac{1 - \frac{d_t}{h}}{C(\rho_c)} + \frac{d_t}{h}\right] \tag{4.16}$$

We have factored out $\rho_c h/\Delta\rho$ in order to facilitate direct comparison with the isostatic case and because it will be convenient to do so when calculating admittance using (4.6), (4.7) and (4.8). In the case where no material has been added to the surface (i.e., $d_t = 0$, so that loading is purely from the bottom), this expression reduces to

$$C(\rho_c)\Delta\rho r = \rho_c h \tag{4.17}$$

Similarly, if $C > 0$ and only h and d_b are specified, it can be shown that

$$r = \frac{\rho_c h}{\Delta\rho}\left[\frac{\frac{d_b}{h}}{C(\rho_c)} - \frac{d_b}{h} + 1\right] C(\Delta\rho) \tag{4.18}$$

In the case where no material has been added to the base (i.e., $d_b = 0$, so that loading is purely from the top), this expression reduces to

$$\Delta\rho r = \rho_c h C(\Delta\rho) \tag{4.19}$$

Lithospheric Deflection, spherical case

The foregoing gives correct values for r in the Cartesian case, which is an appropriate approximation for short wavelength loads. However, in order to interpret admittance at very long wavelengths, we must consider the spherical case. Assuming the icy crust behaves as a thin elastic shell of radius R, equation (4.9) becomes

$$\begin{aligned} &D\nabla^6 w + 4D\nabla^4 w + ETR^2\nabla^2 w + 2ETR^2 w \\ &= R^4\left(\nabla^2 + 1 - \nu\right)\left(\Delta\rho g r - \rho_c g h + \rho_m g h_g\right) \end{aligned} \tag{4.20}$$

where D is as in (4.10). Here, we have adopted a modified version of the approaches of *Turcotte et al.* (1981) and *McGovern et al.* (2002), which themselves follow the earlier derivation of *Kraus* (1967). The final term in (4.20) accounts for the elevation or depression of the geoid (h_g, which we treat as positive upward) that occurs with loading of the ice shell. Here, we adopt an approximation in order to obtain h_g, namely, we assume that $\left(1-\frac{d}{R}\right)^{l+2} \approx 1$, and that the geoid and gravitational acceleration do not change with depth in the shell (as has been pointed out by *Belleguic et al.* (2005), this was an implicit assumption of *Turcotte et al.* (1981)).

Having obtained h_g, and using (4.11) and (4.12), we rewrite (4.20) as

$$\left[\left(1-\frac{3\rho_m}{(2l+1)\overline{\rho}}\right)^{-1}\frac{ET}{R^2 g}\left(\frac{\frac{T^2\left(\nabla^6+4\nabla^4\right)}{R^2 12(1-\nu^2)}+\nabla^2+2}{\nabla^2+1-\nu}\right)+\rho_m\right] w = \Delta\rho d_b - \rho_c d_t$$

where $\overline{\rho}$ is the mean density of the body. If w is expressed in spherical harmonics, we can replace ∇^2 with $-l(l+1)$ (e.g., *Turcotte et al.* (1981), equations 17 and 18) and solve for w, recovering equation (4.13),

$$w = \frac{\Delta\rho d_b - \rho_c d_t}{\rho_m + \mu}$$

but with the flexural rigidity parameter now being

$$\mu(l) = \left(1-\frac{3\rho_m}{(2l+1)\overline{\rho}}\right)^{-1}\frac{ET}{R^2 g}\left(\frac{\frac{T^2\left[l^3(l+1)^3-4l^2(l+1)^2\right]}{R^2 12(1-\nu^2)}+l(l+1)-2}{l\,(l+1)-(1-\nu)}\right) \quad (4.21)$$

For a spherical system, it is also necessary to account for the ratio of surface areas at the top and bottom of the shell (since the buoyancy of the root depends on its volume, not its thickness). This effect complicates the

derivations but it can be shown that, if d_t and h are specified, then the surface area correction leads to

$$r = \frac{\rho_c h}{\Delta\rho}\left[\frac{1-\frac{d_t}{h}}{C(\rho_c)} + \frac{d_t}{h}\right]\left(1-\frac{d}{R}\right)^{-2} \tag{4.22}$$

If d_b is specified rather than d_t, we obtain

$$r = \frac{\rho_c h}{\Delta\rho}\left[\frac{\frac{d_b}{h}}{C(\rho_c)} - \frac{d_b}{h} + 1\right] C\left(\Delta\rho\left(1-\frac{d}{R}\right)^2\right)\left(1-\frac{d}{R}\right)^{-2} \tag{4.23}$$

As required, both of these expressions reduce to the Cartesian equivalents as $R \to \infty$. This correction also partially relaxes the simplifying assumption we made to obtain the geoid height so that we now assume $\left(1-\frac{d}{R}\right)^l \approx 1$ rather than $\left(1-\frac{d}{R}\right)^{l+2} \approx 1$.

Having obtained an expression for r as a function of h (which is possible as long as $C > 0$), we can now substitute (4.22) into (4.7) and combine with (4.6) and (4.8) to get an expression for admittance that depends on h and d_t, but not r

$$Z(l) = \frac{(l+1)}{(2l+1)} 4\pi G\rho_c \left[1 - \left(\frac{1-\frac{d_t}{h}}{C(\rho_c)} + \frac{d_t}{h}\right)\left(1-\frac{d}{R}\right)^l\right] \tag{4.24}$$

Equation (4.24) implicitly accounts for the root thickness (r), bottom load thickness (d_b), and mantle density (ρ_m), such that these terms do not appear in the final expression. Model admittance is sensitive to mantle density only insofar as the ratio $\rho_m/\overline{\rho}$ influences the geoid, the effect of which is captured in $C(\rho_c)$ via (4.21) and (4.15).

If d_b is specified rather than d_t, we instead substitute (4.23) into (4.7) and

obtain

$$Z(l) = \frac{(l+1)}{(2l+1)} 4\pi G\rho_c \left[1 - \left(\frac{\frac{d_b}{h}}{C(\rho_c)} - \frac{d_b}{h} + 1 \right) C \left(\Delta\rho \left(1 - \frac{d}{R} \right)^2 \right) \left(1 - \frac{d}{R} \right)^l \right] \tag{4.25}$$

When $C = 1$ (pure isostasy), both of these expressions reduce to

$$Z(l) = \frac{(l+1)}{(2l+1)} 4\pi G\rho_c \left[1 - \left(1 - \frac{d}{R} \right)^l \right] \tag{4.26}$$

and admittance will always be positive since $(1 - d/R)^l$ must always be less than 1.

Finally, in the limit of an infinitely rigid shell ($C = 0$), for which we must specify both d_t and d_b, it can be shown that the admittance is

$$Z(l) = \frac{(l+1)}{(2l+1)} 4\pi G\rho_c \left[1 - \frac{d_b \Delta\rho}{d_t \rho_c} \left(1 - \frac{d}{R} \right)^{l+2} \right] \tag{4.27}$$

In general (i.e., when $0 < C < 1$), admittance depends on topography (h), the amount of top and/or bottom loading (d_t and/or d_b), as well as the elastic thickness, T, and the mean shell thickness, d. For a given wavelength, mean shell thickness (d), elastic thickness (T), and a fixed, positive h, admittance is a positive linear function of d_t (Figure 4.6) and crosses zero when $d_t = h \left(1 - \left(\frac{1}{C(\rho_c)} - 1 \right)^{-1} \left(\left(1 - \frac{d}{R} \right)^{-l} - 1 \right) \right)$. When both top and bottom loading have taken place, and if h is known, admittance may be either positive or negative, and is uniquely defined if either d_t or d_b is specified.

Based on equation (4.25), it can be shown that, when loading occurs purely from the top (i.e., $d_b = 0$), admittance is independent of surface relief, h, and

is given by

$$Z(l) = \frac{(l+1)}{(2l+1)} 4\pi G\rho_c \left[1 - C\left(\Delta\rho\left(1 - \frac{d}{R}\right)^2\right)\left(1 - \frac{d}{R}\right)^l\right] \tag{4.28}$$

which is necessarily positive, since both C and $(1 - d/R)^l$ are always less than 1. Based on (4.24), when loading occurs purely from the bottom (i.e., $d_t = 0$), admittance is, again, independent of surface relief, h, and is given by

$$Z(l) = \frac{(l+1)}{(2l+1)} 4\pi G\rho_c \left[1 - \frac{1}{C(\rho_c)}\left(1 - \frac{d}{R}\right)^l\right] \tag{4.29}$$

which is positive as long as $C(\rho_c) > (1 - d/R)^l$. For degree 3, this is always true for the parameters given in Table 4.2.

Hence, from Figure 4.6, we see that degree-3 admittance may be negative only if d_t/h is negative (i.e., when erosion has occurred at topographic highs) or if substantially different parameter values are adopted. To obtain a negative degree-3 admittance with pure bottom loading would require an increase of $\sim 30\%$ in the ratio of Young's modulus to the ice shell density (E/ρ_c). It is also possible to obtain a negative admittance without erosion for sufficiently large elastic thicknesses and sufficiently short wavelengths (e.g., for $l = 6$ when $T > 350\,\mathrm{km}$, or for $l = 9$ when $T > 200\,\mathrm{km}$).

4.3.2 Interpretation

Having developed our admittance model, and having seen that negative top loading (that is, erosion at topographic highs) is required in order to give rise to negative admittance at degree 3, we can now use equation (4.24) to see how admittance varies as a function of top load (d_t) and the elastic layer thickness

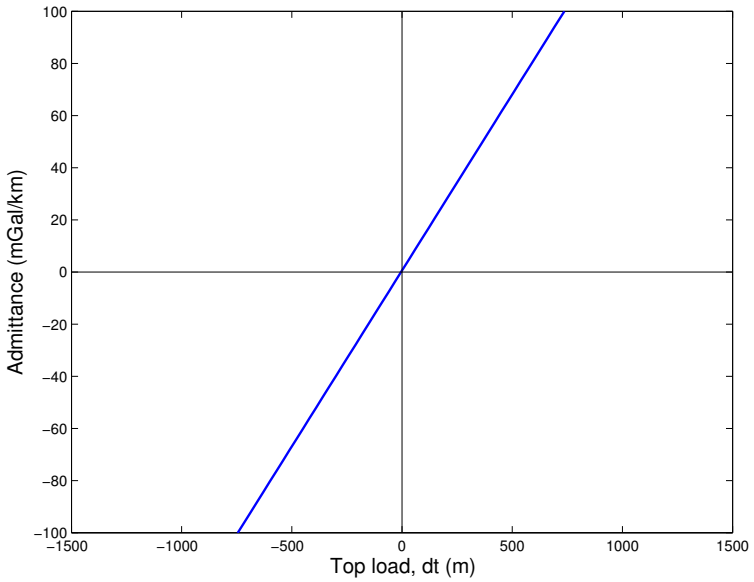

Figure 4.6: Admittance as a function of top load (d_t, where negative d_t indicates erosion) when $h = 66\,\text{m}$, $T = d = 200\,\text{km}$ and assuming the properties listed in Table 4.2.

Table 4.2: Parameter values assumed for admittance calculations

Parameter	Symbol	Assumed Value
Poisson's ratio for ice	ν	0.25
Young's modulus for ice	E	$9\,\text{GPa}$
Crustal (ice shell) density	ρ_c	$920\,\text{kg/m}^3$
Mantle (subsurface ocean) density	ρ_m	$1000\,\text{kg/m}^3$
Titan's mean density	$\overline{\rho}$	$1880\,\text{kg/m}^3$
Titan's radius	R	$2575\,\text{km}$
Acceleration due to gravity at the surface	g	$1.35\,\text{m/s}^2$

(T). This allows us to constrain the relationship between elastic thickness and the amount of erosion/deposition that must have taken place. Figure 4.7a illustrates the admittance corresponding to Figure 4.3 and shows that more than 100 m of surface erosion is required even for very large (~ 400 km) elastic thicknesses. If the elastic thickness is less than 40 km, more than ~ 1 km of erosion is required. Figure 4.7b plots combinations of d, T and d_t that satisfy the observed admittance. For an ice-shell thickness of 200 km, for example, more than 200 m of erosion are required.

Our results suggest that the negative admittance we observe at degree-3 is the result of negative gravity anomalies from large roots dominating over the positive gravity anomalies from the associated topography. We tested this scenario by computing, everywhere over the surface of Titan, the gravity anomaly implied by the observed topography and then comparing the result with the observations (Figure 4.8c). The gravity anomaly is obtained by multiplying the observed degree-3 topography (Figure 4.8a) by equation (4.24), assuming $T = d = 200$ km and a degree-3 erosion amplitude of 293 m (i.e, 293 m of erosion at the topographic peaks and 293 m of deposition in the valleys). This is the amount of erosion required to produce -39 mGal/km, the admittance obtained directly (i.e., neglecting uncertainties) from the SOL1a gravity (*Iess et al.*, 2012) and the Deg6-exp topography (*Zebker et al.*, 2012) (see section 4.2.3). Figure 4.8b shows the resulting gravity anomaly, computed everywhere over the surface. The gravity field predicted through this procedure resembles the observed field (compare panels (b) and (c) in Figure 4.8). Assuming the mantle density given in Table 4.2, the implied root thickness amplitude is ~ 1.4 km.

As illustrated in Figure 4.6, admittance is approximately a direct linear

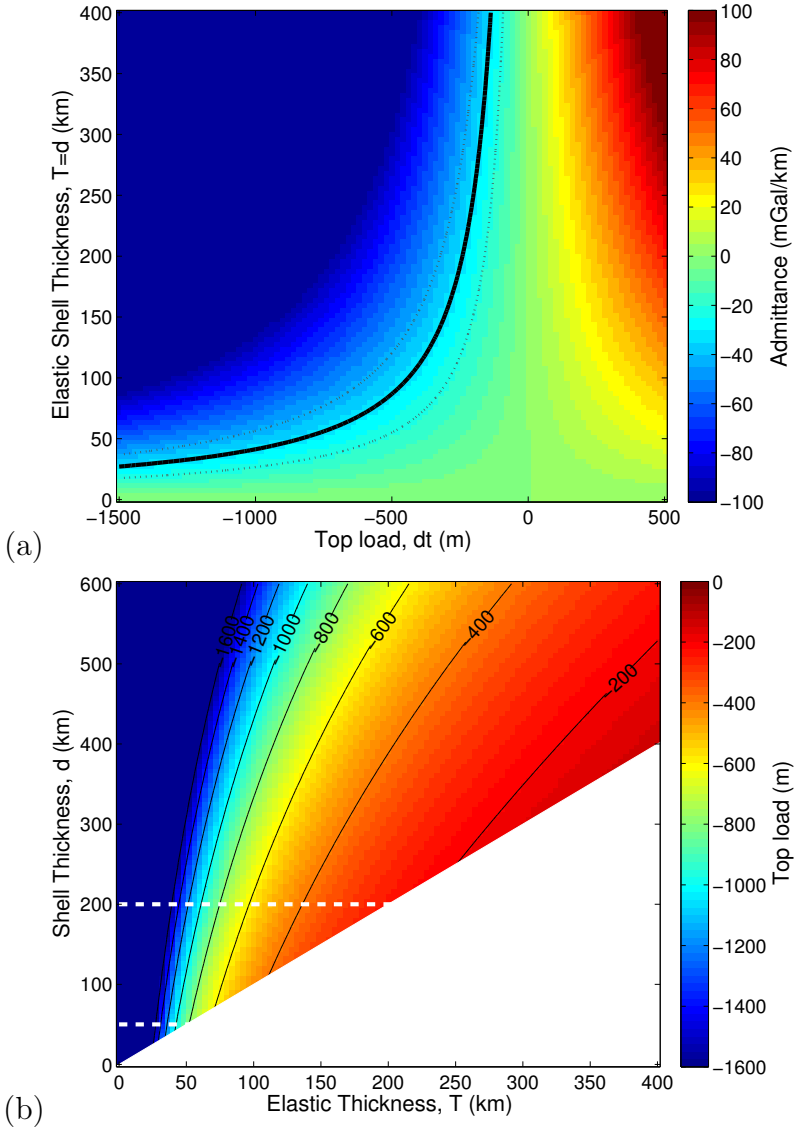

Figure 4.7: Model predictions of admittance and erosion. (a) Degree-3 admittance predicted by our model for various combinations of elastic thickness T and top load d_t, here assuming that T equals the shell thickness d. Larger values of T correspond to smaller values of C (that is, less compensation). Negative top load indicates erosion at topographic highs and deposition at topographic lows. The solid black line indicates the admittance corresponding to Figure 4.3 (-32 mGal/km); the dashed lines indicate the 1σ uncertainty on that estimate. Whereas the rheology of ice implies that $T < 0.5d$ (section 4.4.1), assuming that $T \approx d$ leads to conservative estimates of erosion. (b) Top load amplitude, d_t, required to produce the observed degree-3 admittance for various combinations of total shell thickness d and elastic thickness T. Dashed white lines highlight the likely range of Titan's ice shell thickness, 50–200 km. Both (a) and (b) were generated assuming a degree-3 topographic amplitude h of 66 m.

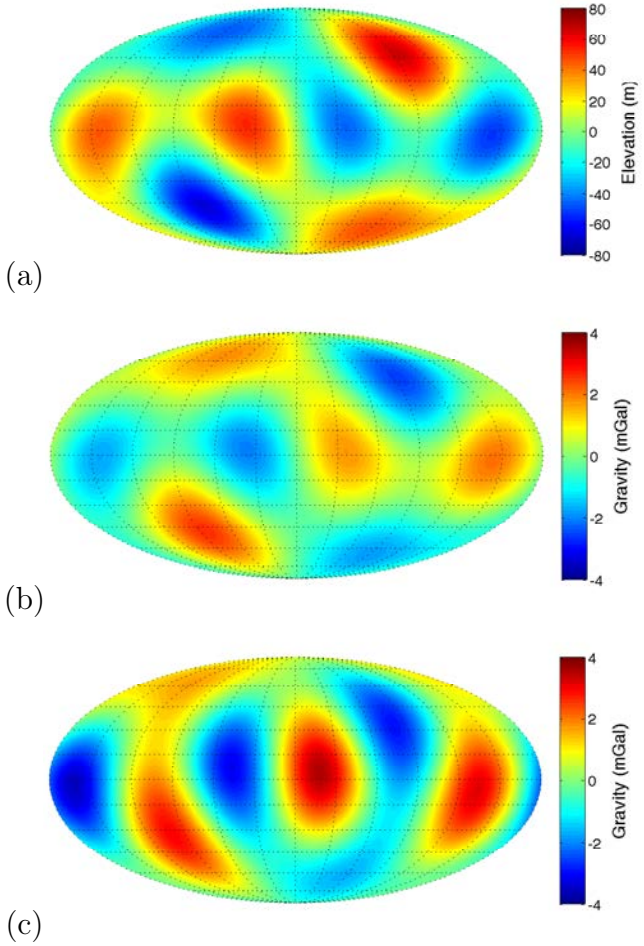

Figure 4.8: Degree-3 topography and gravity maps: (a) Deg6-exp topography (*Zebker et al.*, 2012); (b) gravity computed as described in section 4.3.2 (assuming $T = d = 200\,\text{km}$ and 293 m of erosion); (c) SOL1a gravity (*Iess et al.*, 2012).

function of top load (d_t). Conversely, the top load required to produce a given admittance can be obtained by solving equation (4.24) for d_t:

$$d_t = h\left(1 - \left(\frac{1}{C(\rho_c)} - 1\right)^{-1}\left[\left(1 - \frac{Z(l)}{4\pi G\rho_c}\frac{(2l+1)}{(l+1)}\right)\left(1 - \frac{d}{R}\right)^{-l} - 1\right]\right) \tag{4.30}$$

Based on (4.30), Figure 4.9 shows how the implied erosion (negative d_t) varies with the estimated admittance given various combinations of shell thickness (d) and elastic thickness (T). The dashed black line corresponds to $Z(3) = -32\,\mathrm{mGal/km}$, the admittance estimate obtained from the Monte Carlo analysis (i.e., accounting for uncertainties) based on the SOL1a gravity (*Iess et al.*, 2012) field and the Deg6-exp topography (*Zebker et al.*, 2012) solution. This is also the admittance assumed in generating Figure 4.7b. The $\pm 11\,\mathrm{mGal/km}$ uncertainty in that admittance estimate (Figure 4.4) translates to $\pm 81\,\mathrm{m}$ uncertainty in the erosion estimate when $T = d = 200\,\mathrm{km}$. Different combinations of T and d lead to slightly different uncertainties, but roughly $\pm 30\%$ is typical.

Although, as we will argue in section 4.4.1, the ice shell is not likely to be entirely elastic, adopting $T = d$ leads to more conservative estimates of the magnitude of erosion. For example, the magnitude of erosion required to give rise to $Z(3) = -32\,\mathrm{mGal/km}$ is $\sim 241\,\mathrm{m}$ when we assume $T = d = 200\,\mathrm{km}$ and $\sim 577\,\mathrm{m}$ when we assume $T = 100\,\mathrm{km}$, $d = 200\,\mathrm{km}$.

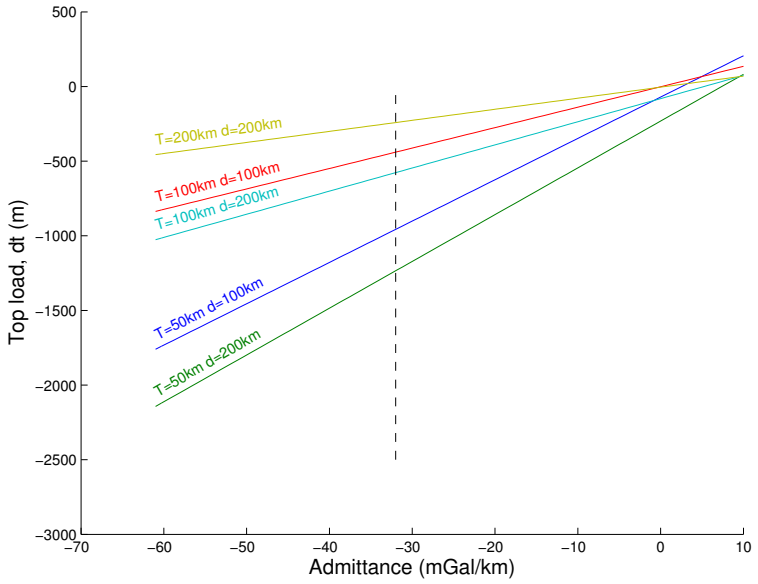

Figure 4.9: Magnitude of implied erosion as a function of admittance given several combinations of mean shell thickness (d) and elastic thickness (T). Negative top loads correspond to surface erosion. The dashed black line indicates the mean admittance estimate obtained from the Monte Carlo analysis based on the SOL1a gravity (*Iess et al.*, 2012) and the Deg6-exp topography (*Zebker et al.*, 2012) (-32 mGal/km).

4.4 Discussion

4.4.1 Ice Shell Structure and Rigidity

Throughout our analysis, we assume the ice shell to be in an equilibrium state where the various forces (flexure within the elastic part of the shell, weight of the overlying topography, and buoyancy of the root) are in balance. This is reasonable because the vertical response time of the shell should be fast compared with the loading timescale. The survival of large-impact basin rims and other topographic features (*Neish et al.*, 2013; *Moore et al.*, 2013, 2014) rules out erosion amplitudes greater than ~ 1 km, implying a shell elastic thickness greater than 40 km (Figure 4.7). This high rigidity could be the result of a cold (ammonia-rich) subsurface ocean (*Moore and Pappalardo*, 2011; *Grasset*

et al., 2000) (section 4.4.1.1), a clathrate-rich shell (*Tobie et al.*, 2006) or low heat flux from the interior (section 4.4.1.2). The addition of a rigid shell would slightly reduce the k_2 tidal Love number, but not enough to conflict with the measured value (*Iess et al.*, 2012) (section 4.4.1.5). The implied elastic thickness rules out a vigorously convecting shell, limits the potential for widespread cryovolcanism (*Moore and Pappalardo*, 2011; *Lopes et al.*, 2007), and permits the survival of lateral shell thickness variations (section 4.4.1.4). To generate the observed topography, our model requires shell thickness variations at degree 3; possible sources include tidal heating in a laterally heterogeneous shell (*Běhounková et al.*, 2012), and redistribution of material via non-Newtonian lateral flow (*Nimmo*, 2004) (section 4.4.1.3). A rigid conductive shell is also only weakly dissipative, potentially helping to explain Titan's high present-day orbital eccentricity (*Tobie et al.*, 2006; *Nimmo and Bills*, 2010).

4.4.1.1 Temperature Profile

Roughly speaking, ice will undergo a transition from elastic to viscous behavior at temperatures in the range $160 - 180\,\mathrm{K}$, depending on the exact strain rate and grain size assumed (*Nimmo et al.*, 2002). For a conductive ice shell with basal temperature $T_b = 270\,\mathrm{K}$, the elastic thickness (T) will then be 38-50% of the total shell thickness (d), while if $T_b = 210\,\mathrm{K}$, then T will be 58-75% of d. While the transition from elastic to viscous behavior will occur over some finite region, that region will be thin because of the very strong variation in viscosity with depth. Hence, a two-layer model is a good approximation.

In order to obtain conservative estimates for the elastic thickness and surface erosion, we assumed $T = d$ in parts of our analysis (e.g., Figure 4.7a). Such a scenario would require that $T_b \approx 180\,\mathrm{K}$, which may not be likely, but

is at least possible in the limit of an ammonia-water eutectic ocean, for which the freezing point is $\sim 176\,\mathrm{K}$.

4.4.1.2 Heat Flux

Assuming a heat flux of $F \approx 4\,\mathrm{mW/m^2}$ through Titan's (conductive) ice shell (*Nimmo and Bills*, 2010), and allowing thermal conductivity to vary with temperature (*Klinger*, 1980), we can estimate the shell's elastic thickness (T) according to

$$T \approx \frac{567}{F} \ln\left(\frac{T_z}{T_s}\right) \tag{4.31}$$

where T_s is the surface temperature and T_z is the temperature at which the shell transitions from elastic to viscous behavior. The resulting estimated elastic thickness is $T \approx 82 - 98\,\mathrm{km}$. Despite the highly approximate nature of this analysis, it yields an elastic thickness that is consistent with our estimates (Figure 4.7b). Larger elastic thicknesses are possible, but would correspond to a lower heat flux.

4.4.1.3 Origin of Long-Wavelength Topography

Like any tidally locked satellite, Titan's shape is primarily determined by tidal and rotational distortion. Centrifugal forces from the rotation lead to an equatorial bulge (flattening at the poles) and the permanent tide leads to elongation along the Titan-Saturn axis. The degree-2 and degree-4 topography will also be affected by variations in ice shell thickness that arise due to tidal heating (*Nimmo and Bills*, 2010). As discussed below (section 4.4.1.4), non-Newtonian flow within the lower part of the ice shell could cause degree-3 shell thickness variations to develop from a pattern that is initially confined to

degrees 2 and 4. This may, in part, explain the source of the observed degree-3 topography. Since ongoing tidal heating will support the maintenance of shell thickness variations at degrees 2 and 4, those variations could persist even as lower crustal flow continues to generate shell thickness variations at degree 3.

Heterogeneities in the ice shell could also contribute to a departure from the purely degree-2 and -4 pattern predicted from tidal heating and could thus be responsible for part of the shell thickness variations, and therefore topography, at degree 3.

4.4.1.4 Lateral Flow in the Ice Shell

Shell thickness variations lead to flow in the lowermost, low-viscosity part of the shell, which will tend to smooth out any such variations. For a Newtonian fluid, the timescale (τ) for removal of variations is given by (*Nimmo*, 2004)

$$\tau = \frac{\eta_b}{g\Delta\rho\delta^3 k^2} \tag{4.32}$$

where η_b is the viscosity at the base of the shell, g is the acceleration due to gravity, $\Delta\rho$ is the density contrast between the shell and the fluid underneath, δ is the effective channel thickness in which flow occurs, and k is the wavenumber ($k = l/R$, where l is spherical harmonic degree and R is the planetary radius).

Assuming a linear temperature gradient and a thermal conductivity (*Klinger*, 1980) which goes as c/T, where $c = 567\,\mathrm{W/m}$, the effective channel thickness (δ) is given by (*Nimmo*, 2004)

$$\delta = \frac{R_g T_b d}{Q \ln\left(T_b/T_s\right)} \tag{4.33}$$

where R_g is the gas constant, d is the shell thickness, Q is the activation energy

and T_b and T_s are the basal and surface temperatures, respectively. Finally, the viscosity η_b is given by

$$\eta_b = \eta_{ref} \exp\left[\frac{Q}{R_g}\left(\frac{1}{T_b} - \frac{1}{T_{ref}}\right)\right] \tag{4.34}$$

where the viscosity of ice is η_{ref} at a reference temperature T_{ref}.

Table 4.3 gives τ as a function of T_b for spherical harmonic degree 3. Here, we have assumed $\eta_{ref} = 10^{14}\,\mathrm{Pa\,s}$ at $T_{ref} = 273\,\mathrm{K}$, $Q = 60\,\mathrm{kJ/mol}$, $T_s = 90\,\mathrm{K}$, $d = 100\,\mathrm{km}$, $g = 1.35\,\mathrm{m/s^2}$, $\Delta\rho = 80\,\mathrm{kg/m^3}$ and $R = 2575\,\mathrm{km}$. For the range of T_b values explored, $\delta = 3.4\,\mathrm{km}$. Rheological parameters (*Goldsby and Kohlstedt*, 2001) are subject to some uncertainty; nonetheless, the results of Table 4.3 serve to illustrate the main conclusion, which is that flow is slow if the ocean is sufficiently cold ($T_b \lesssim 220\,\mathrm{K}$). A temperature of 220 K corresponds to 25 wt% ammonia in a simple $NH_3 - H_2O$ system (*Kargel*, 1998).

Table 4.3: Viscosity and timescale for removal of degree-3 ice shell thickness variations as a function of temperature.

T_b (K)	η_b (Pa s)	τ (Myr)
273	1.0×10^{14}	0.55
250	1.1×10^{15}	6.34
230	1.4×10^{16}	77.6
210	2.8×10^{17}	1491

In practice, the rheology of ice may be non-Newtonian, in which case our flow timescales will be underestimates (*Nimmo*, 2004), permitting larger values of T_b. An important consequence of non-Newtonian flow is that mode-coupling occurs: an initially degree-2 or degree-4 pattern (e.g., due to tidal heating) will develop a degree-3 component as flow proceeds, thus potentially explaining the observed degree-3 signal (see 4.4.1.3).

Finally, we note that if tidal heating is indeed occurring, a balance may develop wherein shell thickness variations are being generated by tidal heating just as quickly as lateral flow is removing those variations. Such an equilibrium situation could be stable even if the relaxation timescales are relatively short, again permitting higher values of T_b.

4.4.1.5 Effect on Tidal k_2

The tidal Love number, k_2, of Titan has been measured (*Iess et al.*, 2012), with a 2-σ lower bound on k_2 of 0.413-0.439. It is therefore important to check that the kind of rigid elastic lid that we are proposing does not contradict the observations. To do so, we constructed a highly simplified model for the interior of Titan (Table 4.4).

Table 4.4: Simple model of Titan's interior, used to determine the effect of a rigid shell on the tidal Love number, k_2.

Layer	**Outer Radius (km)**	**Rigidity (GPa)**	**Viscosity (Pa s)**	**Density** (kg/m^3)
Solid Core	2110	3	10^{21}	2600
High-Pressure Ice	2275	3	10^{21}	1000
Ocean	$2575 - d$	0	0	1000
Rigid Outer Shell	2575	3	10^{21}	920

This model is not meant to be realistic, but suffices to demonstrate our results. The density structure approximately satisfies the nominal moment of inertia constraint, while the low rigidity in the inner layers is designed to reproduce the observed k_2. We followed *Moore and Schubert* (2003) in calculating the model k_2 values. For rigid shell thicknesses of d =5, 100 and 200 km we obtained k_2 values of 0.568, 0.519 and 0.413, respectively. Hence, adding a rigid shell of thickness 100 km or 200 km reduces k_2 by 9% or 27%,

respectively—not enough to contradict the observed k_2 values (*Iess et al.*, 2012).

4.4.2 Erosion and Deposition

Our lower bound on the extent of erosion and deposition (200 m) over global length scales is compatible with estimated local amounts based on impact crater degradation (*Neish et al.*, 2013; *Moore et al.*, 2013, 2014), but somewhat larger than estimates from fluvial incision (*Black et al.*, 2012). The implied vertical erosion/deposition rate is of the order of a meter per million years, comparable to the lower end of aeolian deposition rates measured on Earth (*Patterson et al.*, 1999); erosion may be occurring by physical comminution, dissolution or sublimation. Because Titan's topography is high at the equator, we predict maximum erosion occurring at the equator and sediment transport, via fluvial or aeolian processes, predominantly towards the poles. An alternative possibility is transport in the vapor phase, if the mobile material has a sublimation temperature close to that of the surface temperature.

4.4.3 Degree-2 Admittance and Fluid Love Number

Degree-2 admittance analysis of Titan's ice shell is complicated by the fact that the body is tidally and rotationally distorted. Tidal/rotational distortion dominates the degree-2 gravity signal and also makes a large contribution to the degree-2 topography. If we assume that basal freezing, uplift and erosion processes act similarly at degrees 2 and 3, then ice shell thickness variations should be responsible for a portion of the observed degree-2 gravity and topography signals.

Separating the degree-2 gravity and topography signals into their hydrostatic (i.e., tidal/rotational) and non-hydrostatic (i.e., due to ice shell thickness variations) parts is necessarily an iterative process. We begin by estimating Titan's fluid Love number, h_{2f}, from the observed degree-2 gravity signal (J_2) according to

$$h_{2f} = 1 + \frac{6}{5}\frac{g}{R\omega^2}J_2 \tag{4.35}$$

where R is Titan's mean radius, g is the mean surface gravity, and ω is the angular frequency of rotation. Based on the observed gravity field (*Iess et al.*, 2012), we obtain $h_{2f} \approx 2.0$ (moment of inertia factor ~ 0.34). This allows us to predict the expected hydrostatic topography, h_T according to

$$h_T = h_{2f}\frac{R^2\omega^2}{g}\left[\frac{1}{2}\left(3\cos^2\phi + 1\right)\left(1 - \cos^2\theta\right) - \frac{5}{6}\right] \tag{4.36}$$

which we then subtract from the observed topography to get the non-hydrostatic topography, h_{shell} (i.e., that which is due to variations in ice shell thickness). We then multiply h_{shell} by equation (4.24) to estimate the gravity signal due to an ice shell with anomalously deep roots (the large root size will be forced implicitly by our choices of C and d_t, both of which will be a function of mean shell thickness, d and elastic thickness, T). Having obtained this gravity anomaly due to ice shell thickness variations (Δg_{shell}), we conclude that the portion of the gravity signal that is due to tidal distortion is $\Delta g_{tidal} = \Delta g_{total} - \Delta g_{shell}$. Finally, we use the newly obtained tidal gravity field to get an updated estimate for h_{2f}, again using (4.35). After 3-4 iterations, our estimate for h_{2f} converges to the fourth decimal place, allowing us to separate, in a self-consistent way, the tidal/rotational and ice shell thickness contributions to the degree-2

gravity signal. The final estimate for h_{2f} depends on the assumed mean shell thickness (d) and elastic thickness (T), as illustrated in Figure 4.10. If we assume that $T = 100\,\text{km}$ and $d = 200\,\text{km}$, then we obtain $h_{2f} \approx 2.15$ (moment of inertia factor ~ 0.36).

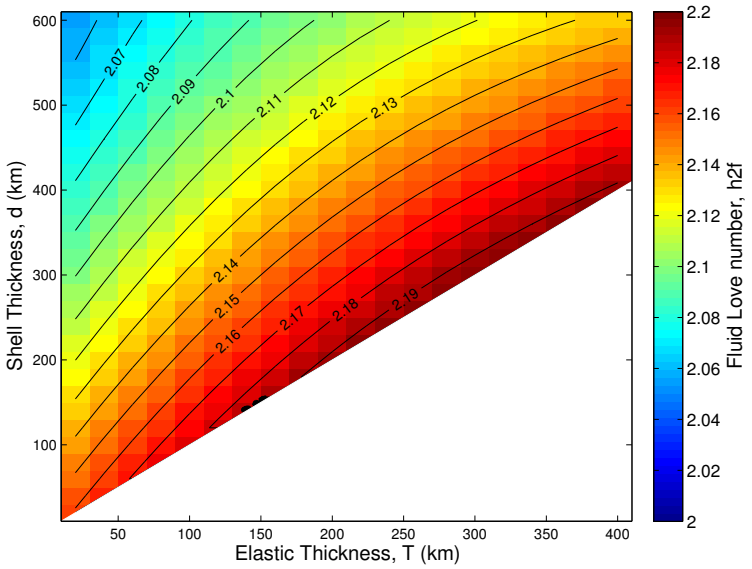

Figure 4.10: Estimate for Titan's fluid Love number, h_{2f}, as a function of mean shell thickness (d) and elastic thickness (T).

Using this fluid Love number, we can estimate the non-hydrostatic portions of the degree-2 topography and gravity signals. Figure 4.11 shows how the observed degree-2 gravity field (a) compares with the predicted field (b), where the predicted field is the sum of the estimated hydrostatic gravity (c), based on $h_{2f} = 2.15$, and the gravity anomaly expected from the estimated ice shell thickness variations (d), assuming an erosion amplitude of 577 m (obtained from Figure 4.7b assuming $T = 100\,\text{km}$ and $d = 200\,\text{km}$). The amplitude of the estimated non-hydrostatic gravity is $\sim 2\,\text{mGal}$ while the estimated hydrostatic gravity amplitude is $\sim 21\,\text{mGal}$. This is one measure of Titan's departure from hydrostatic equilibrium.

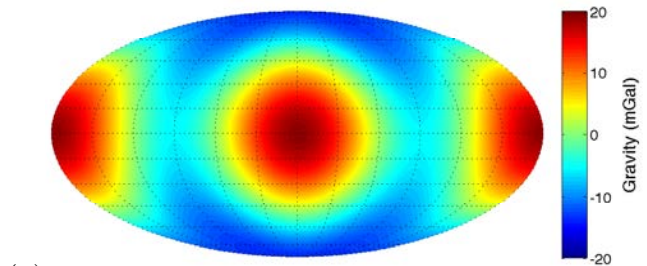

(a)

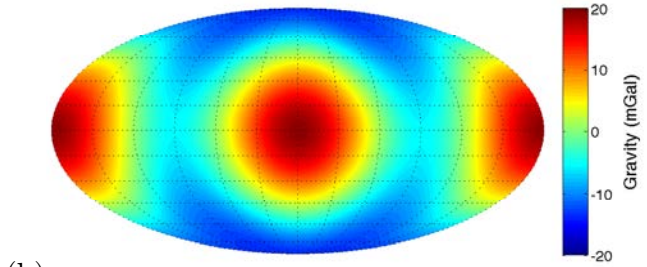

(b)

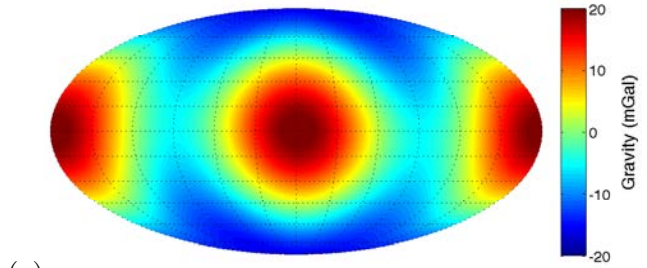

(c)

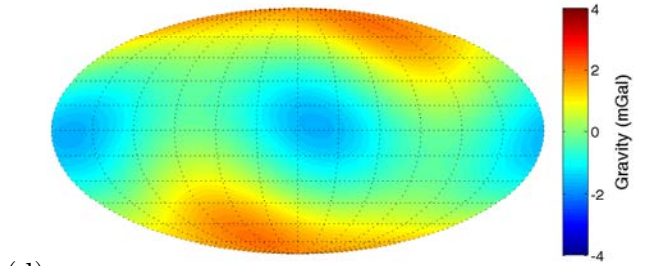

(d)

Figure 4.11: Degree-2 gravity maps centered on the sub-Saturnian point (180° longitude): (a) SOL1a gravity (*Iess et al.*, 2012); (b) total predicted gravity signal; (c) gravity signal caused by tidal/rotational distortion assuming $h_{2f} = 2.15$; (d) gravity signal caused by ice shell thickness variations assuming $T = 100\,\text{km}$ and $d = 200\,\text{km}$, and therefore 577 m of erosion.

4.4.4 Degree-4 Predictions

Assuming once again that the observed topography is the result of uplift due to basal freezing and that the surface has experienced a similar magnitude of erosion at degrees 3 and 4, we can predict the admittance at degree 4. We first obtain the magnitude of degree-3 erosion (d_t) over a range of values for T and d from Figure 4.7b. Using this same value of d_t for the degree-4 erosion amplitude, we then use equation (4.24) to estimate the admittance over the same range of values for T and d. Figure 4.12 illustrates that the degree-4 admittance should be negative if the elastic thickness, T, accounts for most of the total shell thickness, d.

If, for example, $T = d = 200\,\mathrm{km}$, and we assume the same magnitude of erosion at degrees 3 and 4 (in this case, 241 m), then based on the observed topography (*Zebker et al.*, 2012) (Figure 4.13a), we obtain a degree-4 admittance of $-5.1\,\mathrm{mGal/km}$ and we can compute the implied degree-4 gravity anomaly everywhere over the surface (Figure 4.13b). Although the amplitudes are similar, our result is spatially unlike the reported degree-4 gravity field (*Iess et al.*, 2012) (Figure 4.13c). However, as noted in section 4.2.1, the degree-4 gravity field is not currently regarded as reliable; future gravity flybys are expected to improve the determination of the degree-4 field by a factor of two, providing a better test of our prediction. Note that if we assume instead that $T = 100\,\mathrm{km}$ and $d = 200\,\mathrm{km}$ (the corresponding erosion amplitude being 577 m), the greater compensation leads to a muted gravity signal and an admittance that approaches zero. Hence a weak degree-4 gravity signal, or a degree-4 admittance that is positive or only weakly negative, may be an indication that the elastic layer accounts for a smaller portion of the total shell

thickness (Figure 4.12).

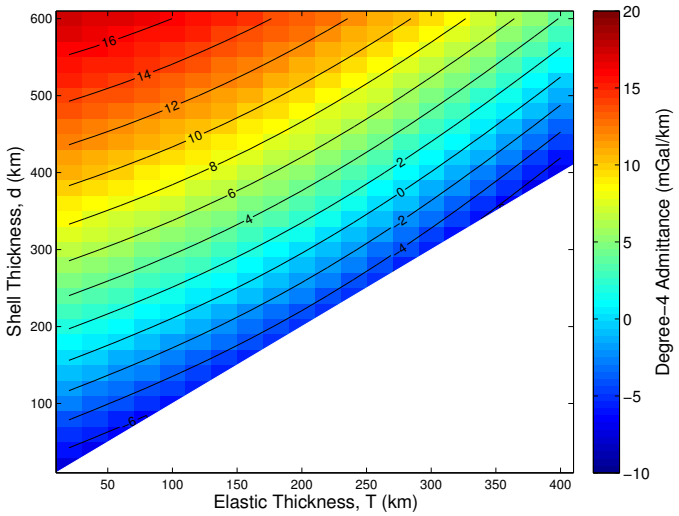

Figure 4.12: Degree-4 admittance predicted for a range of elastic thicknesses (T) and total shell thicknesses (d).

4.5 Conclusions

Titan's degree-3 gravity and topography exhibit a strong inverse correlation and, consequently, the degree-3 admittance is substantially negative, even when model uncertainties are taken into account. Although negative admittances are not common, our model predicts negative admittances at degree 3 under a particular set of conditions: when the ice shell is substantially rigid (with an elastic thickness greater than $\sim$ 40 km), when it has been loaded primarily from below (e.g., due to basal freezing), and when some few hundred meters of erosion has taken place at topographic highs. The conclusion that the ice shell is rigid rules out vigorous convection and limits the potential for widespread cryovolcanism. The substantial erosion required by our model suggests a tendency for sediment to be transported from the high-standing

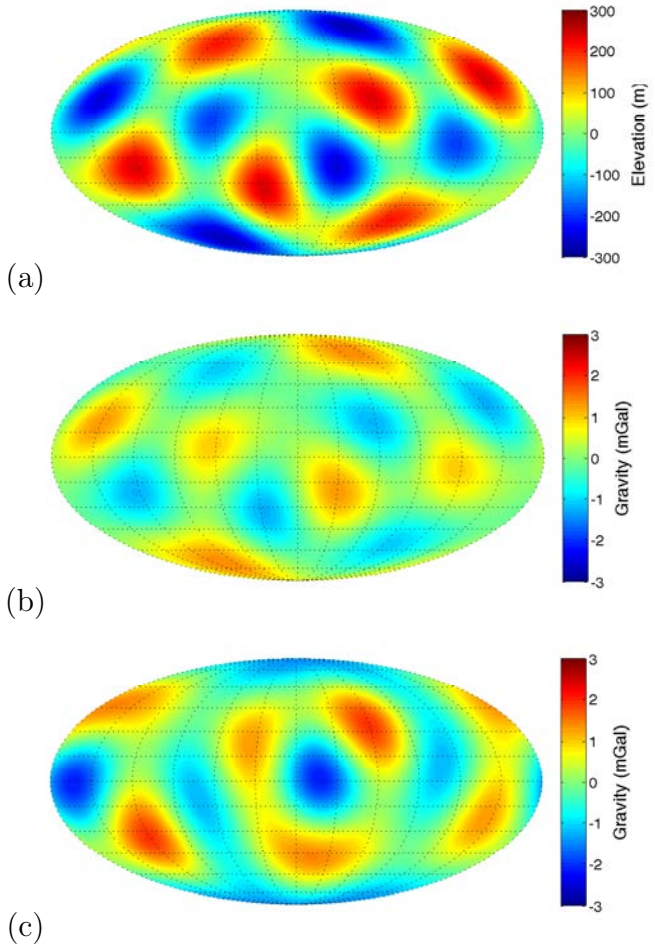

Figure 4.13: Degree-4 topography and gravity maps centered on the sub-Saturnian point (180° longitude): (a) Topography (*Zebker et al.*, 2012); (b) Predicted gravity signal caused by ice shell thickness variations assuming $T = d = 200$ km and therefore 241 m of erosion; (c) SOL1b gravity (*Iess et al.*, 2012) (not currently considered reliable at degree 4).

topography near the equator to the lower elevations found toward the poles.

If similar erosion and deposition processes are taking place at degree 2, then the present-day degree-2 topography is smaller than what should be expected from tidal and rotational distortion alone. This would imply that the observed degree-2 gravity signal is an underestimate of the hydrostatic gravity and that, consequently, Titan's fluid Love number has been underestimated. This would indicate that Titan has a higher moment of inertia (and is thus even less centrally condensed) than previously thought, reinforcing the need to understand how so large a body could have accreted without undergoing more complete differentiation. Our analysis suggests that, if the elastic thickness exceeds half the total shell thickness, the degree-4 admittance will also be negative. Future *Cassini* gravity fly-bys will improve the determination of the degree-4 gravity field by a factor of two and will therefore provide a partial test of this prediction. If a non-negative degree-4 admittance is observed, that may be an indication that a smaller portion (less than half) of the ice shell is elastic.

Acknowledgements

We thank the *Cassini* radar science team, M. Manga, D. Stevenson, R. Pappalardo, W. McKinnon, and two anonymous reviewers for their suggestions. Portions of this work were supported by NASA grants NNX13AG02G and NNX11AK44G.

Chapter 5

Internal Structure of Enceladus

This chapter details analysis I carried out, along with Francis Nimmo, in support of Iess, L. et al. (2014), The Gravity Field and Interior Structure of Enceladus, *Science, 344*(6179), 78–80, doi:10.1126/science.1250551.

Abstract

With water-rich jets actively erupting from its South Polar Terrain (*Spitale and Porco*, 2007), Saturn's tiny moon Enceladus is one of the most compelling exploration targets in the solar system. A subsurface liquid sea or ocean is often presumed to be the source of the jets. However, without better knowledge of Enceladus' gravity field, it has been difficult to constrain interior structure models sufficiently to confirm the presence of an internal ocean. Here we combine the newly determined gravity field (*Iess et al.*, 2014), obtained from Doppler tracking of the *Cassini* spacecraft, with a shape model determined from limb profile analyses (*Nimmo et al.*, 2011), to constrain the interior structure of Enceladus, confirming that a subsurface ocean is likely. We employ an

admittance analysis that self-consistently separates the hydrostatic and non-hydrostatic components of the gravity and topography signals in a way that allows us to determine both the moment of inertia for Enceladus and the depth at which the topography may be compensated isostatically. The observations are most easily accommodated by a differentiated Enceladus, with moment of inertia $\sim 0.335MR^2$, surrounded by an H_2O mantle consisting of an outer ice shell, $20-40$ km thick, and a subsurface liquid ocean with an average thickness > 15 km.

5.1 Introduction

Enceladus, embedded in Saturn's E-ring, is a small ($\sim$ 250 km radius), but distinctly geologically active world (*Porco et al.*, 2006). In particular, its South Polar Terrain (SPT) is cross-cut by four major fissures, known as the "Tiger Stripes", along which more than 100 distinct geysers have been identified. The geysers spray water, rich in salts and organic compounds, out from the small moon, resulting in a bright, "snow" covered surface, and a persistent vapor plume that extends outward some 500 km (*Porco et al.*, 2006; *Spitale and Porco*, 2007). Shear heating (*Nimmo et al.*, 2007) has been proposed as a mechanism for the vapor production and a subsurface liquid sea or ocean, although not directly observed, is considered to be likely (*Spencer and Nimmo*, 2013).

Reliable internal structure models have not previously been available to help confirm or refute the existence of a subsurface ocean. Although good shape models have been available for some time (*Nimmo et al.*, 2011), determination of the gravity field, which requires dedicated flybys and modeling

of unknown non-gravitational disturbances (e.g., from plume drag), has only recently been completed (*Iess et al.*, 2014). Below, we combine the shape models with the newly determined gravity field in order to construct an interior structure model for Enceladus.

In Chapter 4, we used the spectral admittance, $Z(l)$, to quantify the relationship between Titan's gravity and topography, and used the result to draw conclusions about the thickness and elastic behavior of the ice shell. Our analysis was focused mainly on the degree-3 admittance since analysis of degree-2 admittance is complicated by the effects of tidal and rotational distortion. In the case of Enceladus, the gravity data are even more limited: the degree-2 gravity field is well constrained, but determination of the degree-3 field is limited to the zonal term (C_{30}) alone. Here, we instead take on the task of decomposing the degree-2 gravity and topography signals into their hydrostatic and non-hydrostatic components. The hydrostatic components of the degree-2 signal are controlled by tidal and rotational distortion. The remainder of the degree-2 gravity and topography signals are due to additional mass and shape anomalies that may arise, for example, from an irregular core shape (*Thomas et al.*, 2007; *McKinnon*, 2013), or from lateral variations in the thickness of the outer ice shell (*Nimmo and Bills*, 2010).

In section 5.2, we briefly describe the observed gravity and topography and the degree to which the degree-2 terms deviate from the expectation for a relaxed, hydrostatic body. In section 5.3, we review the relevant theoretical tools for modeling the hydrostatic gravity and topography, for computing admittances under various conditions of isostasy and flexure, and for determining the moment of inertia. In section 5.4, we discuss the results before concluding in section 5.5.

5.2 Observations

5.2.1 Gravity Field

The gravitational field of Enceladus is described by *Iess et al.* (2014) as non-normalized, dimensionless potential coefficients C^g_{lm}, S^g_{lm} such that the gravitational potential at the reference radius (R) can be written

$$U(\theta,\phi) = -\frac{GM}{R}\sum_{l=0}^{\infty}\sum_{m=0}^{l}\left(C^g_{lm}\cos m\phi + S^g_{lm}\sin m\phi\right)P_{lm}(\cos\theta)$$

where $P_{lm}(\cos\theta)$ are the non-normalized associated Legendre functions (see Appendix A), θ is colatitude, ϕ is longitude and C^g_{lm} and S^g_{lm} are non-normalized spherical harmonic coefficients of degree l and order m.

Enceladus' low-order gravity field was determined (*Iess et al.*, 2014) via radio tracking of the *Cassini* spacecraft during three separate flybys in which the spacecraft passed within 100 km of the moon, twice over the southern hemisphere (E9, E19) and once over the northern hemisphere (E12). Doppler data from the three flybys were analyzed separately and combined into a multi-arc solution (Figure 5.1). Constraining the gravity field was especially challenging in the case of Enceladus due to its small size ($\sim 250\,$km radius) but also due to non-gravitational effects including the spacecraft's interaction with the vapor plume, which causes appreciable drag in the $\sim 20\,$seconds around closest approach during passes over the southern hemisphere. Accounting for this effect, *Iess et al.* (2014) were able to constrain the major degree-2 terms (C^g_{20} and C^g_{22}) to 1% uncertainty along with the degree-3 zonal term (C^g_{30}) to 20% uncertainty.

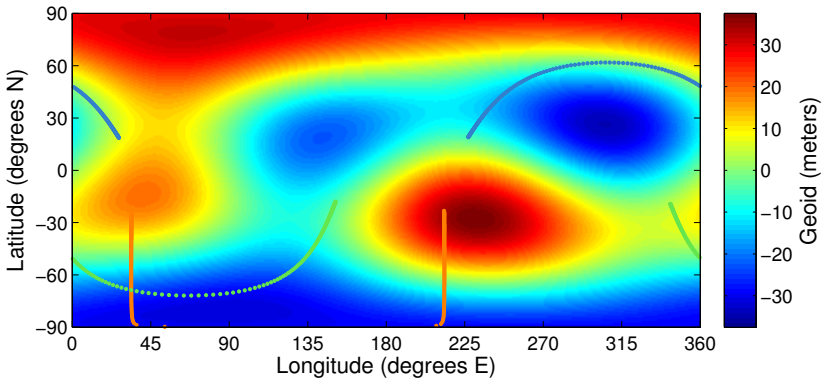

Figure 5.1: Enceladus' geoid with respect to the reference ellipsoid (see Appendix C). Also shown are the *Cassini* ground tracks from the three gravity flybys: E9 (orange), E12 (blue), and E19 (green).

5.2.2 Topography

Titan's topography is described by *Nimmo et al.* (2011) in terms of fully normalized spherical harmonic coefficients $\bar{C}^h_{lm}$, $\bar{S}^h_{lm}$, such that the topography at any point on the surface is given by

$$H(\theta,\phi) = \sum_{l=0}^{\infty}\sum_{m=0}^{l}\left(\bar{C}^h_{lm}\cos m\phi + \bar{S}^h_{lm}\sin m\phi\right)\bar{P}_{lm}(\cos\theta)$$

where $\bar{P}_{lm}(\cos\theta)$ are the fully normalized associated Legendre functions (see Appendix A). To facilitate direct comparison with the non-normalized gravity coefficients, we obtain the non-normalized coefficients C^h_{lm}, S^h_{lm} from the normalized coefficients with

$$\{C,S\}^h_{lm} = \sqrt{(2-\delta_{0m})\,(2l+1)\,\frac{(l-m)!}{(l+m)!}}\,\left\{\bar{C},\bar{S}\right\}^{\,h}_{lm} \tag{5.1}$$

so that the topography is described by

$$H(\theta,\phi) = \sum_{l=0}^{\infty}\sum_{m=0}^{l}\left(C^h_{lm}\cos m\phi + S^h_{lm}\sin m\phi\right)P_{lm}(\cos\theta)$$

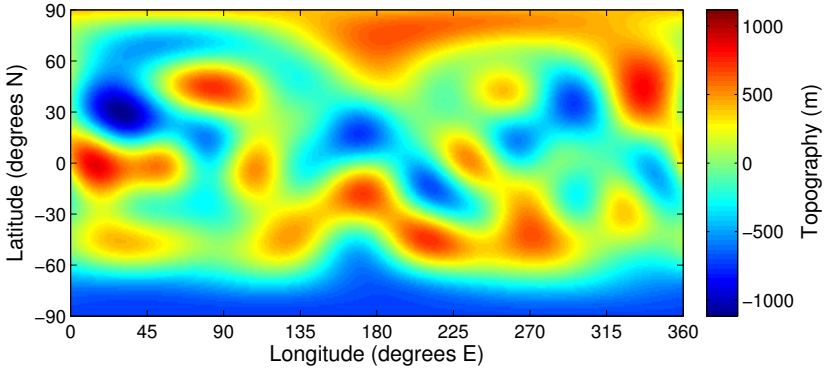

Figure 5.2: Enceladus' topography for harmonic degrees 3 through 8.

where, again, $P_{lm}(\cos\theta)$ are the non-normalized associated Legendre functions.

Enceladus' topography was determined through analysis of limb-profiles (*Nimmo et al.*, 2011). 43 separate limb profiles were measured from images of Enceladus, providing 43 arcs of topographic data, which were then combined to constrain a global shape model up to spherical harmonic degree 8 (Figure 5.2). The shape model's uncertainty is less than 5% for C^h_{20}, about 2% for C^h_{22}, and about 1% for C^h_{30}.

5.2.3 Deviation from Hydrostatic Equilibrium

For tidally-locked (synchronous) satellites, the degree-2 shape and gravity field are dominated by rotational flattening and elongation due to the permanent tide (see Appendix C). If the body is in hydrostatic equilibrium, its shape and gravity field conform to the expectation for a body whose outer layer is an inviscid fluid, in which case, only the C_{20} and C_{22} terms are significant, and have the approximate ratio

$$\frac{-C_{20}}{C_{22}} = \frac{10}{3} \approx 3.33$$

While this approximation is excellent in most cases, it is an overestimate in the case of very fast-rotating bodies, such as Enceladus (*Tricarico*, 2014). For Enceladus, a ratio of ~ 3.25 may be more appropriate (*Mckinnon*, 2015). We will proceed here assuming the typical hydrostatic ratio of 10/3 but, for an analysis that builds on ours while taking this effect into account, see *Mckinnon* (2015).

For Enceladus, the gravity coefficients have the ratio

$$\frac{-C_{20}^{g}}{C_{22}^{g}} \approx 3.51 \pm 0.06$$

and the topography coefficients have the ratio

$$\frac{-C_{20}^{h}}{C_{22}^{h}} \approx 4.20 \pm 0.28$$

Whereas the topography deviates substantially from the hydrostatic expectation, the gravity field deviates only modestly. This is an indication that the excess non-hydrostatic topography may be largely compensated by internal density anomalies, as would be expected for topography that is supported isostatically. Perhaps the most conspicuous feature of the gravity field is the negative gravity anomaly over the South Polar Terrain (Figure 5.1). Such a gravity anomaly is expected given the large topographic depression in that region (Figure 5.2), but the magnitude of the gravity anomaly in relation to the magnitude of the topographic depression will be diagnostic of the degree to which the topography is compensated isostatically.

5.3 Theory

5.3.1 Separation of Hydrostatic Component

We begin by presuming that the gravity and topography coefficients can be decomposed into their hydrostatic and non-hydrostatic parts as follows

$$C_{lm}^{\mathrm{g}} = C_{lm}^{\mathrm{g,hyd}} + C_{lm}^{\mathrm{g,nh}} \tag{5.2}$$

$$C_{lm}^{\mathrm{h}} = C_{lm}^{\mathrm{h,hyd}} + C_{lm}^{\mathrm{h,nh}} \tag{5.3}$$

where $C_{lm}^{\mathrm{g,hyd}}$ and $C_{lm}^{\mathrm{h,hyd}}$ are the hydrostatic components: the parts of the signals that result from tidal and rotational distortion. The hydrostatic parts of the gravity and topography signals are a function of the body's moment of inertia. If we make an assumption about the moment of inertia factor (α), we can obtain the fluid Love number, h_{2f}, via the Radau-Darwin approximation (*Murray and Dermott*, 1999)

$$\alpha = \frac{I}{MR^2} = \frac{2}{3}\left(1 - \frac{2}{5}\sqrt{\frac{5}{h_{2f}} - 1}\right) \tag{5.4}$$

The fluid Love number describes the degree to which a body deforms in response to the tidal and rotational deforming potentials. Given the fluid Love number and using the present-day rotation rate, we can estimate the hydrostatic shape and gravity field (Appendix C). In terms of non-normalized spherical harmonic coefficients, these are

$$C_{20}^{\mathrm{h,hyd}} = -\frac{5}{6}\frac{R^2\omega^2}{g}h_{2f} \tag{5.5}$$

$$C_{22}^{\mathrm{h,hyd}} = \frac{1}{4}\frac{R^2\omega^2}{g}h_{2f} \tag{5.6}$$

The change in shape, and therefore mass distribution, also produces a corresponding change in the gravitational potential such that

$$C_{20}^{\mathrm{g,hyd}} = -\frac{5}{6}\frac{R\omega^2}{g}\left(h_{2f} - 1\right) \tag{5.7}$$

$$C_{22}^{\mathrm{g,hyd}} = \frac{1}{4}\frac{R\omega^2}{g}\left(h_{2f} - 1\right) \tag{5.8}$$

Of course, we don't yet know the moment of inertia (α), so any such calculation is only a guess. But if we make the key assumption that the non-hydrostatic gravity-to-topography ratios should be equal (i.e., that the admittance is isotropic), then the correct moment of inertia is the one that yields

$$Z_{20} = Z_{22}$$

where the component-wise admittance is defined as

$$Z_{lm} = \frac{C_{lm}^{\mathrm{g,nh}}}{C_{lm}^{\mathrm{h,nh}}} \tag{5.9}$$

More specifically,

$$Z_{20} = \frac{C_{20}^{\mathrm{g}} + \frac{5}{6}\frac{R\omega^2}{g}\left(h_{2f} - 1\right)}{C_{20}^{\mathrm{h}} + \frac{5}{6}\frac{R^2\omega^2}{g}h_{2f}} \tag{5.10}$$

$$Z_{22} = \frac{C_{22}^{\mathrm{g}} - \frac{1}{4}\frac{R\omega^2}{g}\left(h_{2f} - 1\right)}{C_{22}^{\mathrm{h}} - \frac{1}{4}\frac{R^2\omega^2}{g}h_{2f}} \tag{5.11}$$

The task now becomes finding a value of h_{2f} for which $Z_{20} = Z_{22}$.

5.3.2 Model Admittance

We already derived the model admittance in Chapter 4 (section 4.3.1). However, since we are now working with dimensionless gravitational potential coefficients rather than acceleration, admittance here has units of m^{-1}, and we must alter the equations slightly. Specifically, the admittances we use here will be those of the previous chapter (and *Hemingway et al.* (2013)) divided by $\frac{GM(l+1)}{R^2} = G\frac{4}{3}\pi R\bar{\rho}\,(l+1)$.

Much of our analysis here will make use of the simple case in which we assume that surface loads are compensated completely, for which the degree-l admittance is simply (*c.f.* equation (4.26) and section 5.3.3)

$$Z\,(l) = \frac{3\rho_{\mathrm{c}}}{(2l+1)\,R\bar{\rho}}\left(1 - \left(1 - \frac{d}{R}\right)^{l}\right) \tag{5.12}$$

where R and $\bar{\rho}$ are, respectively, the radius and bulk density of Enceladus, ρ_{c} is the density of the surface load, which we take to be the same as the density of the icy crust, and d is the compensation depth.

In the special case where we assume a surface load that is entirely uncompensated (i.e., supported rigidly, see section 5.3.3), then

$$Z\,(l) = \frac{3\rho_{\mathrm{c}}}{(2l+1)\,R\bar{\rho}} \tag{5.13}$$

5.3.3 Elastic Flexure

More generally, we may need to account for the effects of elastic flexure (bending and membrane stresses) in the lithosphere. If the lithosphere is at least partially elastic and is deflected downward by the addition of a surface load,

then the degree-l admittance is given by (*c.f.* equation (4.28))

$$Z\left(l\right) = \frac{3\rho_{\mathrm{c}}}{\left(2l+1\right)R\overline{\rho}}\left(1 - C_t\left(1 - \frac{d}{R}\right)^{l}\right) \tag{5.14}$$

where C_t is the degree of compensation assuming top-loading (where $C_t = 1$ means complete isostatic compensation and $C_t = 0$ means zero compensation, or perfectly rigid support). Similarly, if loading occurs purely from the bottom (i.e., under-plating) then the degree-l admittance is given by (*c.f.* equation (4.29))

$$Z\left(l\right) = \frac{3\rho_{\mathrm{c}}}{\left(2l+1\right)R\overline{\rho}}\left(1 - \frac{1}{C_b}\left(1 - \frac{d}{R}\right)^{l}\right) \tag{5.15}$$

where C_b is the degree of compensation assuming pure bottom-loading. The compensation terms C_t and C_b become important when considering the effects of elastic flexure (see Chapter 4, section 4.3.1 for the derivations) and are defined as

$$C_b = \frac{1}{1 + \frac{\mu}{\rho_{\mathrm{c}}}} \tag{5.16}$$

and

$$C_t = \frac{1}{1 + \frac{\mu}{\Delta\rho}\left(1 - \frac{d}{R}\right)^{-2}} \tag{5.17}$$

where $\Delta\rho = \rho_{\mathrm{m}} - \rho_{\mathrm{c}}$ is the density contrast at the water/ice interface (ρ_{m} is the density of the subsurface ocean "mantle"), where μ describes the flexural rigidity at a particular wavelength and gravity, and is defined in equation (4.21) as

$$\mu(l) = \left(1 - \frac{3\rho_{\mathrm{m}}}{(2l+1)\overline{\rho}}\right)^{-1}\frac{ET}{R^2 g}\left(\frac{\frac{T^2\left[l^3(l+1)^3 - 4l^2(l+1)^2\right]}{R^2 12(1-\nu^2)} + l(l+1) - 2}{l\left(l+1\right) - (1-\nu)}\right) \tag{5.18}$$

5.3.4 Moment of Inertia

For a simple, spherically symmetric, two-layer body, the moment of inertia is given by

$$I = \frac{8}{15}\pi \left(\rho_{\mathrm{o}} R^5 + (\rho_{\mathrm{i}} - \rho_{\mathrm{o}})\,(R-d)^5\right) \tag{5.19}$$

where the subscripts (i) and (o) refer to the inner and outer layers, respectively, and where d is the thickness of the mantle so that the core radius is $R_{\mathrm{core}} = R - d$. We will often discuss the normalized moment of inertia (also called the moment of inertia factor), $\alpha = \frac{I}{MR^2}$, which can be written

$$\alpha = \frac{2}{5\bar{\rho}} \left(\rho_{\mathrm{o}} + (\rho_{\mathrm{i}} - \rho_{\mathrm{o}}) \left(1 - \frac{d}{R}\right)^5\right) \tag{5.20}$$

where $\bar{\rho}$ is the bulk density of Enceladus.

5.4 Results and Discussion

5.4.1 Admittance and Moment of Inertia

Considering a range of possible moments of inertia, we use equations (5.4), (5.10), and (5.11) to compute the corresponding Z_{20} and Z_{22} admittances and find that the two independent estimates converge at $\sim 3.4 \times 10^{-7}\,\mathrm{m}^{-1}$ when the moment of inertia factor is ~ 0.335 (Figure 5.3).

Because we also have the zonal part of the degree-3 gravity field (C_{30}^g), we can compute Z_{30} and use it as an independent check on our admittance estimate (note that the degree-3 terms have no hydrostatic component so Z_{30} is obtained directly from equation (5.9) and does not depend on moment of inertia). Because they reflect behavior at different wavelengths, however, the degree-3

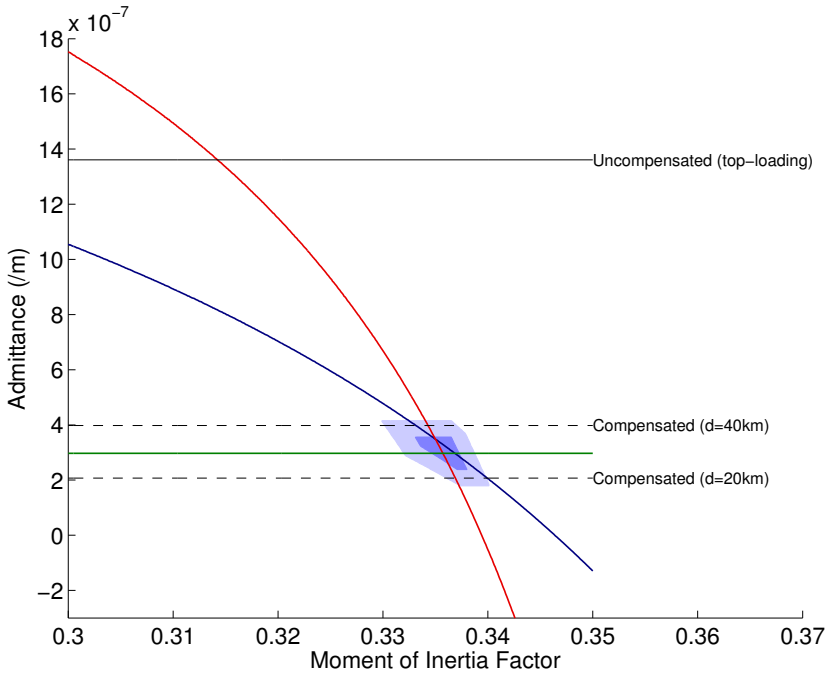

Figure 5.3: Region of 1σ agreement (dark blue) and 2σ agreement (pale blue) between the admittances estimated separately from the (2,0) (blue line), (2,2) (red line), and (3,0) (green line) terms. The (3,0) term has been multiplied by 0.99 to obtain the equivalent degree-2 value (see text, section 5.4.1). The solid line at $\sim 14 \times 10^{-7}\,\mathrm{m}^{-1}$ represents the admittance expected for uncompensated (rigidly supported) topography. The dashed horizontal lines near 2 and $4 \times 10^{-7}\,\mathrm{m}^{-1}$ represent the admittances expected for fully compensated topography with compensation depths (ice shell thicknesses) of 20 and 40 km, respectively.

Table 5.1: Parameter values assumed for admittance calculations

Parameter	**Symbol**	**Assumed Value**
Poisson's ratio for ice	ν	0.25
Young's modulus for ice	E	9 GPa
Crustal (ice shell) density	ρ_{c}	$920\,\mathrm{kg/m^3}$
Mantle (subsurface ocean) density	ρ_{m}	$1000\,\mathrm{kg/m^3}$
Enceladus' mean density	$\overline{\rho}$	$1609\,\mathrm{kg/m^3}$
Enceladus' radius	R	252.1 km
Enceladus' surface gravity	g	$0.114\,\mathrm{m/s^2}$

admittance (Z_{30}) cannot be compared directly with the degree-2 admittances (Z_{20} and Z_{22}). The relevant comparison is between the degree-2 estimates (Z_{20} and Z_{22}) and the degree-3 estimate, scaled by the ratio $Z\,(2)\,/Z\,(3)$, which we obtain by evaluating equation (5.12) at both $l = 2$ and $l = 3$. Doing this calculation requires assuming a compensation model. For simplicity, we assume complete isostatic compensation ($C = 1$) and then we solve equation (5.12) for d. Given that (ignoring uncertainties for the moment) $Z_{30} = 3.003 \times 10^{-7}\,\mathrm{m^{-1}}$, and assuming the parameters given in Table 5.1, we obtain $d \approx 29\,\mathrm{km}$. The result is that $\frac{Z(2)}{Z(3)} \approx 0.99$ so that $Z_{30}\left(\frac{Z(2)}{Z(3)}\right) \approx 2.973 \times 10^{-7}\,\mathrm{m^{-1}}$. This scaled degree-3 admittance (green line in Figure 5.3) plots very close to the intersection of the Z_{20} and Z_{22} lines (blue and red lines, respectively). This result thus provides an *a posteriori* check that the assumption of isotropic admittance is appropriate. Table 5.2 lists the gravity and topography coefficients separated into their hydrostatic and non-hydrostatic parts, along with the resulting admittances.

Taking uncertainties into account, agreement between the three estimates occurs at the 1σ level for normalized moments of inertia ($\alpha = \frac{I}{MR^2}$) in the range 0.333–0.338 and admittances in the range $2.4 - 3.6 \times 10^{-7}\,\mathrm{m^{-1}}$ (Figure 5.3). Agreement at the 2σ level occurs in the range $\alpha = 0.330 - 0.340$ and

Table 5.2: Gravity and topography coefficients separated into their hydrostatic and non-hydrostatic components, along with the resulting admittance estimate. A moment of inertia factor of $\alpha = 0.335$ is assumed in computing the hydrostatic gravity and topography.

Coefficient	Observed	Hydrostatic	Non-Hydrostatic	Admittance
C_{20}^g	-5.435×10^{-3}	-5.000×10^{-3}	-0.436×10^{-3}	$Z_{20} = 3.411 \times 10^{-7}\,\mathrm{m}^{-1}$
C_{20}^h	$-3,846\,\mathrm{m}$	$-2,569\,\mathrm{m}$	$-1,277\,\mathrm{m}$	
C_{22}^g	1.550×10^{-3}	1.500×10^{-3}	0.050×10^{-3}	$Z_{22} = 3.421 \times 10^{-7}\,\mathrm{m}^{-1}$
C_{22}^h	$917\,\mathrm{m}$	$771\,\mathrm{m}$	$146\,\mathrm{m}$	
C_{30}^g	0.115×10^{-3}		0.115×10^{-3}	$Z_{30} = 3.003 \times 10^{-7}\,\mathrm{m}^{-1}$
C_{30}^h	$384\,\mathrm{m}$		$384\,\mathrm{m}$	

$Z(2) = 1.8 - 4.2 \times 10^{-7}\,\mathrm{m}^{-1}$. The regions of agreement (blue shaded areas in Figure 5.3) were obtained by performing a Monte Carlo analysis in which each admittance value is calculated 100,000 times with the gravity and topography coefficients being distributed randomly according to their formal uncertainties. The regions in which there is overlap between the resulting 1σ ranges of the three separate admittance estimates (based on the Z_{20}, Z_{22}, and Z_{30} estimates) is considered to be the region of agreement at the 1σ level (dark blue shaded area in Figure 5.3). The same procedure was carried out to determine the region of agreement at the 2σ level (pale blue shaded area in Figure 5.3).

5.4.2 Isostatic Compensation

Admittance is a function of the degree and depth of compensation (e.g., equation (5.14)), with large admittances indicating little compensation or very large compensation depths, and small admittances indicating substantial (or even complete) compensation and/or shallow compensation depths. The observed degree-2 admittance, $Z(2) \approx 3.4 \times 10^{-7}\,\mathrm{m}^{-1}$, is much smaller than the admittance given by equation (5.13) for fully uncompensated (that is, rigidly supported) topography, $\sim 14 \times 10^{-7}\,\mathrm{m}^{-1}$, suggesting that the topog-

raphy is highly compensated (Figure 5.3). If the topography is compensated completely ($C = 1$), then we can use equation (5.12) to estimate the depth of compensation. The observed admittance compares well with the expectation for complete compensation at depths of roughly $20 - 40$ km (dashed lines in Figure 5.3).

5.4.3 Elastic Support

If there is some measure of elastic strength in the lithosphere, then our compensation depth estimates must be altered. If we assume the ice shell has been loaded from the top, we can use equation (5.14) to see how admittance varies with compensation depth (d) and the elastic layer thickness (T). Enceladus is so small that, even a very thin elastic layer provides significant flexural support and leads to large admittances (Figure 5.4a). To produce the admittance we observe, for the case of top loading, the elastic layer must be less than ~ 25 m in thickness. If the topography is supported in part by elastic flexure, the compensation depth must be even shallower than the $20 - 40$ km we estimated for the fully isostatic case.

Conversely, if the topography arises due to buoyant loads emplaced at the base of the ice shell (bottom loading), larger elastic thicknesses require deeper compensation depths in order to be compatible with the observed admittances (Figure 5.4b). This is because bottom loading in the presence of an elastic lithosphere leads to reduced buoyant uplift, leaving the low-density isostatic roots to influence the gravity signal, reducing the admittance. If the ice shell has appreciable elastic strength, and was loaded primarily from below, the compensation depth must be greater than the $20 - 40$ km we estimated for

the fully isostatic case. Not all points in Figure 5.4b are possible, however, because the maximum mantle thickness corresponding to the low end of the admittance range is less than about 60 km (see Figure 5.5a). Consequently, we can rule out elastic thicknesses larger than ~ 300 m.

5.4.4 Internal Structure

The moment of inertia implied by the convergence illustrated in Figure 5.3, $\sim 0.335MR^2$, indicates a substantial degree of differentiation. We approximate Enceladus as a simple two-layer body: a silicate core surrounded by an H_2O mantle, with density somewhere between that of ice and liquid water. Given the observed bulk density constraint, $\bar{\rho} = 1609\,\mathrm{kg/m^3}$, we use equation (5.20) to obtain a mantle thickness of roughly $50 - 65$ km (Figure 5.5a) and a core density around $2250 - 2500\,\mathrm{kg/m^3}$ (Figure 5.5b). The low core density is an indication that the (presumably silicate) core may be substantially hydrated.

5.5 Conclusions

In spite of the limited nature of the gravity observations, we have been able to draw some useful conclusions. The combination of the large non-hydrostatic topography and the modest non-hydrostatic gravity suggests substantial compensation, consistent with lateral thickness variations in an ice shell that is supported isostatically, i.e., "floating" in a subsurface liquid layer. We obtain a self-consistent interior structure model, with an average compensation depth of $20 - 40$ km, when we assume the moment of inertia is $\sim 0.335MR^2$. Given the known bulk density ($1609\,\mathrm{kg/m^3}$), our results are consistent with an Enceladus consisting of a hydrated silicate core of radius $185 - 200$ km and density

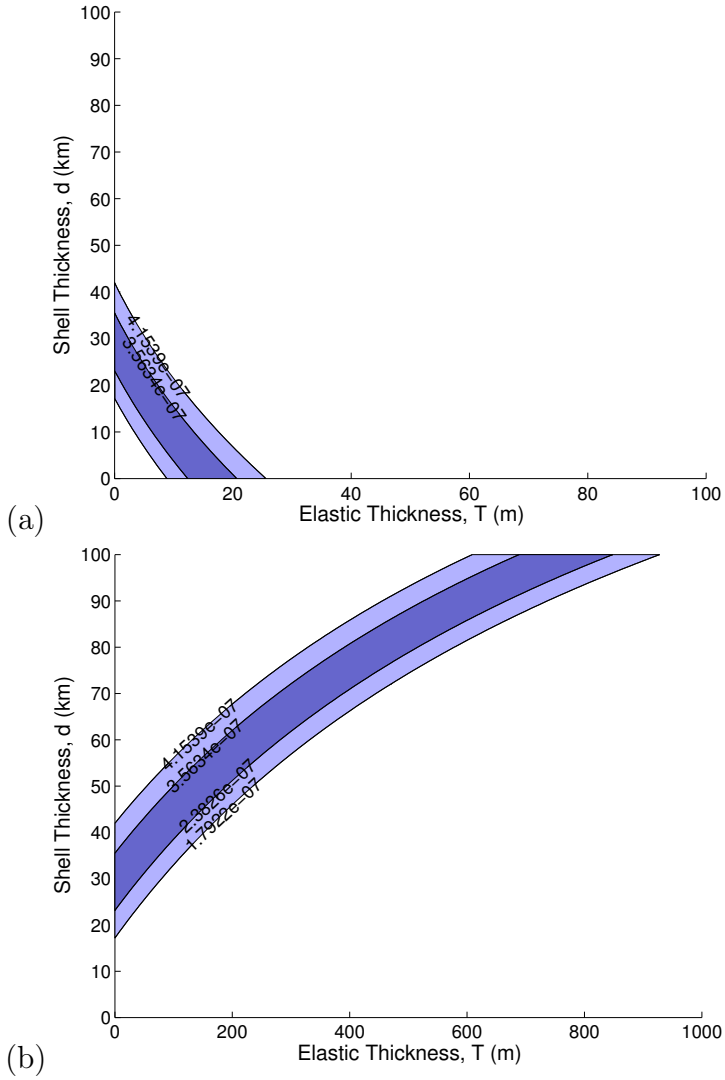

Figure 5.4: Admittance as a function of compensation depth (d) and elastic layer thickness (T) assuming the topography arises from: (a) surfaces loads that deflect the lithosphere downward; or (b) under-plating of the ice shell that deflects the lithosphere upward. The dark blue bands correspond to the admittance estimates within the 1σ region of agreement while the pale blue bands correspond to the 2σ region. Because compensation takes place at the base of the ice shell, compensation depth and shell thickness are equivalent.

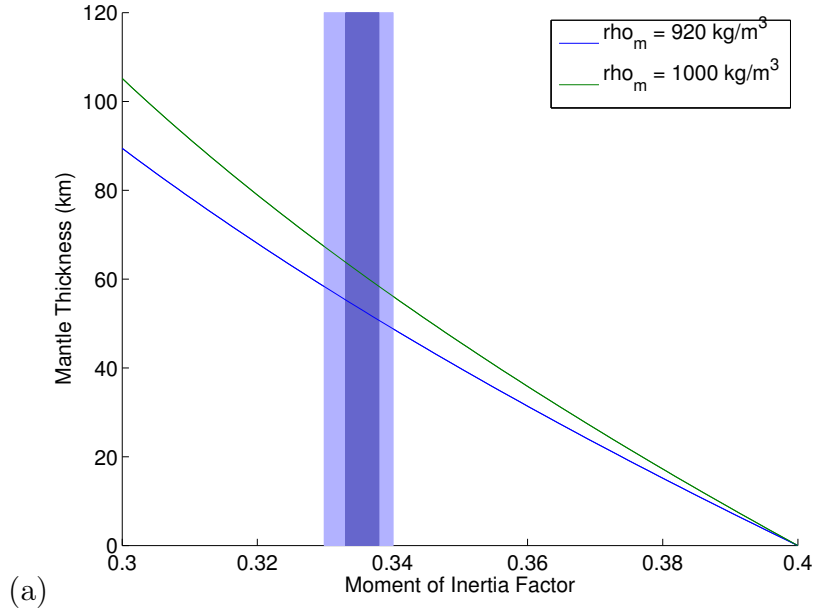

(a)

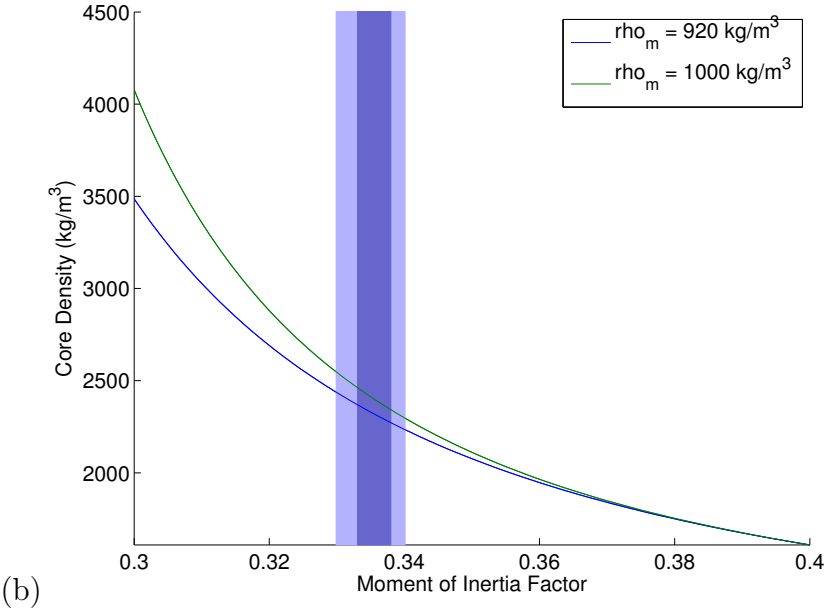

(b)

Figure 5.5: Mantle Thickness (a) and Core Density (b) as a function of Moment of Inertia for two different assumed mantle densities. The dark blue bands illustrate the moment of inertia factor within the 1σ region of agreement while the pale blue bands correspond to the 2σ region (refer to Figure 5.3).

$2250 - 2500\,\mathrm{kg/m^3}$, a subsurface ocean layer with mean thickness $15 - 25\,\mathrm{km}$, and an outer ice shell $20 - 40\,\mathrm{km}$ thick.

Acknowledgements

We thank the *Cassini* radio science team and Luciano Iess for inviting us to work with the newly acquired Enceladus gravity data.

Appendix A

Spherical Harmonics

Because several different conventions are in widespread use, I make my usage and notations explicit here to avoid ambiguity. Much of this Appendix follows *Wieczorek* (2007), although my notation differs slightly.

Any square-integrable function defined over the surface of a sphere, may be represented by a linear combination of spherical harmonic functions as follows

$$F(\theta,\phi) = \sum_{l=0}^{\infty} \sum_{m=0}^{l} \left(C_{lm} \cos m\phi + S_{lm} \sin m\phi\right) P_{lm}(\cos\theta) \qquad \text{(A.1)}$$

where θ is colatitude, ϕ is longitude, $P_{lm}(\cos\theta)$ are the associated Legendre functions of degree l and order m, and where C_{lm} and S_{lm} are the corresponding expansion coefficients. Equation (A.1) is sometimes written more compactly as

$$F(\theta,\phi) = \sum_{l=0}^{\infty} \sum_{m=-l}^{l} f_{lm} Y_{lm}(\theta,\phi) \qquad \text{(A.2)}$$

where f_{lm} are the expansion coefficients, and where $Y_{lm}(\theta,\phi)$ are the real

spherical harmonic functions, defined by

$$Y_{lm}(\theta,\phi) = \begin{cases} P_{lm}(\cos\theta)\cos m\phi & m \geq 0 \\ P_{lm}(\cos\theta)\sin|m|\,\phi & m < 0 \end{cases} \tag{A.3}$$

I will mainly use the former convention, but the latter will be especially convenient for the derivations in Appendix C.

To ensure accurate computations, even across a range of spherical harmonic degrees, it is often necessary to normalize the spherical harmonic functions. When working with normalized spherical harmonics, I write

$$F(\theta,\phi) = \sum_{l=0}^{\infty}\sum_{m=0}^{l}\left(\bar{C}_{lm}\cos m\phi + \bar{S}_{lm}\sin m\phi\right)\bar{P}_{lm}(\cos\theta) \tag{A.4}$$

where $\bar{P}_{lm}(\cos\theta)$ are the normalized associated Legendre functions and where $\bar{C}_{lm}$ and $\bar{S}_{lm}$ are the corresponding normalized expansion coefficients. The more compact form is written

$$F(\theta,\phi) = \sum_{l=0}^{\infty}\sum_{m=-l}^{l}\bar{f}_{lm}\bar{Y}_{lm}(\theta,\phi) \tag{A.5}$$

where $\bar{f}_{lm}$ are the normalized expansion coefficients, and where $\bar{Y}_{lm}(\theta,\phi)$ are the normalized real spherical harmonic functions, defined by

$$\bar{Y}_{lm}(\theta,\phi) = \begin{cases} \bar{P}_{lm}(\cos\theta)\cos m\phi & m \geq 0 \\ \bar{P}_{lm}(\cos\theta)\sin|m|\,\phi & m < 0 \end{cases} \tag{A.6}$$

Several different normalizations are in use, but I will discuss only two here.

The first is the Schmidt semi-normalization, widely used in geomagnetism

$$\bar{P}_{lm}(\mu) = \sqrt{(2-\delta_{m0})\frac{(l-m)!}{(l+m)!}} P_{lm}(\mu) \tag{A.7}$$

where δ_{0m} is the Kronecker delta. The second is what I may call the geodesy 4π-normalization, or full normalization, which I use when working with topography and gravity fields

$$\bar{P}_{lm}(\mu) = \sqrt{(2-\delta_{m0})(2l+1)\frac{(l-m)!}{(l+m)!}} P_{lm}(\mu) \tag{A.8}$$

The unnormalized associated Legendre functions are given by

$$P_{lm}(\mu) = \left(1-\mu^2\right)^{\frac{m}{2}} \frac{d^m}{d\mu^m} P_l(\mu) \tag{A.9}$$

where $P_l(\mu)$ is the degree-l Legendre polynomial, and is given by

$$P_l(\mu) = \frac{1}{2^l l!}\frac{d^l}{d\mu^l}\left(\mu^2-1\right)^l \tag{A.10}$$

Note that caution is required when using the Matlab function `legendre()` since its conventions differ from the above, and so appropriate corrections must be made (carefully). For instance, the Matlab definitions also include the Condon-Shortly phase factor, $(-1)^m$. When requesting normalized associated Legendre functions from Matlab, this is not an issue because the phase factor appears both in the definition of P_{lm} and in the normalization, such that they cancel. For the Schmidt normalization, the normalized associated Legendre functions obtained from Matlab are the same as in equation (A.7), but for the

geodesy 4π normalization, the Matlab result gives

$$\left(\bar{P}_{lm}(\mu)\right)_{\text{Matlab}} = \sqrt{\left(l+\frac{1}{2}\right)\frac{(l-m)!}{(l+m)!}}P_{lm}(\mu) \tag{A.11}$$

Hence, we need the following adjustment when using the full (or geodesy 4π) normalization

$$\bar{P}_{lm}(\mu) = \sqrt{2(2-\delta_{m0})}\left(\bar{P}_{lm}(\mu)\right)_{\text{Matlab}} \tag{A.12}$$

When using unnormalized associated Legendre functions from Matlab, the following correction is required to account for the Condon-Shortly phase factor

$$P_{lm}(\mu) = (-1)^m \left(P_{lm}(\mu)\right)_{\text{Matlab}} \tag{A.13}$$

Finally, if the function $F(\theta,\phi)$ is known over θ and ϕ, the fully normalized expansion coefficients can be obtained via

$$\bar{f}_{lm} = \frac{1}{4\pi}\int_{\theta}\int_{\phi} F(\theta,\phi)\,\bar{Y}_{lm}(\theta,\phi)\sin\theta d\theta d\phi \tag{A.14}$$

Appendix B

Magnetic Potential and Source Models

B.1 Magnetic Scalar Potential and Vector Magnetic Fields

Magnetic fields originating within a planetary body, and measured externally, can be specified by a magnetic scalar potential, V, which satisfies Laplace's equation

$$\nabla^2 V = 0$$

and can be represented as a linear combination of spherical harmonic functions as

$$V(r,\theta,\phi) = a\sum_{l=0}^{\infty}\sum_{m=0}^{l}\left(\frac{a}{r}\right)^{l+1}\left(C_{lm}\cos m\phi + S_{lm}\sin m\phi\right)P_{lm}(\cos\theta)$$

where r is the radius at which the potential is to be expressed, θ is colatitude, ϕ is longitude, $P_{lm}(\cos\theta)$ are the associated Legendre functions of degree l and order m, C_{lm} and S_{lm} are the corresponding expansion coefficients representing the magnetic scalar potential at a reference radius a.

The vector magnetic field (also called magnetic flux density or magnetic induction, with units of Teslas) outside the reference radius, a, is given by the negative gradient of the scalar magnetic potential

$$\mathbf{B} = -\nabla V$$

In spherical coordinates, the magnetic field vector components are therefore given by

$$B_r = -\frac{\partial V}{\partial r} = \sum_{l=0}^{\infty}\sum_{m=0}^{l}(l+1)\left(\frac{a}{r}\right)^{l+2}\left(C_{lm}\cos m\phi + S_{lm}\sin m\phi\right)P_{lm}(\cos\theta)$$

$$B_\theta = -\frac{\partial V}{r\partial\theta} = -\sum_{l=0}^{\infty}\sum_{m=0}^{l}\left(\frac{a}{r}\right)^{l+2}\left(C_{lm}\cos m\phi + S_{lm}\sin m\phi\right)\frac{\partial P_{lm}(\cos\theta)}{\partial\theta}$$

$$B_\phi = -\frac{\partial V}{r\sin\theta\partial\phi} = \frac{1}{\sin\theta}\sum_{l=0}^{\infty}\sum_{m=0}^{l}m\left(\frac{a}{r}\right)^{l+2}\left(C_{lm}\sin m\phi - S_{lm}\cos m\phi\right)P_{lm}(\cos\theta)$$

Note that these expressions differ slightly from those of *Connerney* (2007) due, I believe, to typographical errors in the latter.

B.2 Source Models

Here, we calculate the locations of the maxima and minima in the horizontal magnetic field profiles due to both vertically and horizontally magnetized

sources, as discussed in Chapter 2. We first consider the single dipole sources illustrated in Figure 2.1 and then repeat the calculations for the line sources discussed in section 2.4.

B.2.1 Single Dipole Source

If we take the horizontal and vertical positions in the top panels of Figure 2.1 to be the x and z coordinates, respectively, and if the magnetic dipoles are each located at the origin with magnetic moment $\mathbf{m}$ (with units of Am^2), then the resulting magnetic field, $\mathbf{B}$ (with units of Teslas or $\frac{\mathrm{N}}{\mathrm{Am}}$), at a position, $\mathbf{r} = x\hat{\mathbf{i}} + y\hat{\mathbf{j}} + z\hat{\mathbf{k}}$, is given by

$$\mathbf{B} = \frac{\mu_0}{4\pi}\left(3(\mathbf{m}\cdot\mathbf{r})\mathbf{r} - \mathbf{m}r^2\right)\frac{1}{r^5} \tag{B.1}$$

Equation (B.1) is adapted from *Blakely* (1995), pp. 75. Here, we employ SI units with μ_0 being the magnetic permeability of free space (which has a value of $4\pi \times 10^{-7}\ \frac{\mathrm{N}}{\mathrm{A}^2}$). For points in the x-z plane, the horizontal component of the magnetic field (B_h) is identical to the magnitude of the x-component (B_x) since, by symmetry, magnetic field lines cannot cross the x-z plane (i.e., cannot have a y-component).

Considering the case of the vertically oriented dipole ($\mathbf{m} = \begin{bmatrix} 0 & 0 & m \end{bmatrix}^T$), the horizontal component of the magnetic field becomes

$$B_h = |B_x| = \frac{\mu_0}{4\pi}\left(\frac{3mzx}{(x^2+z^2)^{\frac{5}{2}}}\right) \tag{B.2}$$

Equation (B.2) demonstrates that field lines directly over a vertically oriented dipole are vertical at any altitude because $B_h = 0$ when $x = 0$ (this is

also evident in Figure 2.1a). Differentiating equation (B.2) with respect to x and setting the result to zero yields the positions of the peaks in the horizontal field strength profile

$$x_{B_h \max} = \pm \frac{1}{2} z \tag{B.3}$$

This means that the separation between peaks ($2x$) is equal to the altitude above the source (z), which is evident in Figure 2.1c.

Considering the case of the horizontally oriented dipole ($\mathbf{m} = \begin{bmatrix} m & 0 & 0 \end{bmatrix}^T$), and still being restricted to points in the x-z plane, the vertical (z) component of the magnetic field becomes

$$B_v = |B_z| = \frac{\mu_0}{4\pi} \left(\frac{3mxz}{(x^2 + z^2)^{\frac{5}{2}}} \right) \tag{B.4}$$

Equation (B.4) demonstrates that field lines directly over a horizontally oriented dipole are horizontal at any altitude because $Bz = 0$ when $x = 0$ (Figure 2.1b). Again, starting from equation (B.1), and considering only points in the x-z plane, the horizontal component of the magnetic field due to a horizontally oriented dipole that is aligned with the x-axis becomes

$$B_h = |B_x| = \frac{\mu_0}{4\pi} \left(\frac{m\,(2x^2 - z^2)}{(x^2 + z^2)^{\frac{5}{2}}} \right) \tag{B.5}$$

Setting equation (B.5) to zero shows that the horizontal field strength drops to zero when

$$x_{B_h = 0} = \pm \frac{1}{\sqrt{2}} z \tag{B.6}$$

Hence, the cusps in the horizontal magnetic field profile are laterally displaced from the source by a distance of $1/\sqrt{2}$ times the altitude above the

source (this is evident in Figure 2.1d).

B.2.2 Linear Source

Instead of a single dipole, consider a source that is a linear structure such as a long, thin, uniformly magnetized cylinder. If this linear source is infinitely long and coincident with the y-axis, and the magnetization per unit length is $\mathbf{m}'$, then the magnetic field is given by

$$\mathbf{B} = \frac{\mu_0}{4\pi}\left(4(\mathbf{m}' \cdot \mathbf{r})\mathbf{r} - 2\mathbf{m}' r^2\right)\frac{1}{r^4} \tag{B.7}$$

Equation (B.7) is adapted from *Blakely* (1995), pp. 96. Again, considering only points in the x-z plane, the horizontal component of the magnetic field due to the vertically magnetized line source becomes

$$B_h = |B_x| = \frac{\mu_0}{4\pi}\left(\frac{4m'zx}{(x^2+z^2)^2}\right) \tag{B.8}$$

As with the dipole case, field lines directly over a vertically magnetized line source are vertical at any altitude. Differentiating equation (B.8) with respect to x and setting the result to zero yields the positions of the peaks in the horizontal field profile

$$x_{B_h \max} = \pm\frac{1}{\sqrt{3}}z \tag{B.9}$$

Considering the case of a horizontally magnetized line source, the vertical (z) component of the magnetic field becomes

$$B_v = |B_z| = \frac{\mu_0}{4\pi}\left(\frac{4m'xz}{(x^2+z^2)^2}\right) \tag{B.10}$$

Hence, field lines directly over a horizontally magnetized linear source are horizontal at any altitude. Again, starting from equation (B.7), and considering only points in the x-z plane, the horizontal component of the magnetic field due to a linear source coincident with the y-axis and magnetization parallel to the x-axis becomes

$$B_h = |B_x| = \frac{\mu_0}{4\pi}\left(\frac{2m'\left(x^2 - z^2\right)}{\left(x^2 + z^2\right)^2}\right) \tag{B.11}$$

Setting equation (B.11) to zero shows that the horizontal field strength drops to zero when

$$x_{B_h=0} = \pm z \tag{B.12}$$

Hence, the cusps in the horizontal magnetic field profile are laterally displaced from the line source by a distance equal to the altitude above the source.

Appendix C

Gravitational Potential and Figures of Equilibrium

C.1 Gravitational Potential

If U is the work per unit mass done by an object's gravitational field, then the acceleration due to gravity is given by

$$\mathbf{g} = -\nabla U \tag{C.1}$$

where U is the gravitational potential, or Newtonian potential, and is given by

$$U(\mathbf{r}) = -G \int_V \frac{\rho(\mathbf{r}')}{|\mathbf{r} - \mathbf{r}'|} dV' \tag{C.2}$$

where the integral is performed over the object's entire volume V, the density at position $\mathbf{r}'$ is $\rho(\mathbf{r}')$, and where G is the universal gravitational constant.

Everywhere outside the object, the gravitational potential satisfies Laplace's

equation (*Kaula*, 2000)

$$\nabla^2 U(r) = 0 \tag{C.3}$$

and the potential can be expressed as a linear combination of spherical harmonic functions as

$$U(r,\theta,\phi) = -\frac{GM}{r}\sum_{l=0}^{\infty}\sum_{m=-l}^{l}\left(\frac{R_0}{r}\right)^l C^{\mathrm{g}}_{lm} Y_{lm}(\theta,\phi) \tag{C.4}$$

where r is the radius at which the potential is to be expressed, θ is colatitude, ϕ is longitude, and C^{g}_{lm} are the degree-l and order-m spherical harmonic expansion coefficients representing the dimensionless gravitational potential at a reference radius R_0 (see Appendix A).

Following equation (C.1), to get the radial part of the gravitational acceleration, we differentiate with respect to r, obtaining

$$g_r(r,\theta,\phi) = \frac{GM}{r^2}\sum_{l=0}^{\infty}\sum_{m=-l}^{l}\left(\frac{R_0}{r}\right)^l (l+1)\, C^{\mathrm{g}}_{lm} Y_{lm}(\theta,\phi) \tag{C.5}$$

where we have followed the usual convention of making gravity positive downward.

C.2 Tidal and Rotational Deforming Potentials

C.2.1 Tidal Deforming Potential

A satellite in synchronous orbit around its parent body will experience permanent tidal distortion due to the variation in potential caused by the nearby tide-raising body. Following from *Murray and Dermott* (1999), the potential,

V, at a point, P, is

$$V = -\frac{GM}{d}$$

where M is the mass of the tide-raising body and d is the distance between P and the center of the tide-raising body. If the center-to-center distance between the two bodies is a, the body's radius is R, and P makes an angle ψ with the centerline between the two bodies, then (by the cosine rule)

$$d^2 = a^2 + R^2 - 2aR\cos\psi$$

which can be written as

$$d = a\left(1 + \left(\frac{R}{a}\right)^2 - 2\left(\frac{R}{a}\right)\cos\psi\right)^{1/2}$$

Expanding this, we obtain

$$V^{\text{tid}} = -\frac{GM}{a}\left[1 + \left(\frac{R}{a}\right)\cos\psi + \left(\frac{R}{a}\right)^2 \frac{1}{2}\left(3\cos^2\psi - 1\right) + \ldots\right] \qquad \text{(C.6)}$$

The first term in (C.6) is a constant and therefore does not contribute to tidal distortion. The second term in (C.6) relates to circular motion of the satellite around its parent body and therefore does not contribute to tidal distortion. The tide-raising part of the potential begins with the third term. Neglecting higher order terms, the tide-raising part of the potential is

$$V^{\text{tid}} = -\frac{GMR^2}{a^3}\frac{1}{2}\left(3\cos^2\psi - 1\right) = -\frac{GMR^2}{a^3}P_2(\cos\psi)$$

If the tide-raising body is much more massive than the synchronous satellite

$(M \gg m)$, and the angular frequency is ω, then $\omega^2 = GM/a^3$. Hence

$$V^{\rm tid} = -\omega^2 R^2 P_2(\cos\psi)$$

Assuming the tidal axis is perpendicular to the spin axis and converting to coordinates of colatitude, θ, and longitude, ϕ, we have $\cos\psi = \cos\phi\sin\theta$, so that

$$V^{\rm tid} = -\omega^2 R^2 P_2(\cos\phi\sin\theta) \tag{C.7}$$

This can be re-written in terms of the (non-normalized) spherical harmonic functions, Y_{20} and Y_{22}. First, we look at $P_2(\cos\phi\sin\theta)$

$$P_2\left(\cos\phi\sin\theta\right) = \frac{1}{2}\left(3\cos^2\phi\sin^2\theta - 1\right)$$

which, after some manipulation, can be written

$$P_2\left(\cos\phi\sin\theta\right) = \frac{3}{4}\cos 2\phi\left(1-\cos^2\theta\right) - \frac{1}{4}\left(3\cos^2\theta - 1\right)$$

But because $Y_{20} = P_2\left(\cos\theta\right) = \frac{1}{2}\left(3\cos^2\theta - 1\right)$ and $Y_{22} = P_{22}\left(\cos\theta\right)\cos\left(2\phi\right) = 3\left(1-\cos^2\theta\right)\cos\left(2\phi\right)$, we have

$$P_2\left(\cos\phi\sin\theta\right) = \frac{1}{4}Y_{22} - \frac{1}{2}Y_{20}$$

Hence

$$V^{\rm tid} = \omega^2 R^2\left[\frac{1}{2}Y_{20} - \frac{1}{4}Y_{22}\right] \tag{C.8}$$

C.2.2 Rotational Deforming Potential

For a body rotating with angular velocity ω, the centrifugal acceleration is $\mathbf{a}^{\rm cf} = \omega^2\mathbf{x}$, where $\mathbf{x} = R\sin\theta$ is a vector pointed outward from, and perpendicular to, the axis of rotation and reaching the surface at colatitude θ. Since $\mathbf{a}^{\rm cf} = -\nabla V^{\rm cf}$, the centrifugal potential is thus

$$V^{\rm cf} = -\frac{1}{2}\omega^2 R^2 \sin^2\theta$$

Because $P_2(\cos\theta) = \frac{1}{2}(3\cos^2\theta - 1)$, we can write this as

$$V^{\rm cf} = \frac{1}{3}\omega^2 R^2 \left[P_2(\cos\theta) - 1\right] \tag{C.9}$$

Since the last term in (C.9) is a constant, it does not contribute to rotational distortion. The relevant part of the rotational potential is thus

$$V^{\rm rot} = \frac{1}{3}\omega^2 R^2 P_2(\cos\theta) \tag{C.10}$$

This can be re-written simply in terms of $Y_{20} = P_2(\cos\theta)$ as

$$V^{\rm rot} = \frac{1}{3}\omega^2 R^2 Y_{20} \tag{C.11}$$

C.2.3 Combined Deforming Potential

A body subjected to both tidal and rotation distortion will experience a total disturbing potential $V^{\rm tot} = V^{\rm rot} + V^{\rm tid}$. Combining (C.7) and (C.10), we have

$$V^{\rm tot} = \omega^2 R^2 \left[\frac{1}{3}P_2(\cos\theta) - P_2(\cos\phi\sin\theta)\right]$$

Or, in terms of spherical harmonic functions, we combine (C.8) and (C.11) to get

$$V^{\text{tot}} = \omega^2 R^2 \left[\frac{1}{3} Y_{20} + \frac{1}{2} Y_{20} - \frac{1}{4} Y_{22} \right]$$

where the first term is the result of rotation and the second and third terms are due to the permanent tide. This simplifies to

$$V^{\text{tot}} = \omega^2 R^2 \left[\frac{5}{6} Y_{20} - \frac{1}{4} Y_{22} \right] \tag{C.12}$$

C.3 Equilibrium Figures and Potentials

A body subjected to a deforming potential, V, will deform to some degree, depending on the body's rigidity and internal mass distribution, attributes reflected in the Love number h. In determining the equilibrium shape of a relaxed hydrostatic body, we are concerned with the fluid Love number h_f, and the deformed shape is given by (*Monk and MacDonald*, 1960)

$$H^{\text{hyd}}(\theta, \phi) = R - \frac{h_f}{g} V \tag{C.13}$$

The change in shape will result in a further change in the gravitational potential, $k_f V$, which defines the Love number k_f, so that the non-central parts of the body's hydrostatic gravity are given by

$$U^{\text{hyd}}(\theta, \phi) = k_f V \tag{C.14}$$

where, for a fluid body, $h_f = 1 + k_f$.

For a perfectly fluid body, we can relate the fluid Love number, h_{2f}, to

the body's normalized moment of inertia using the Radau-Darwin equation (*Murray and Dermott*, 1999), which can be written

$$\frac{I}{MR^2} = \frac{2}{3}\left(1 - \frac{2}{5}\sqrt{\frac{5}{h_{2f}} - 1}\right) \tag{C.15}$$

C.3.1 Rotational Deformation

C.3.1.1 Hydrostatic Shape

A planet with no permanent tidal elongation will have an equilibrium shape determined by rotational distortion. Here we treat the disturbing potential as a degree-2 harmonic and so we are concerned with the degree-2 fluid Love number h_{2f}. Substituting equation (C.11) into equation (C.13), we obtain

$$H^{\mathrm{hyd}}(\theta, \phi) = R - \frac{\omega^2 R^2}{g} h_{2f}\left[\frac{1}{3} Y_{20}\right] \tag{C.16}$$

If the hydrostatic topography is represented in spherical harmonics as

$$H^{\mathrm{hyd}}(\theta, \phi) = \sum_{l=0}^{\infty} \sum_{m=-l}^{l} C_{lm}^{\mathrm{h,hyd}} Y_{lm}(\theta, \phi)$$

then the non-zero coefficients for the hydrostatic shape are

$$C_{00}^{\mathrm{h,hyd}} = R \tag{C.17}$$

$$C_{20}^{\mathrm{h,hyd}} = -\frac{1}{3}\frac{R^2\omega^2}{g} h_{2f} \tag{C.18}$$

Note that the ratio between the centrifugal and gravitational accelerations

at the surface of the body is often written

$$q = \frac{R\omega^2}{g} \tag{C.19}$$

so we can also write

$$C_{20}^{\mathrm{h,hyd}} = -\frac{1}{3} R q h_{2f}$$

The above hydrostatic shape (predicted based on rotational distortion, accounting for the fluid Love number h_{2f}) is often defined by the semi-axes of an ellipsoid ($a = b > c$). This is done simply by evaluating the above hydrostatic shape at three locations: at the spin pole, when $\theta = 0$ (gives the magnitude of the c-axis), and at two points on the equator: when $\theta = \frac{\pi}{2}$, $\phi = \frac{\pi}{2}$ (b-axis), and when $\theta = \frac{\pi}{2}$, $\phi = 0$ (a-axis). The resulting semi-axes are

$$a = b = R\left(1 + \frac{1}{6} q h_{2f}\right)$$

$$c = R\left(1 - \frac{1}{3} q h_{2f}\right)$$

From which we have

$$\frac{a - c}{R} = \frac{1}{2} q h_{2f}$$

C.3.1.2 Hydrostatic Gravity

Substituting equation (C.11) into equation (C.14), we obtain

$$U^{\mathrm{hyd}}(\theta, \phi) = \omega^2 R^2 k_{2f} \left[\frac{1}{3} Y_{20}\right] \tag{C.20}$$

If the hydrostatic gravitational potential is represented (at the reference

radius) in spherical harmonics as

$$U^{\text{hyd}}(\theta,\phi) = -\frac{GM}{R}\sum_{l=0}^{\infty}\sum_{m=-l}^{l} C_{lm}^{\text{g,hyd}} Y_{lm}(\theta,\phi)$$

where $C_{lm}^{\text{g,hyd}}$ are the dimensionless gravitational potential coefficients, then, noting that the surface gravity is $g = \frac{GM}{R^2}$, the only non-zero coefficient for the hydrostatic gravitational potential is

$$C_{20}^{\text{g,hyd}} = -\frac{1}{3}\frac{\omega^2 R}{g} k_{2f} \tag{C.21}$$

Again using $q = \frac{R\omega^2}{g}$, and noting that the negative (2,0) coefficient is also called J_2, so we can write

$$J_2 = -C_{20}^{\text{g,hyd}} = \frac{1}{3} q k_{2f}$$

C.3.1.3 Geoid

The geoid is the equipotential surface corresponding to the average potential at a reference radius: $U_{ref} = GM/R$. The shape of the geoid is a function of the actual mass distribution within the body (captured in the potential coefficients, C_{lm}^{g}, and including rotational deformation) plus the effects of rotation on the equipotential surface.

For a body with no permanent tide, the geoid is given by

$$H^{\text{geoid}}(\theta,\phi) = R + R\sum_{l=2}^{\infty}\sum_{m=-l}^{l} C_{lm}^{\text{g}} Y_{lm} - \frac{1}{3}\frac{R^2\omega^2}{g} Y_{20} \tag{C.22}$$

Hence, the spherical harmonic coefficients for the geoid are equal to the

potential coefficients multiplied by R, with the exception of the (0,0) and (2,0) coefficients, which are

$$C_{00}^{\mathrm{h,geoid}} = R$$

$$C_{20}^{\mathrm{h,geoid}} = R\left(C_{20}^{\mathrm{g}} - \frac{1}{3}\frac{R\omega^2}{g}\right)$$

C.3.1.4 Reference Ellipsoid

The C_{20} term, which arises primarily from rotational distortion, typically dominates the geoid. To highlight those parts of the geoid that are caused by mass anomalies rather than rotational distortion, the geoid is sometimes shown with respect to a reference ellipsoid. In general, an ellipsoid is triaxial with semi-axes $a > b > c$, but for a body subjected only to rotational distortion, $a = b > c$ (see section C.3.2.4 for the reference ellipsoid corresponding to a synchronous satellite, which experiences both rotational and tidal distortion). The reference ellipsoid is sometimes expressed as a degree-2 shape that matches the geoid in its C_{20} term alone. That is

$$H^{\mathrm{ref}}(\theta,\phi) = R\left(1 + \left(C_{20}^{\mathrm{g}} - \frac{1}{3}\frac{\omega^2 R}{g}\right)Y_{20}\right) \tag{C.23}$$

which is evaluated at three locations to get the semi-axes of the "equivalent" ellipsoid

$$a = H^{\mathrm{ref}}\left(\frac{\pi}{2}, 0\right) = R\left(1 - \frac{1}{2}C_{20}^{\mathrm{g}} + \frac{1}{6}\frac{\omega^2 R}{g}\right)$$

$$b = H^{\mathrm{ref}}\left(\frac{\pi}{2}, \frac{\pi}{2}\right) = R\left(1 - \frac{1}{2}C_{20}^{\mathrm{g}} + \frac{1}{6}\frac{\omega^2 R}{g}\right)$$

$$c = H^{\mathrm{ref}}(0,0) = R\left(1 + C_{20}^{\mathrm{g}} - \frac{1}{3}\frac{\omega^2 R}{g}\right)$$

The ellipsoid's surface is given by

$$H^{\text{ref}}(\theta,\phi) = \frac{abc}{\sqrt{(bc\sin\theta\cos\phi)^2 + (ca\sin\theta\sin\phi)^2 + (ab\cos\theta)^2}} \tag{C.24}$$

Strictly speaking, an ellipsoid has power at all even harmonics, meaning that the reference ellipsoid given by equation (C.24) is not identical to the purely degree-2 shape described by equation (C.23), except at the pole and at the equator. Because we are usually working with spherical harmonics, equation (C.23) is easier to use and so the geoid with respect to the "reference ellipsoid" is often obtained by subtracting equation (C.23) from equation (C.22). That is

$$H^{\text{geoid-ref}}(\theta,\phi) = R\sum_{l=2}^{\infty}\sum_{m=-l}^{l} C_{lm}^{\text{g}} Y_{lm} - RC_{20}^{\text{g}} Y_{20} \tag{C.25}$$

Hence, the spherical harmonic coefficients for the geoid with respect to the "reference ellipsoid" are equal to the dimensionless gravitational potential coefficients multiplied by R, with the exception of the (2,0) coefficient, which is zero.

C.3.2 Tidal/Rotational Deformation

C.3.2.1 Hydrostatic Shape

A synchronous, or tidally-locked, satellite will have an equilibrium shape determined by both tidal and rotational distortion. Since we are considering only a degree-2 disturbing potential, we are concerned with the degree-2 fluid Love number h_{2f}. Substituting equation (C.12) into equation (C.13), we obtain

$$H^{\text{hyd}}(\theta,\phi) = R + \frac{\omega^2 R^2}{g} h_{2f}\left[\frac{1}{4}Y_{22} - \frac{5}{6}Y_{20}\right] \tag{C.26}$$

If the hydrostatic topography is represented in spherical harmonics as

$$H^{\mathrm{hyd}}(\theta,\phi)=\sum_{l=0}^{\infty}\sum_{m=-l}^{l}C_{lm}^{\mathrm{h,hyd}}Y_{lm}\left(\theta,\phi\right)$$

then the non-zero coefficients for the hydrostatic shape are

$$C_{00}^{\mathrm{h,hyd}}=R \tag{C.27}$$

$$C_{20}^{\mathrm{h,hyd}}=-\frac{5}{6}\frac{R^2\omega^2}{g}h_{2f} \tag{C.28}$$

$$C_{22}^{\mathrm{h,hyd}}=\frac{1}{4}\frac{R^2\omega^2}{g}h_{2f} \tag{C.29}$$

The ratio between the degree-2 coefficients is thus

$$\frac{C_{20}^{\mathrm{h,hyd}}}{C_{22}^{\mathrm{h,hyd}}}=-\frac{10}{3}$$

Note also that, because $Y_{20}=P_2\left(\cos\theta\right)=\frac{1}{2}\left(3\cos^2\theta-1\right)$ and $Y_{22}=P_{22}\left(\cos\theta\right)\cos\left(2\phi\right)=3\left(1-\cos^2\theta\right)\cos\left(2\phi\right)$, and using $q=\frac{R\omega^2}{g}$, equation (C.26) is sometimes written

$$H^{\mathrm{hyd}}\left(\theta,\phi\right)=R+Rqh_{2f}\left[\frac{1}{2}\left(3\cos^2\phi+1\right)\left(1-\cos^2\theta\right)-\frac{5}{6}\right]$$

The above hydrostatic shape (predicted based on tidal and rotational distortion, accounting for the fluid Love number h_{2f}) is often defined by the semi-axes of a triaxial ellipsoid (a, b, c). This is done simply by evaluating the above hydrostatic shape at three locations: at the spin pole, when $\theta=0$ (gives the magnitude of the c-axis), and at two points on the equator: when $\theta=\frac{\pi}{2}$,

$\phi = \frac{\pi}{2}$ (b-axis), and when $\theta = \frac{\pi}{2}$, $\phi = 0$ (a-axis). The resulting semi-axes are

$$a = R\left(1 + \frac{7}{6}qh_{2f}\right)$$

$$b = R\left(1 - \frac{1}{3}qh_{2f}\right)$$

$$c = R\left(1 - \frac{5}{6}qh_{2f}\right)$$

From which we have

$$\frac{a-c}{R} = 2qh_{2f}$$

and

$$\frac{a-c}{b-c} = 4$$

C.3.2.2 Hydrostatic Gravity

Substituting equation (C.12) into equation (C.14), we obtain

$$U^{\text{hyd}}(\theta,\phi) = \omega^2 R^2 k_{2f}\left[\frac{5}{6}Y_{20} - \frac{1}{4}Y_{22}\right] \tag{C.30}$$

If the hydrostatic gravitational potential is represented (at the reference radius) in spherical harmonics as

$$U^{\text{hyd}}(\theta,\phi) = -\frac{GM}{R}\sum_{l=0}^{\infty}\sum_{m=-l}^{l} C_{lm}^{\text{g,hyd}} Y_{lm}(\theta,\phi)$$

where $C_{lm}^{\text{g,hyd}}$ are the dimensionless gravitational potential coefficients, then, noting that the surface gravity is $g = \frac{GM}{R^2}$, the non-zero coefficients for the

hydrostatic gravitational potential are

$$C_{20}^{\mathrm{g,hyd}} = -\frac{5}{6}\frac{\omega^2 R}{g}k_{2f} \tag{C.31}$$

$$C_{22}^{\mathrm{g,hyd}} = \frac{1}{4}\frac{\omega^2 R}{g}k_{2f} \tag{C.32}$$

Note that, using the shorthand $q = \frac{R\omega^2}{g}$, we can also write

$$J_2 = -C_{20}^{\mathrm{g,hyd}} = \frac{5}{6}qk_{2f}$$

The ratio between the degree-2 coefficients is

$$\frac{C_{20}^{\mathrm{g,hyd}}}{C_{22}^{\mathrm{g,hyd}}} = -\frac{10}{3}$$

C.3.2.3 Geoid

The geoid is the equipotential surface corresponding to the average potential at a reference radius: $U_{ref} = GM/R$. The shape of the geoid is a function of the actual mass distribution within the body (captured in the potential coefficients, and including tidal and rotational deformation) plus the effects of tides and rotation on the equipotential surface.

The synchronous satellite geoid is given by

$$H^{\mathrm{geoid}}(\theta,\phi) = R + R\sum_{l=2}^{\infty}\sum_{m=-l}^{l} C_{lm}^{\mathrm{g}}Y_{lm} - \frac{5}{6}\frac{R^2\omega^2}{g}Y_{20} + \frac{1}{4}\frac{R^2\omega^2}{g}Y_{22} \tag{C.33}$$

Hence, the spherical harmonic coefficients for the geoid are equal to the dimensionless gravitational potential coefficients multiplied by R, with the

exception of the (0,0), (2,0) and (2,2) coefficients, which are

$$C_{00}^{\mathrm{h,geoid}} = R$$

$$C_{20}^{\mathrm{h,geoid}} = R\left(C_{20}^{\mathrm{g}} - \frac{5}{6}\frac{R\omega^2}{g}\right)$$

$$C_{22}^{\mathrm{h,geoid}} = R\left(C_{22}^{\mathrm{g}} + \frac{1}{4}\frac{R\omega^2}{g}\right)$$

C.3.2.4 Reference Ellipsoid

The C_{20} and C_{22} terms, which arise primarily from tidal and rotational distortion, typically dominate the geoid. To highlight those parts of the geoid that are caused by mass anomalies rather than tidal/rotational distortion, the geoid is sometimes shown with respect to a reference ellipsoid. The reference ellipsoid is a triaxial ellipsoid with semi-axes $a > b > c$. It is sometimes expressed as a degree-2 shape that matches the geoid in its C_{20} and C_{22} terms only. That is

$$H^{\mathrm{ref}}(\theta,\phi) = R\left(1 + \left(C_{20}^{\mathrm{g}} - \frac{5}{6}\frac{\omega^2 R}{g}\right)Y_{20} + \left(C_{22}^{\mathrm{g}} + \frac{1}{4}\frac{\omega^2 R}{g}\right)Y_{22}\right) \qquad \text{(C.34)}$$

which is evaluated at three locations to get the semi-axes of the "equivalent" ellipsoid

$$a = H^{\mathrm{ref}}\left(\frac{\pi}{2}, 0\right) = R\left(1 - \frac{1}{2}C_{20}^{\mathrm{g}} + 3C_{22}^{\mathrm{g}} + \frac{7}{6}\frac{\omega^2 R}{g}\right)$$

$$b = H^{\mathrm{ref}}\left(\frac{\pi}{2}, \frac{\pi}{2}\right) = R\left(1 - \frac{1}{2}C_{20}^{\mathrm{g}} - 3C_{22}^{\mathrm{g}} - \frac{1}{3}\frac{\omega^2 R}{g}\right)$$

$$c = H^{\mathrm{ref}}(0,0) = R\left(1 + C_{20}^{\mathrm{g}} - \frac{5}{6}\frac{\omega^2 R}{g}\right)$$

The ellipsoid's surface is given by

$$H^{\text{ref}}(\theta,\phi) = \frac{abc}{\sqrt{(bc\sin\theta\cos\phi)^2 + (ca\sin\theta\sin\phi)^2 + (ab\cos\theta)^2}} \tag{C.35}$$

Strictly speaking, an ellipsoid has power at all even harmonics, meaning that the reference ellipsoid given by equation (C.35) is not identical to the purely degree-2 shape described by equation (C.34), except along the three Cartesian axes (where a, b, c are defined). Because we are usually working with spherical harmonics, equation (C.34) is easier to use and so the geoid with respect to the "reference ellipsoid" is often obtained by subtracting equation (C.34) from equation (C.33). That is

$$H^{\text{geoid-ref}}(\theta,\phi) = R\sum_{l=2}^{\infty}\sum_{m=-l}^{l} C_{lm}^{\text{g}} Y_{lm} - RC_{20}^{\text{g}} Y_{20} - RC_{22}^{\text{g}} Y_{22} \tag{C.36}$$

Hence, the spherical harmonic coefficients for the geoid with respect to the "reference ellipsoid" are equal to the dimensionless gravitational potential coefficients multiplied by R, with the exception of the (2,0) and (2,2) coefficients, which are zero.

Bibliography

Adams, J. B., and T. B. McCord (1971), Alteration of Lunar Optical Properties: Age and Composition Effects, *Science*, *171*(3971), 567–571.

Archinal, B. B. A., M. R. Rosiek, R. L. Kirk, and B. L. Redding (2006), The Unified Lunar Control Network 2005, *Tech. rep.*, USGS, Flagstaff, AZ.

Béghin, C., C. Sotin, and M. Hamelin (2010), Titan's native ocean revealed beneath some 45km of ice by a Schumann-like resonance, *Comptes Rendus Geosci.*, *342*(6), 425–433, doi:10.1016/j.crte.2010.03.003.

Belleguic, V., P. Lognonné, and M. Wieczorek (2005), Constraints on the Martian lithosphere from gravity and topography data, *J. Geophys. Res.*, *110*(E11), E11,005, doi:10.1029/2005JE002437.

Bills, B. G., and F. Nimmo (2011), Rotational dynamics and internal structure of Titan, *Icarus*, *214*(1), 351–355, doi:10.1016/j.icarus.2011.04.028.

Black, B. A., J. T. Perron, D. M. Burr, and S. A. Drummond (2012), Estimating erosional exhumation on Titan from drainage network morphology, *J. Geophys. Res.*, *117*(E8), 1–17, doi:10.1029/2012JE004085.

Blakely, R. J. (1995), *Potential Theory in Gravity and Magnetic Applications*, Cambridge University Press.

Blewett, D. T., B. R. Hawke, N. C. Richmond, and C. G. Hughes (2007), A magnetic anomaly associated with an albedo feature near Airy crater in the lunar nearside highlands, *Geophys. Res. Lett.*, *34*(24), 1–6, doi:10.1029/2007GL031670.

Blewett, D. T., E. I. Coman, B. R. Hawke, J. J. Gillis-Davis, M. E. Purucker, and C. G. Hughes (2011), Lunar swirls: Examining crustal magnetic anomalies and space weathering trends, *J. Geophys. Res.*, *116*(E02002), doi:10.1029/2010JE003656.

Běhounková, M., G. Tobie, G. Choblet, and O. Čadek (2012), Tidally-induced melting events as the origin of south-pole activity on Enceladus, *Icarus*, *219*(2), 655–664, doi:10.1016/j.icarus.2012.03.024.

Choukroun, M., and C. Sotin (2012), Is Titan's shape caused by its meteorology and carbon cycle?, *Geophys. Res. Lett.*, *39*(4), 1–5, doi:10.1029/2011GL050747.

Clark, R. N. (2009), Detection of adsorbed water and hydroxyl on the Moon., *Science*, *326*(5952), 562–4, doi:10.1126/science.1178105.

Cohen, B. A., P. O. Hayne, D. A. Paige, and B. T. Greenhagen (2014), Lunar Flashlight: Mapping Lunar Surface Volatiles Using a Cubesat, in *Annu. Meet. Lunar Explor. Anal. Gr.*, vol. 35812, p. 3031, doi:10.1126/science.1187726.

Coleman, P. J., B. R. Lichtenstein, C. T. Russell, L. R. Sharp, and G. Schubert (1972), Magnetic fields near the moon, in *Third Lunar Sci. Conf.*, pp. 2271–2286.

Connerney, J. E. (1999), Magnetic Lineations in the Ancient Crust of Mars, *Science*, *284*(5415), 794–798, doi:10.1126/science.284.5415.794.

Connerney, J. E. P. (2007), Planetary Magnetism, in *Treatise Geophys.*, chap. 10.07, pp. 243–280.

Dawkins, R. (1976), *The Selfish Gene*, Oxford Univ. Press, Oxford, U.K.

Domingue, D. L., C. R. Chapman, R. M. Killen, T. H. Zurbuchen, J. A. Gilbert, M. Sarantos, M. Benna, J. A. Slavin, D. Schriver, P. M. Trávníček, T. M. Orlando, A. L. Sprague, D. T. Blewett, J. J. Gillis-Davis, W. C. Feldman, D. J. Lawrence, G. C. Ho, D. S. Ebel, L. R. Nittler, F. Vilas, C. M. Pieters, S. C. Solomon, C. L. Johnson, R. M. Winslow, J. Helbert, P. N. Peplowski, S. Z. Weider, N. Mouawad, N. R. Izenberg, and W. E. McClintock (2014), Mercury's Weather-Beaten Surface: Understanding Mercury in the Context of Lunar and Asteroidal Space Weathering Studies, *Space Sci. Rev.*, *181*(1-4), 121–214, doi:10.1007/s11214-014-0039-5.

Dwyer, C. A., D. J. Stevenson, and F. Nimmo (2011), A long-lived lunar dynamo driven by continuous mechanical stirring, *Nature*, *479*(7372), 212–214, doi:10.1038/nature10564.

Dyal, P., C. W. Parkin, and C. P. Sonett (1970), Apollo 12 Magnetometer: Measurement of a Steady Magnetic Field on the Surface of the Moon, *Science*, *169*(3947), 762–764.

Dyment, J., and J. Arkani-Hamed (1998), Equivalent source magnetic dipoles revisited, *Geophys. Res. Lett.*, *25*(11), 2003–2006, doi:10.1029/98GL51331.

Eliason, E., C. Isbell, E. Lee, T. Becker, L. Gaddis, A. McEwen, and M. Robinson (1999), The Clementine UVVIS Global Lunar Mosaic, *Tech. rep.*, U.S. Geological Survey / Planetary Data System.

Garrick-Bethell, I., B. P. Weiss, D. L. Shuster, and J. Buz (2009), Early lunar magnetism., *Science*, *323*(5912), 356–9, doi:10.1126/science.1166804.

Garrick-Bethell, I., J. W. Head, and C. M. Pieters (2011), Spectral properties, magnetic fields, and dust transport at lunar swirls, *Icarus*, *212*(2), 480–492, doi:10.1016/j.icarus.2010.11.036.

Goldberg, D. E. (1989), *Genetic Algorithms in Search, Optimization and Machine Learning*, Addison-Wesley, Reading, Mass.

Goldsby, D. L., and D. L. Kohlstedt (2001), Superplastic deformation of ice: Experimental observations, *J. Geophys. Res.*, *106*(B6), 11,017–11,030, doi:10.1029/2000JB900336.

Grasset, O., C. Sotin, and F. Deschamps (2000), On the internal structure and dynamics of Titan, *Planet. Space Sci.*, *48*(7-8), 617–636, doi:10.1016/S0032-0633(00)00039-8.

Halekas, J. S., D. L. Mitchell, R. P. Lin, S. Frey, L. L. Hood, M. H. Acuña, and A. B. Binder (2001), Mapping of crustal magnetic anomalies on the lunar near side by the Lunar Prospector electron reflectometer, *J. Geophys. Res.*, *106*(E11), 841–852.

Hapke, B. (2001), Space weathering from Mercury to the asteroid belt, *J. Geophys. Res.*, *106*(E5), 10,039–10,073.

Harnett, E. M., and R. M. Winglee (2003), 2.5-D fluid simulations of the solar wind interacting with multiple dipoles on the surface of the Moon, *J. Geophys. Res.*, *108*(A2), doi:10.1029/2002JA009617.

Hemingway, D., and I. Garrick-Bethell (2012), Magnetic field direction and lunar swirl morphology: Insights from Airy and Reiner Gamma, *J. Geophys. Res.*, *117*(E10012), doi:10.1029/2012JE004165.

Hemingway, D., F. Nimmo, H. Zebker, and L. Iess (2013), A rigid and weathered ice shell on Titan, *Nature*, *500*(7464), 550–552, doi:10.1038/nature12400.

Hemingway, D. J., I. Garrick-Bethell, and M. A. Kreslavsky (2015), Latitudinal Variation in Spectral Properties of the Lunar Maria and Implications for Space Weathering, *Icarus*, doi:10.1016/j.icarus.2015.08.004.

Hendrix, A. R., K. D. Retherford, G. Randall Gladstone, D. M. Hurley, P. D. Feldman, A. F. Egan, D. E. Kaufmann, P. F. Miles, J. W. Parker, D. Horvath, P. M. Rojas, M. H. Versteeg, M. W. Davis, T. K. Greathouse, J. Mukherjee, A. J. Steffl, W. R. Pryor, and S. A. Stern (2012), The lunar far-UV albedo: Indicator of hydration and weathering, *J. Geophys. Res. E Planets*, *117*(12), 1–8, doi:10.1029/2012JE004252.

Holland, J. (1992), *Adaptation in Natural and Artificial Systems: An Introductory Analysis with Applications to Biology, Control, and Artificial Intelligence*, MIT Press, Cambridge, Mass.

Hood, L., and G. Schubert (1980), Lunar Magnetic Anomalies and Surface Optical Properties, *Science*, *208*, 49–51, doi:10.1126/science.307.5713.1191.

Hood, L., and C. Williams (1989), The lunar swirls-Distribution and possible origins, in *Lunar Planet. Sci. Conf. Proc.*, vol. 19, pp. 99–113.

Hood, L., C. Russell, and P. Coleman (1981), Contour maps of lunar remanent magnetic fields, *J. Geophys. Res.*, *86*, 1055–1069.

Hood, L. L. (2011), Central magnetic anomalies of Nectarian-aged lunar impact basins: Probable evidence for an early core dynamo, *Icarus*, *211*(2), 1109–1128, doi:10.1016/j.icarus.2010.08.012.

Hood, L. L., and N. A. Artemieva (2008), Antipodal effects of lunar basin-forming impacts: Initial 3D simulations and comparisons with observations, *Icarus*, *193*(2), 485–502, doi:10.1016/j.icarus.2007.08.023.

Hood, L. L., P. Coleman, and D. Wilhelms (1979), The Moon: Sources of the Crustal Magnetic Anomalies, *Science*, *204*(4388), 53–57.

Hood, L. L., A. Zakharian, J. Halekas, D. Mitchell, R. Lin, M. Acuña, and A. Binder (2001), Initial mapping and interpretation of lunar crustal magnetic anomalies using Lunar Prospector magnetometer data, *J. Geophys. Res.*, *106*(E11), 27,825–27,839, doi:10.1029/2000JE001366.

Iess, L., N. J. Rappaport, R. A. Jacobson, P. Racioppa, D. J. Stevenson, P. Tortora, J. W. Armstrong, and S. W. Asmar (2010), Gravity field, shape, and moment of inertia of Titan., *Science*, *327*(5971), 1367–9, doi:10.1126/science.1182583.

Iess, L., R. A. Jacobson, M. Ducci, D. J. Stevenson, J. I. Lunine, J. W. Armstrong, S. W. Asmar, P. Racioppa, N. J. Rappaport, and P. Tortora (2012), The Tides of Titan, *Science*, *337*, 457–459, doi:10.1126/science.1219631.

Iess, L., D. J. Stevenson, M. Parisi, D. Hemingway, R. A. Jacobson, J. I. Lunine, F. Nimmo, J. W. Armstrong, S. W. Asmar, M. Ducci, and P. Tortora (2014), The Gravity Field and Interior Structure of Enceladus, *Science*, *344*(6179), 78–80, doi:10.1126/science.1250551.

Jeffreys, H. (1976), *The Earth: its origin, history, and physical constitution*, 6th ed., 535–566 pp., Cambridge University Press, New York.

Kargel, J. S. (1998), Physical Chemistry of Ices in the Outer Solar System, in *Sol. Syst. Ices*, edited by B. Schmitt, C. de Bergh, and M. Festou, pp. 3–32, Kluwer Academic Publishers, Dordrecht.

Kaula, W. M. (2000), *Theory of Satellite Geodesy: Applications of Satellites to Geodesy*, Dover.

Klinger, J. (1980), Influence of a Phase Transition of Ice on the Heat and Mass Balance of Comets, *Science*, *209*(4453), 271–272.

Kramer, G. Y., S. Besse, D. Dhingra, J. Nettles, R. Klima, I. Garrick-Bethell, R. N. Clark, J.-P. Combe, J. W. Head, L. a. Taylor, C. M. Pieters, J. Boardman, and T. B. McCord (2011), M3 spectral analysis of lunar swirls and the link between optical maturation and surface hydroxyl formation at magnetic anomalies, *J. Geophys. Res.*, *116*(E00G18), doi:10.1029/2010JE003729.

Kraus, H. (1967), *Thin Elastic Shells*, Wiley, New York.

Kreslavsky, M. A., J. W. Head, G. A. Neumann, M. A. Rosenburg, O. Aharonson, D. E. Smith, and M. T. Zuber (2013), Lunar topographic roughness maps from Lunar Orbiter Laser Altimeter (LOLA) data: Scale dependence and correlation with geologic features and units, *Icarus*, *226*(1), 52–66, doi:10.1016/j.icarus.2013.04.027.

Kurata, M., H. Tsunakawa, Y. Saito, H. Shibuya, M. Matsushima, and H. Shimizu (2005), Mini-magnetosphere over the Reiner Gamma magnetic anomaly region on the Moon, *Geophys. Res. Lett.*, *32*(24), 5–8, doi:10.1029/2005GL024097.

Lawrence, D. J., W. C. Feldman, R. C. Elphic, R. C. Little, T. H. Prettyman, S. Maurice, P. G. Lucey, and A. B. Binder (2002), Iron abundances on the lunar surface as measured by the Lunar Prospector gamma-ray and neutron spectrometers, *J. Geophys. Res.*, *107*(E12), 5130, doi:10.1029/2001JE001530.

Le Bars, M., M. A. Wieczorek, O. Karatekin, D. Cébron, and M. Laneuville (2011), An impact-driven dynamo for the early Moon, *Nature*, *479*(7372), 215–218, doi:10.1038/nature10565.

Le Feuvre, M., and M. A. Wieczorek (2011), Nonuniform cratering of the Moon and a revised crater chronology of the inner Solar System, *Icarus*, *214*(1), 1–20, doi:10.1016/j.icarus.2011.03.010.

Lin, R. P. (1979), Constraints on the origins of lunar magnetism from electron reflection measurements of surface magnetic fields, *Phys. Earth Planet. Inter.*, *20*, 271–280.

Lin, R. P., D. L. Mitchell, D. W. Curtis, K. A. Anderson, C. W. Carlson, J. McFadden, M. H. Acuña, L. L. Hood, and A. Binder (1998), Lunar Surface Magnetic Fields and Their Interaction with the Solar Wind: Results from Lunar Prospector, *Science*, *281*(5382), 1480–1484, doi:10.1126/science.281.5382.1480.

Lopes, R., K. Mitchell, E. Stofan, J. Lunine, R. Lorenz, F. Paganelli, R. Kirk, C. Wood, S. Wall, L. Robshaw, a.D. Fortes, C. Neish, J. Radebaugh, E. Reffet, S. Ostro, C. Elachi, M. Allison, Y. Anderson, R. Boehmer, G. Boubin, P. Callahan, P. Encrenaz, E. Flamini, G. Francescetti, Y. Gim, G. Hamilton, S. Hensley, M. Janssen, W. Johnson, K. Kelleher, D. Muhleman, G. Ori, R. Orosei, G. Picardi, F. Posa, L. Roth, R. Seu, S. Shaffer, L. Soderblom, B. Stiles, S. Vetrella, R. West, L. Wye, and H. Zebker (2007), Cryovolcanic features on Titan's surface as revealed by the Cassini Titan Radar Mapper, *Icarus*, *186*(2), 395–412, doi:10.1016/j.icarus.2006.09.006.

Lucchitta, B. K. (1978), Geologic Map of the North Side of the Moon.

Lucey, P. G., D. T. Blewett, G. J. Taylor, and B. R. Hawke (2000a), Imaging of lunar surface maturity, *J. Geophys. Res.*, *105*(E8), 20,377–20,386.

Lucey, P. G., D. T. Blewett, and B. L. Jolliff (2000b), Lunar iron and titanium abundance algorithms based on final processing of Clementine ultraviolet-visible images, *J. Geophys. Res.*, *105*(E8), 20,297–20,305.

Lucey, P. G., G. A. Neumann, M. A. Riner, E. Mazarico, D. E. Smith, M. T. Zuber, D. A. Paige, D. B. J. Bussey, J. T. S. Cahill, A. McGovern, P. Isaacson, L. M. Corley, M. H. Torrence, H. J. Melosh, J. W. Head, and E. Song (2014), The global albedo of the Moon at 1064 nm, *J. Geophys. Res. Planets*, *119*, 1665–1679, doi:10.1002/2013JE004592.Received.

McCord, T. B., L. A. Taylor, J.-P. Combe, G. Kramer, C. M. Pieters, J. M. Sunshine, and R. N. Clark (2011), Sources and physical processes responsible for OH/H2O in the lunar soil as revealed by the Moon Mineralogy Mapper (M3), *J. Geophys. Res.*, *116*, E00G05, doi:10.1029/2010JE003711.

McGovern, P. J., S. C. Solomon, D. E. Smith, M. T. Zuber, M. Simons, M. A. Wieczorek, R. J. Phillips, G. A. Neumann, O. Aharonson, and J. W. Head (2002), Localized gravity/topography admittance and correlation spectra on Mars: Implications for regional and global evolution, *J. Geophys. Res.*, *107*(E12), 1–25, doi:10.1029/2002JE001854.

McKenzie, D. (1994), The Relationship between Topography and Gravity on Earth and Venus, *Icarus*, *112*, 55–88.

McKinnon, W. B. (2013), The shape of Enceladus as explained by an irregular core: Implications for gravity, libration, and survival of its subsurface ocean, *J. Geophys. Res. Planets*, *118*, doi:10.1002/jgre.20122.

Mckinnon, W. B. (2015), Effect of Enceladus's rapid synchronous spin on interpretation of Cassini gravity, *Geophys. Res. Lett.*, *42*, doi:10.1002/2015GL063384.

Mitchell, D., J. Halekas, R. Lin, S. Frey, L. Hood, M. Acuña, and a. Binder (2008), Global mapping of lunar crustal magnetic fields by Lunar Prospector, *Icarus*, *194*(2), 401–409, doi:10.1016/j.icarus.2007.10.027.

Mitri, G., and A. P. Showman (2008), A model for the temperature-dependence of tidal dissipation in convective plumes on icy satellites: Implications for Europa and Enceladus, *Icarus*, *195*(2), 758–764, doi:10.1016/j.icarus.2008.01.010.

Monk, W., and G. MacDonald (1960), *The Rotation of the Earth*, Cambridge University Press.

Moore, J. M., and R. T. Pappalardo (2011), Titan: An exogenic world?, *Icarus*, *212*(2), 790–806, doi:10.1016/j.icarus.2011.01.019.

Moore, J. M., A. D. Howard, and P. M. Schenk (2013), Bedrock denudation on Titan: estimates of vertical extent and lateral debris dispersion, in *44th Lunar Planet. Sci. Conf.*, p. 1763.

Moore, J. M., A. D. Howard, and A. M. Morgan (2014), The landscape of Titan as witness to its climate evolution, *J. Geophys. Res. Planets*, *119*, 2060–2077, doi:10.1002/2014JE004608.

Moore, W. B., and G. Schubert (2003), The tidal response of Ganymede and Callisto with and without liquid water oceans, *Icarus*, *166*(1), 223–226, doi:10.1016/j.icarus.2003.07.001.

Murray, C. D., and S. Dermott (1999), *Solar System Dynamics*, Cambridge University Press.

Mustard, J. F., L. Li, and G. He (1998), Nonlinear spectral mixture modeling of lunar multispectral data: Implications for lateral transport, *J. Geophys. Res.*, *103*(E8), 19,419–19,425.

Neish, C., D. Blewett, D. Bussey, S. Lawrence, M. Mechtley, and B. Thomson (2011), The surficial nature of lunar swirls as revealed by the Mini-RF instrument, *Icarus*, *215*(1), 186–196, doi:10.1016/j.icarus.2011.06.037.

Neish, C., R. Kirk, R. Lorenz, V. Bray, P. Schenk, B. Stiles, E. Turtle, K. Mitchell, and A. G. Hayes (2013), Crater topography on Titan: Implications for landscape evolution, *Icarus*, *223*(1), 82–90, doi:10.1016/j.icarus.2012.11.030.

Ness, N. F., K. W. Behannon, C. S. Scearce, and S. C. Cantarano (1967), Early Results from the Magnetic Field Experiment on Lunar Explorer 35, *J. Geophys. Res.*, *72*(23), 5769–5778.

Nicholas, J. B., M. E. Purucker, and T. J. Sabaka (2007), Age spot or youthful marking: Origin of Reiner Gamma, *Geophys. Res. Lett.*, *34*(2), 1–4, doi:10.1029/2006GL027794.

Nimmo, F. (2004), Non-Newtonian topographic relaxation on Europa, *Icarus*, *168*(1), 205–208, doi:10.1016/j.icarus.2003.11.022.

Nimmo, F., and B. Bills (2010), Shell thickness variations and the long-wavelength topography of Titan, *Icarus*, *208*(2), 896–904, doi:10.1016/j.icarus.2010.02.020.

Nimmo, F., R. T. Pappalardo, and B. Giese (2002), Effective elastic thickness and heat flux estimates on Ganymede, *Geophys. Res. Lett.*, *29*(7), 1158.

Nimmo, F., J. R. Spencer, R. T. Pappalardo, and M. E. Mullen (2007), Shear heating as the origin of the plumes and heat flux on Enceladus., *Nature*, *447*(7142), 289–91, doi:10.1038/nature05783.

Nimmo, F., B. G. Bills, and P. C. Thomas (2011), Geophysical implications of the long-wavelength topography of the Saturnian satellites, *J. Geophys. Res.*, *116*(E11), E11,001, doi:10.1029/2011JE003835.

Noble, S. K., C. M. Pieters, and L. P. Keller (2007), An experimental approach to understanding the optical effects of space weathering, *Icarus*, *192*(2), 629–642, doi:10.1016/j.icarus.2007.07.021.

Nozette, S., P. Rustan, L. P. Pleasance, D. M. Horan, P. Regeon, E. M. Shoemaker, P. D. Spudis, C. H. Acton, D. N. Baker, J. E. Blamont, B. J. Buratti, M. P. Corson, M. E. Davies, T. C. Duxbury, E. M. Eliason, B. M. Jakosky,

J. F. Kordas, I. T. Lewis, C. L. Lichtenberg, P. G. Lucey, E. Malaret, M. A. Massie, J. H. Resnick, C. J. Rollins, H. S. Park, A. S. Mcewen, R. E. Priest, C. M. Pieters, R. A. Reisse, M. S. Robinson, R. A. Simpson, D. E. Smith, T. C. Sorenson, R. W. Vorder Breugge, and M. T. Zuber (1994), The Clementine Mission to the Moon: Scientific Overview, *Science*, *266*(5192), 1835–1839.

Pariso, J. E., and H. P. Johnson (1991), Alteration Processes at Deep Sea Drilling Project/Ocean Drilling Program Hole 504B at the Costa Rica Rift: Implications for Magnetization of Oceanic Crust, *J. Geophys. Res.*, *96*(B7), 11,703–11,722.

Parker, R. L. (2003), Ideal bodies for Mars magnetics, *J. Geophys. Res.*, *108*(E1), 5006, doi:10.1029/2001JE001760.

Patterson, D. B., K. A. Farley, and M. D. Norman (1999), He-4 as a tracer of continental dust: A 1.9 million year record of aeolian flux to the west equatorial Pacific Ocean, *Geochim. Cosmochim. Acta*, *63*(5), 615–625.

Pieters, C. M. (1978), Mare basalt types on the front side of the moon: A summary of spectral reflectance data, in *9th Lunar Planet. Sci. Conf.*, pp. 2825–2849.

Pieters, C. M., E. M. Fischer, O. Rode, and A. Basu (1993), Optical Effects of Space Weathering: The Role of the Finest Fraction, *J. Geophys. Res.*, *98*(E11), 20,817–20,824.

Pieters, C. M., L. A. Taylor, S. K. Noble, L. P. Keller, B. Hapke, R. V. Morris, C. C. Allen, D. S. McKay, and S. Wentworth (2000), Space weathering on airless bodies: Resolving a mystery with lunar samples, *Meteorit. Planet. Sci.*, *35*, 1101–1107.

Pieters, C. M., J. N. Goswami, R. N. Clark, M. Annadurai, J. Boardman, B. Buratti, J.-P. Combe, M. D. Dyar, R. Green, J. W. Head, C. Hibbitts, M. Hicks, P. Isaacson, R. Klima, G. Kramer, S. Kumar, E. Livo, S. Lundeen, E. Malaret, T. McCord, J. Mustard, J. Nettles, N. Petro, C. Runyon, M. Staid, J. Sunshine, L. A. Taylor, S. Tompkins, and P. Varanasi (2009), Character and spatial distribution of OH/H2O on the surface of the Moon seen by M3 on Chandrayaan-1, *Science*, *326*(5952), 568–72, doi: 10.1126/science.1178658.

Pieters, C. M., E. Ammannito, D. T. Blewett, B. W. Denevi, M. C. De Sanctis, M. J. Gaffey, L. Le Corre, J.-Y. Li, S. Marchi, T. B. McCord, L. A. McFadden, D. W. Mittlefehldt, A. Nathues, E. Palmer, V. Reddy, C. A. Raymond,

and C. T. Russell (2012), Distinctive space weathering on Vesta from regolith mixing processes., *Nature*, *491*(7422), 79–82, doi:10.1038/nature11534.

Pieters, C. M., D. P. Moriarty, and Ian Garrick-Bethell (2014), Atypical regolith processes hold the key to enigmatic lunar swirls, in *45th Lunar Planet. Sci. Conf.*

Pinet, P. C., V. V. Shevchenko, S. D. Chevrel, Y. Daydou, and C. Rosemberg (2000), Local and regional lunar regolith characteristics at Reiner Gamma Formation: Optical and spectroscopic properties from Clementine and Earth-based data, *J. Geophys. Res.*, *105*(E4), 9457–9475.

Porco, C. C., P. Helfenstein, P. C. Thomas, A. P. Ingersoll, J. Wisdom, R. West, G. Neukum, T. Denk, R. Wagner, T. Roatsch, S. Kieffer, E. Turtle, A. McEwen, T. V. Johnson, J. Rathbun, J. Veverka, D. Wilson, J. Perry, J. Spitale, A. Brahic, J. A. Burns, A. D. Delgenio, L. Dones, C. D. Murray, and S. Squyres (2006), Cassini observes the active south pole of Enceladus., *Science*, *311*(5766), 1393–1401, doi:10.1126/science.1123013.

Prettyman, T. H., J. J. Hagerty, R. C. Elphic, W. C. Feldman, D. J. Lawrence, G. W. McKinney, and D. T. Vaniman (2006), Elemental composition of the lunar surface: Analysis of gamma ray spectroscopy data from Lunar Prospector, *J. Geophys. Res.*, *111*(E12007), doi:10.1029/2005JE002656.

Purucker, M. (2008), A global model of the internal magnetic field of the Moon based on Lunar Prospector magnetometer observations, *Icarus*, *197*(1), 19–23, doi:10.1016/j.icarus.2008.03.016.

Purucker, M. E., and J. B. Nicholas (2010), Global spherical harmonic models of the internal magnetic field of the Moon based on sequential and coestimation approaches, *J. Geophys. Res.*, *115*(E12), 1–14, doi:10.1029/2010JE003650.

Purucker, M. E., T. J. Sabaka, and R. A. Langel (1996), Conjugate gradient analysis: A new tool for studying satellite magnetic data sets, *Geophys. Res. Lett.*, *23*(5), 507–510.

Richards, M. A., and B. H. Hager (1984), Geoid anomalies in a dynamic Earth, *J. Geophys. Res.*, *89*(B7), 5987, doi:10.1029/JB089iB07p05987.

Richmond, N. C., L. L. Hood, J. Halekas, D. Mitchell, R. Lin, M. Acuña, and A. B. Binder (2003), Correlation of a strong lunar magnetic anomaly with a high-albedo region of the Descartes mountains, *Geophys. Res. Lett.*, *30*(7), 1395, doi:10.1029/2003GL016938.

Richmond, N. C., L. Hood, D. Mitchell, R. Lin, M. Acuña, and A. Binder (2005), Correlations between magnetic anomalies and surface geology antipodal to lunar impact basins, *J. Geophys. Res.*, *110*(E5), 1–11, doi: 10.1029/2005JE002405.

Roberts, J. H., and F. Nimmo (2008), Tidal heating and the long-term stability of a subsurface ocean on Enceladus, *Icarus*, *194*(2), 675–689, doi:10.1016/j.icarus.2007.11.010.

Sasaki, S., K. Nakamura, Y. Hamabe, E. Kurahashi, and T. Hiroi (2001), Production of iron nanoparticles by laser irradiation in a simulation of lunar-like space weathering., *Nature*, *410*(6828), 555–7, doi:10.1038/35069013.

Schultz, P. H., and L. J. Srnka (1980), Cometary Collisions on the Moon and Mercury, in *Lunar Planet. Sci. Conf. 11th*, pp. 1009–1011.

Shea, E. K., B. P. Weiss, W. S. Cassata, D. L. Shuster, S. M. Tikoo, J. Gattacceca, T. L. Grove, and M. D. Fuller (2012), A long-lived lunar core dynamo, *Science*, *335*(6067), 453–6, doi:10.1126/science.1215359.

Shibuya, H., H. Tsunakawa, F. Takahashi, H. Shimizu, M. Matsushima, and K. M.-l. Team (2010), Near surface magnetic field mapping over the swirls in the SPA region using Kaguya LMAG data, in *Eur. Planet. Sci. Congr.*, vol. 5.

Smith, D. E., M. T. Zuber, G. A. Neumann, F. G. Lemoine, E. Mazarico, M. H. Torrence, J. F. McGarry, D. D. Rowlands, J. W. Head, T. H. Duxbury, O. Aharonson, P. G. Lucey, M. S. Robinson, O. S. Barnouin, J. F. Cavanaugh, X. Sun, P. Liiva, D.-d. Mao, J. C. Smith, and A. E. Bartels (2010), Initial observations from the Lunar Orbiter Laser Altimeter (LOLA), *Geophys. Res. Lett.*, *37*(18), 1–6, doi:10.1029/2010GL043751.

Spencer, J. R., and F. Nimmo (2013), Enceladus: An Active Ice World in the Saturn System, *Annu. Rev. Earth Planet. Sci.*, *41*(1), 693–717, doi: 10.1146/annurev-earth-050212-124025.

Spitale, J. N., and C. C. Porco (2007), Association of the jets of Enceladus with the warmest regions on its south-polar fractures., *Nature*, *449*(7163), 695–7, doi:10.1038/nature06217.

Staid, M. I., and C. M. Pieters (2000), Integrated Spectral Analysis of Mare Soils and Craters: Applications to Eastern Nearside Basalts, *Icarus*, *145*, 122–139, doi:10.1006/icar.1999.6319.

Starukhina, L. V., and Y. G. Shkuratov (2004), Swirls on the Moon and Mercury: meteoroid swarm encounters as a formation mechanism, *Icarus*, *167*(1), 136–147, doi:10.1016/j.icarus.2003.08.022.

Stiles, B. W., S. Hensley, Y. Gim, D. M. Bates, R. L. Kirk, A. Hayes, J. Radebaugh, R. D. Lorenz, K. L. Mitchell, P. S. Callahan, H. Zebker, W. T. Johnson, S. D. Wall, J. I. Lunine, C. A. Wood, M. Janssen, F. Pelletier, R. D. West, and C. Veeramacheneni (2009), Determining Titan surface topography from Cassini SAR data, *Icarus*, *202*(2), 584–598, doi:10.1016/j.icarus.2009.03.032.

Sunshine, J. M., T. L. Farnham, L. M. Feaga, O. Groussin, F. Merlin, R. E. Milliken, and M. F. A'Hearn (2009), Temporal and spatial variability of lunar hydration as observed by the Deep Impact spacecraft., *Science*, *326*(5952), 565–8, doi:10.1126/science.1179788.

Thomas, P., J. Burns, P. Helfenstein, S. Squyres, J. Veverka, C. Porco, E. Turtle, A. Mcewen, T. Denk, and B. Giese (2007), Shapes of the saturnian icy satellites and their significance, *Icarus*, *190*(2), 573–584, doi:10.1016/j.icarus.2007.03.012.

Tobie, G., O. Grasset, J. I. Lunine, A. Mocquet, and C. Sotin (2005), Titan's internal structure inferred from a coupled thermal-orbital model, *Icarus*, *175*(2), 496–502, doi:10.1016/j.icarus.2004.12.007.

Tobie, G., J. I. Lunine, and C. Sotin (2006), Episodic outgassing as the origin of atmospheric methane on Titan., *Nature*, *440*(7080), 61–4, doi:10.1038/nature04497.

Tricarico, P. (2014), Multi-Layer Hydrostatic Equilibrium of Planets and Synchronous Moons: Theory and Application To Ceres and To Solar System Moons, *Astrophys. J.*, *782*(2), 99, doi:10.1088/0004-637X/782/2/99.

Turcotte, D. L., R. J. Willemann, W. F. Haxby, and J. Norberry (1981), Role of Membrane Stresses in the Support of Planetary Topography, *J. Geophys. Res.*, *86*(1), 3951–3959.

Vernazza, P., R. P. Binzel, A. Rossi, M. Fulchignoni, and M. Birlan (2009), Solar wind as the origin of rapid reddening of asteroid surfaces, *Nature*, *458*(7241), 993–5, doi:10.1038/nature07956.

Von Frese, R. R. B., W. J. Hinze, and L. W. Braile (1981), Spherical Earth Gravity and Magnetic Anomaly Analysis by Equivalent Point Source Inversion, *Earth Planet. Sci. Lett.*, *53*, 69–83.

Werner, S. C., and S. Medvedev (2010), The Lunar rayed-crater population - Characteristics of the spatial distribution and ray retention, *Earth Planet. Sci. Lett.*, *295*(1-2), 147–158, doi:10.1016/j.epsl.2010.03.036.

Wieczorek, M. A. (2007), Gravity and Topography of the Terrestrial Planets, in *Treatise Geophys.*, vol. 10, chap. 10.05, pp. 165–206, doi:10.1016/B978-044452748-6/00156-5.

Wieczorek, M. A., B. P. Weiss, and S. T. Stewart (2012), An Impactor Origin for Lunar Magnetic Anomalies, *Science*, *335*(6073), 1212–1215, doi:10.1126/science.1214773.

Wilcox, B. B., P. G. Lucey, and J. J. Gillis (2005), Mapping iron in the lunar mare: An improved approach, *J. Geophys. Res.*, *110*(E11001), doi:10.1029/2005JE002512.

Yokota, Y., T. Matsunaga, M. Ohtake, J. Haruyama, R. Nakamura, S. Yamamoto, Y. Ogawa, T. Morota, C. Honda, K. Saiki, K. Nagasawa, K. Kitazato, S. Sasaki, A. Iwasaki, H. Demura, N. Hirata, T. Hiroi, R. Honda, Y. Iijima, and H. Mizutani (2011), Lunar photometric properties at wavelengths 0.5-1.6 micron acquired by SELENE Spectral Profiler and their dependency on local albedo and latitudinal zones, *Icarus*, *215*(2), 639–660, doi:10.1016/j.icarus.2011.07.028.

Zebker, H., B. Stiles, S. Hensley, R. Lorenz, R. L. Kirk, and J. Lunine (2009), Size and shape of Saturn's moon Titan., *Science*, *324*(5929), 921–3, doi:10.1126/science.1168905.

Zebker, H. A., L. Iess, S. D. Wall, R. D. Lorenz, J. I. Lunine, and B. W. Stiles (2012), Titan's Figure Fatter, Flatter Than Its Gravity Field, in *AGU Fall Meet. 2012*, pp. P23F–01.

Zuber, M. T., J. W. Head, D. E. Smith, G. A. Neumann, E. Mazarico, M. H. Torrence, O. Aharonson, A. R. Tye, C. I. Fassett, M. A. Rosenburg, and H. J. Melosh (2012), Constraints on the volatile distribution within Shackleton crater at the lunar south pole., *Nature*, *486*(7403), 378–81, doi:10.1038/nature11216.